August 2015

Magnetic transport properties of oriented soft, hard and exchange-coupled magnetic thin films and $Au_{25}(SC_6H_{13})_{18}$ spherical nanocluster

Rukshan M. Thantirige
University of Massachusetts - Amherst

Recommended Citation

Thantirige, Rukshan M., "Magnetic transport properties of oriented soft, hard and exchange-coupled magnetic thin films and $Au_{25}(SC_6H_{13})_{18}$ spherical nanocluster" (2015). *Doctoral Dissertations*. 410.
https://scholarworks.umass.edu/dissertations_2/410

MAGNETIC TRANSPORT PROPERTIES OF ORIENTED SOFT, HARD AND EXCHANGE-COUPLED MAGNETIC THIN FILMS AND $Au_{25}(SC_6H_{13})_{18}$ SPHERICAL NANOCLUSTER

A Dissertation Presented

by

RUKSHAN M. THANTIRIGE

Submitted to the Graduate School of the

University of Massachusetts Amherst in partial fulfillment

of the requirements for the degree of

DOCTOR OF PHILOSOPHY

May 2015

Department of Physics

MAGNETIC TRANSPORT PROPERTIES OF ORIENTED SOFT, HARD AND EXCHANGE-COUPLED MAGNETIC THIN FILMS AND $Au_{25}(SC_6H_{13})_{18}$ SPHERICAL NANOCLUSTER

A Dissertation Presented

by

RUKSHAN M. THANTIRIGE

Approved as to Style and Content by:

Mark Tuominen, Chair

Adrian Parsegian, Member

Narayanan Menon, Member

Dhandapani Venkataraman, Member

Rory Miskimen, Department Chair
Department of Physics

ACKNOWLEDGMENT

In performing my research, I received support, help and guidance from many respected individuals, who deserve my greatest gratitude. First of all, I am indebted to my research adviser, Prof. Mark T. Tuominen for countless advises, encouragements and patiently guiding me and investing in my research education for the last five years. Also, I would like to thank Prof. Adrian Parsegian, Prof. Narayanan Menon and Prof. Dhandapani Venkataraman for serving on my thesis committee and giving insightful advises. Further, I pay my gratitude to Prof. Katherine Aidala at Mt Holyoke Collage for her helpful guidance in conducting my research.

I'm specially grateful to former group members Dr. Nihar Pradhan, Dr. Nikhil Malvankar, Dr. Stefan Dickert, Dr. Tianyu Yang, Dr. Huajie Ke as I received most of my training from them. I would also thank Dr. Craig Versek for his help and guidance in micromagnetic work and Mr. Michel Thorn for his useful advises. I further acknowledge Ms. Dan Wang, Mr. Ramesh Adhikari and Mr. Asanka Weerasinghe for helping me with some of my sample preparation and measurements, and all current group members for helping me to maintain and repair lab equipment.

In addition, I'm very grateful to my collaborators from other departments and other universities: Dr. Jacob John and Prof Ken Carter at the department of Polymer Science and Engineering for providing me nanoimprinted gratings and teaching me nanoimprint

lithography, Dr. Saikat Gosh from Food Science department for helping me in analyzing nanoparticle properties, Mr. Viraj Thanthirige, Prof. Guda Ramakrishna and Prof. Ekkehard Sinn at department of Chemistry, Western Michigan University for supplying me $Au_{25}(SC_6H_{13})_{18}$ nanoclusters and sharing valuable information about recent developments in diamagnetic nanoclusters and their optical absorption properties, Dr. Deepak Singh from NIST for fruitful discussions and inspiring me with novel fabrication ideas.

I would also like to pay my special gratitude to Mr. John Nicholson for all his help with cleanroom instruments and sharing information about new sample fabrication techniques and capabilities. Further, I acknowledge Mr. Jacob Hirsch and Mr. Pete Dawson for their help in XPS and XRD measurements. Also, I'm grateful to Mrs. Jane Knapp, Mrs. Barbara Keyworth, Prof. Krishna Kumar and Prof. Carlo Dallapiccola for their help in many ways, and other faculty members for teaching me course work and inspiring me to continue learning.

Finally, I would like to thank my undergraduate adviser, Prof. B.S.B. Karunaratne and other faculty members at the University of Peradeniya, Sri Lanka for preparing me for the graduate education and all my family and friends for all their guidance, patience, understanding and supporting me.

ABSTRACT

MAGNETIC TRANSPORT PROPERTIES OF ORIENTED SOFT, HARD AND EXCHANGE-COUPLED MAGNETIC THIN FILMS AND $Au_{25}(SC_6H_{13})_{18}$ SPHERICAL NANOCLUSTER

MAY 2015

RUKSHAN M. THANTIRIGE

BS - UNIVERSITY OF PERADENIYA, SRI LANKA

MS - UNIVERSITY OF MASSACHUSETTS, AMHERST

PhD - UNIVERSITY OF MASSACHUSETTS, AMHERST

Directed by: Professor Mark T. Tuominen

This study was conducted with the aim of improving permanent magnetic properties of existing materials and exploring non-conventional ferromagnetic properties of gold-based nanoclusters. The first chapter of this dissertation gives an introduction to relevant fundamental concepts and proceeding chapters present findings of three projects.

In the first project, shape anisotropy induced permanent magnetism in oriented magnetic thin films was investigated. Roll-to-roll nanoimprinting, a high-throughput fabrication method was utilized to fabricate densely packed Fe nanostripe-based magnetic thin films that exhibit large in-plane uniaxial anisotropy and nearly square hysteresis loops at room temperature. $(BH)_{max}$ exceeds 3 MGOe for samples of intermediate thickness and the anisotropy dependence on film thickness was also investigated. Temperature dependent magnetic measurements and micromagnetic simulations confirmed that the magnetization reversal is dominated by curling reversal mode.

The second project is an investigation of how magnetization reversal of hard and exchange-spring magnets is affected by substrate properties. Thin layers of $SmCo_5$ and $SmCo_5/Co$ with varying thickness were grown at 500^{o} C by sputtering on MgO(100) and glass with a Cr underlayer. X-ray diffraction studies reveal that in-plane hard magnetic properties is a result of $SmCo_5$ $(11\ \bar{2}\ 0)$, guided by the Cr (200) of the seed layer. The $(BH)_{max}$ of samples made on MgO(100) are higher due to high degree of $SmCo_5$ $(11\bar{2}0)$ formation with in-plane orientation by epitaxial guidance. Temperature dependent studies performed on exchange-coupled samples show that H_C linearly increases with decreasing temperature, however, an exchange decoupling can be observed at lower temperatures only for the sample grown on glass.

In the third project, field-cooled and temperature dependent magnetic properties of $Au_{25}(SC_6H_{13})_{18}$ spherical nanocluster are reported. This ensemble shows a weak exchange-biased behavior below 125 K. With increasing the cooling-field at constant temperature, the H_C drops while M_S rises which suggests that the magnetic state transforms from an exchange-bias like to a ferromagnetic dominated state. Temperature

dependent measurements show unusual behavior in H_C with the temperature, which drops first and then rises above 125 K, while magnetization rises non-monotonically. We believe this non-trivial phenomenon can be caused by magnetic phase transitions or thermally induced long-range interactions.

TABLE OF CONTENTS

Page

CHAPTER

LIST OF TABLES

Table Page

LIST OF FIGURES

Figure Page

CHAPTER 1

FUNDAMENTALS AND RELEVANT CONCEPTS

A brief introduction to magnetism and closely related concepts are discussed in this chapter to help establish a theoretical foundation for the rest of the dissertation. The chapter begins with the origin of ferromagnetism and ends with the exchange-bias effect.

1.1 Origin of Ferromagnetism

The origin of magnetism can be related to the electron motion and the electronic configuration of an atom. In general, if the outermost electron shell of an atom is not filled, such materials show paramagnetic properties, as uncoupled electrons respond to external magnetic fields, which results a positive magnetic response. The majority of metals fall into this category. On the other hand, relative motion of the electron induces diamagnetic properties as it counters the external magnetic field and results a negative response to an external magnetic field. In principle, all materials have a diamagnetic response but its effect is predominant in materials with closed outer electronic shells, although this rule does not apply in all occasions. As an example Au, Ag have $d^{10}s^{1}$ configuration but they show diamagnetic properties due to the dominance of closed *d* shells.

Ferromagnetic materials exhibit a spontaneous magnetic moment below a critical temperature called Curie temperature T_C, below which all magnetic moments align in a particular direction due to a strong short-range interaction between magnetic spins called 'exchange interaction' that results a long range magnetic ordering. Typical magnetic dipole-dipole interactions cannot account for this phenomena as such interactions are very weak (< 1 K) and vanish due to thermal fluctuations. Moreover, dipole-dipole interactions prefer anti-parallel alignment when two magnetic dipoles are brought into close proximity. The exchange interaction is a quantum mechanical phenomena based on minimizing coulomb repulsion between adjacent atoms when their valence electrons overlap in certain materials. That is, if the coulomb repulsion can be minimized (electrons are further apart) when electrons have parallel spins than they have opposite spins, parallel alignment yields lower total energy and leads to ferromagnetic ordering with a high magnetic moment ground state. The opposite is true if the coulomb repulsion is minimized by opposite spin configuration, which leads to zero magnetic moment ground state, called antiferromagnetic state [1, 2].

The exchange interaction can be further explained by Heisenberg model, with the following Hamiltonian that describes the interaction between the individual spins in a three-dimensional lattice.

$$\hat{H} = -2\sum_{i>j} J_{ij} S_i \cdot S_j \tag{1.1}$$

With the exchange integral,

$$J_{ij} = \iint \psi_i^*(\vec{r_1}) \cdot \psi_j^*(\vec{r_2}) \cdot \hat{H} \cdot \psi_i(\vec{r_2}) \cdot \psi_j(\vec{r_1}) \cdot d\vec{r_1}\, d\vec{r_2} \qquad (1.2)$$

If J_{ij} is positive, the ensembles prefers a parallel ordering leading to a ferromagnetic state and anti-parallel ordering is favorable when J_{ij} is negative, resulting a antiferromagnetic state with zero-spin moment. This direct exchange interaction is possible when unpaired orbitals of adjacent atoms overlap, however even when such overlapping does not take place interaction can be mediated by a third party involvement (indirect exchange) that usually results long-range coupling. Such interactions that are arbitrated by non-magnetic ions located between magnetic ions are called ‘super-exchange’ interactions, and they usually result antiferromagnetic ordering (ex: MnO, MnF_2). In addition, indirect exchange can also be mediated by conduction electrons. Here, localized magnetic moments, which are r distance away can spin-polarize surrounding conduction electrons which in turn couples the localized moments. These types of interactions are called RKKY (Ruderman, Kittel, Kasuya, Yosida) interactions and they take the following form.

$$J_{RKKY}(r) \propto \frac{\cos(2K_F r)}{r^3} \qquad (1.3)$$

This is essentially an r dependent long-range interaction with an oscillatory term so depending on the separation, RKKY can result both ferromagnetic and antiferromagnetic ordering. RKKY interaction is a contributing component of giant magnetoresistance (GMR) multilayer materials, which play an important role in technological applications [1, 3].

The exchange interaction in iron series transition metals (Fe, Co, Ni) and their alloys are mediated by the delocalized conduction 3*d* electrons (while 4*s* can indeed provide RKKY type interactions), evident by their non-integer magnetic moments such as 2.2 μ_B, 1.7 μ_B and 0.6 μ_B for Fe, Co and Ni, respectively. This is called band ferromagnetism or itinerant ferromagnetism. The origin of ferromagnetic ordering in 3*d* transition metals can be explained by the Stoner model that combines the onsite magnetic ordering by band splitting (spin-split bands) with density of states (DOS) at the fermi level $D(E_F)$ [1]. This condition is only satisfied if the spin splitting is energetically favorable. Let us consider the spin-split and non-split (degenerate state) conditions (Figure 1.1). In the non-split state both spin-up and spin-down sub-bands are degenerate, resulting a state with zero magnetic moment, however the presence of strong crystal fields can change this population by raising the spin-up sub-band while lowering the spin-down sub-band by same magnitude that creates an energy gap as shown. This leads to a stable state with non-zero magnetic moment, if increased kinetic energy due to population change in sub-bands is compensated by the energy reduction due to exchange interaction. This is represented by the well known Stoner criterion,

$$I \cdot D(E_F) \geq 1 \tag{1.4}$$

Where I is spin-spin coupling constant, a measure of coulomb interaction. Materials those meet the above condition are considered ferromagnetic. Figure 1.2 is the variation of $I.D(E_F)$ with atomic number which shows Fe, Co and Ni fulfill the Stoner criteria.

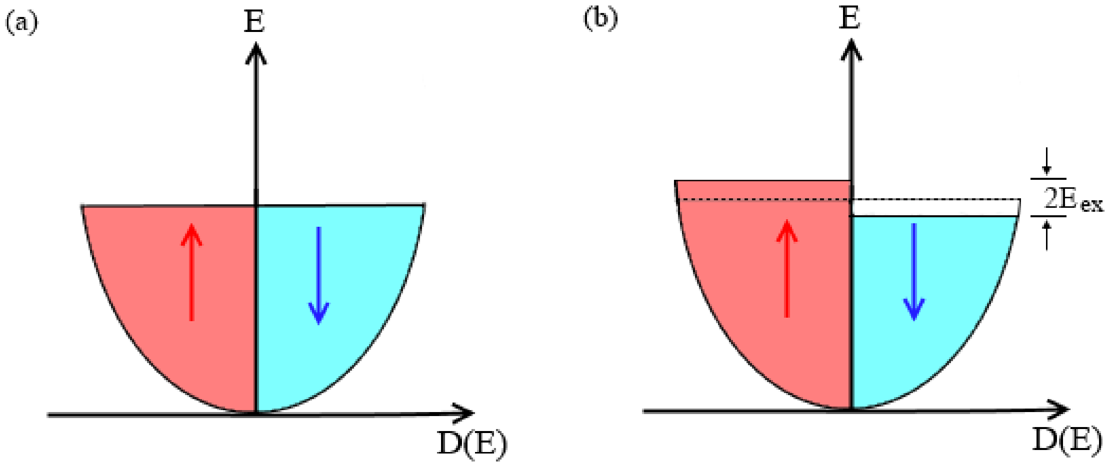

Figure 1.1 - Schematic of the spin density of (a) spin-split and (b) non-split 3*d* bands of transition metal. Spin-up and spin-down 3*d* electrons have an energy difference of $2E_{ex}$, the exchange splitting.

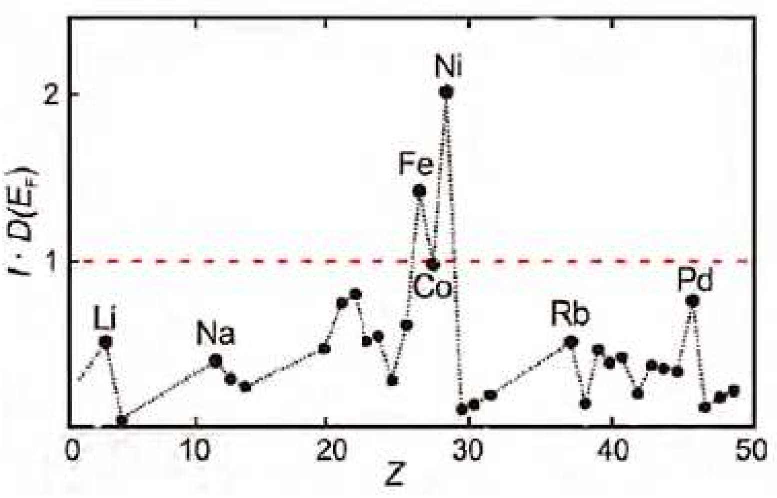

Figure 1.2- Variation of $I.D(E_F)$ with the atomic number. Only Fe, Co and Ni fulfill the Stoner criterion to show ferromagnetism (adopted from ref [3]).

Here, the exchange integral I depends only on the element, however the $D(E_F)$ depends on the crystal structure, microscopic organization, geometry and outside environment. As an example noble metals such as Ag, Pt and Au in bulk show diamagnetism but show strong ferromagnetic properties in ligand stabilized ultrafine nanoparticles due to size reduction and surface induced effects [4-8]. Heusler alloys is another such example where compounds exhibit ferromagnetic properties although they do not contain ferromagnetic elements [9, 10].

Also, it is important to realize that ferromagnetism does not just depend on the elemental composition but strongly on crystal structure as well [11]. As an example *bcc* Fe and Ni have higher DOS than their *fcc* versions, so the $I.D(E_F)$ product of *bcc* Fe and Ni are higher, or in other words ferromagnetic (Figure 1.3). Contrarily, certain alloys with ferromagnetic elements such as certain grades of stainless steel show no ferromagnetism.

In rare earth magnetic materials (alloys of rare-earth and transition metals), the magnetism reflects indirect exchange, RKKY type, interactions as 4f electrons in rare earth elements such as Sm and Nd, are essentially localized while 3d electrons of transition metals in the same lattice are itinerant. These materials have large anisotropies due to their asymmetric crystalline structures but their magnetic moments are relatively lower as a result of non-magnetic rare earth elements [12, 13]. More details about rare-earth magnetic materials and their dynamics will be discussed in Chapter 3.

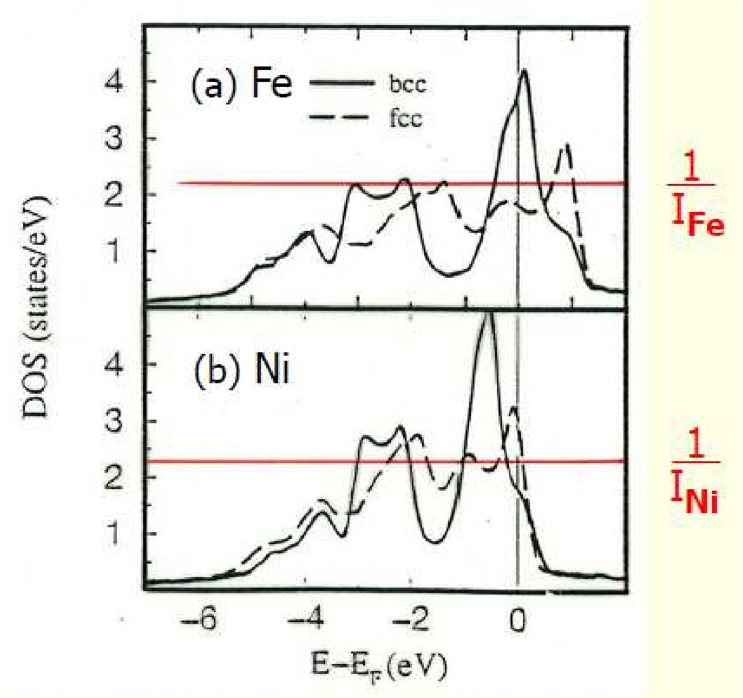

Figure 1.3 - DOS dependence on crystal structure for Fe and Ni. For both Fe and Ni, bcc structure has higher DOS that promotes strong ferromagnetic properties (adopted from ref [11]).

1.2 Magnetic Anisotropy

Magnetic anisotropy is the ability to direct the magnetic moments in particular or predefined directions by breaking the symmetry. It can be intrinsic as certain magnetic crystals have preferred directions with minimum energy configurations as a result of crystal asymmetry. This is called magnetocrystalline anisotropy and is observed in many magnetic materials with hexagonal or tetragonal crystal structures, and it is mostly a material dependent property. Magnetic anisotropy can also be induced and tailored by changing the shape. This is because magnetic charges of the body prefer to concentrate in corners or on sharp edges, which creates magnetic dipoles within the body. In thin films, additional anisotropy terms come into play due to film thickness, surface roughness, exchange coupling (if multilayered), epitaxy and strain conditions. In general, magnetic anisotropy plays an important role as it results a highly ordered configurations, which make materials usable in variety of applications [1, 14].

The origin of magnetocrystalline anisotropy is the spin-orbit interaction. In order to explain this let us consider a one-dimensional chain of atoms (Figure 1.4). As a result of spin-orbit interaction the atomic orbitals are spheroidal which are otherwise nearly spherical. Hence, when electron orbitals align with the crystal field, it results in two distinct arrangements with different energy configurations. As shown in Figure 1.4, the configuration (a) has lower energy due to low electrostatic repulsion in comparison to configuration (b) where atomic orbitals in adjacent atoms lie closer. So magnetic moments orient (or can be oriented with minimum energy) as in configuration (a) and its direction is called the 'easy-axis'.

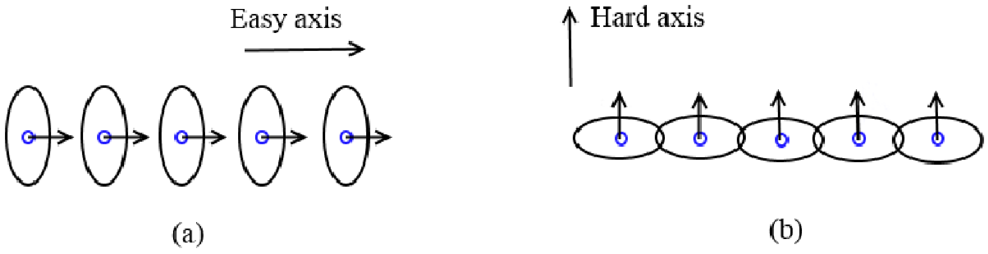

Figure 1.4 - Spin arrangement of a 1-D atomic chain. a) low energy configuration b) higher energy configuration.

However, this effect vanishes if the crystalline structure is isotropic such as *bcc* or *fcc*, as such crystals have no crystal asymmetry. Let us consider a two dimensional crystal with lattice constants *a* and *b* (Figure 1.5). If *a* and *b* are same then both configurations are equally probable, leaves no preferred direction for magnetic moments to align [2]. But, if the crystal structure is asymmetric as in the case of hexagonal and tetragonal crystals ($c/a > 1$) it results well defined easy-axis with large anisotropies. As an example Fe, Ni are *bcc* and they have negligibly small magnetocrystalline anisotropies while Co and $SmCo_5$ have large magnetocrystalline anisotropies as a result of their hexagonal crystal structure (Figure 1.6). Also, if the crystal has one preferred direction, the anisotropy is called uniaxial and takes the following form.

$$K_{uni} = K_1 \cdot Sin^2\theta + K_2 \cdot Sin^4\theta + ... \tag{1.5}$$

Where θ is the angle between the magnetization direction and the easy axis, and K_1 and K_2 are the anisotropy constants.

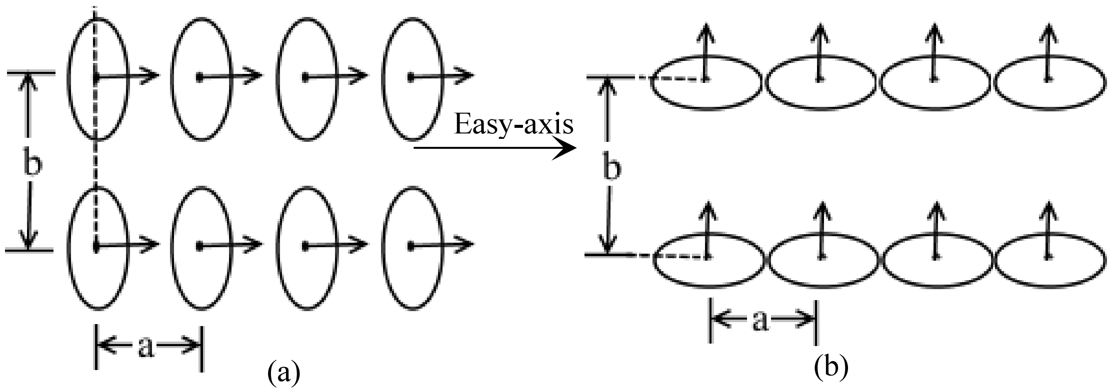

(a) (b)

Figure 1.5 - Spin arrangement in an asymmetric magnetic crystal. a) Spins oriented along easy axis b) Spins oriented along hard axis.

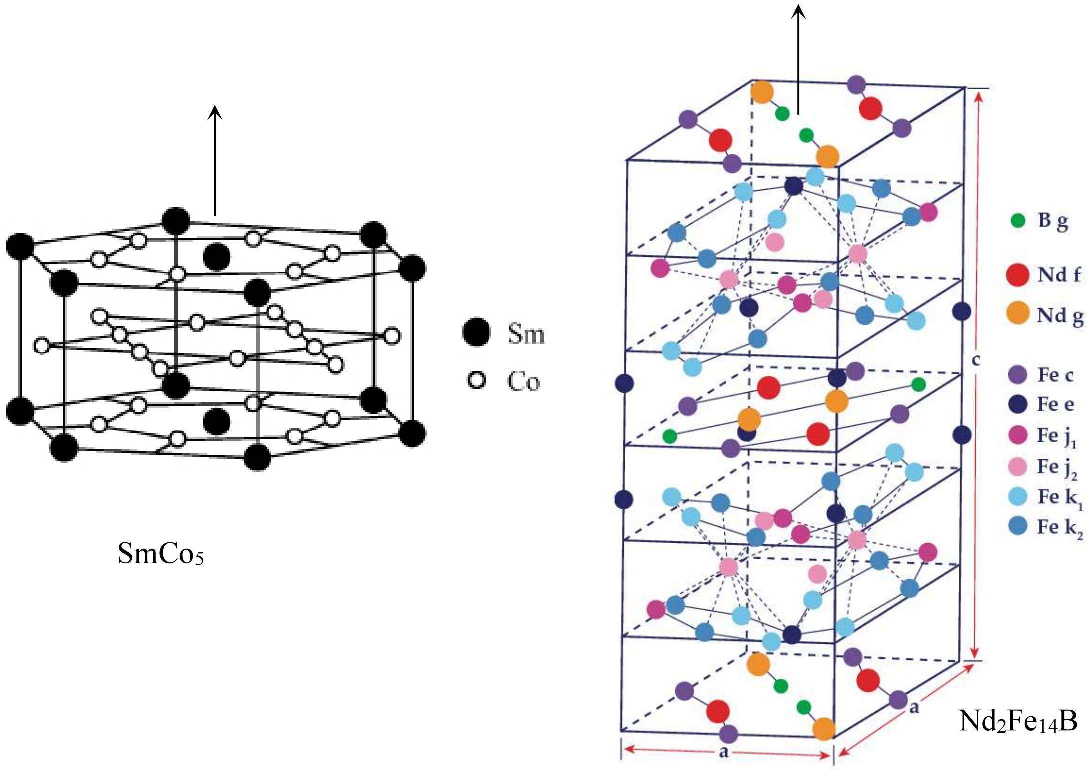

$SmCo_5$

$Nd_2Fe_{14}B$

Figure 1.6 - Crystalline structures of $SmCo_5$ and $Nd_2Fe_{14}B$. These magnetic materials have strong uniaxial anisotropy along z-axis (arrow) due to crystal asymmetry (adopted from ref [15, 16].

The anisotropy arises from the geometry or the shape of the object is the shape anisotropy, is one of the fundamental sources of magnetic anisotropy which can be tailored as desired. If we consider an elliptical body, it produces magnetic poles on extreme ends of the object, surface across the long axis. This induced dipole by the shape, produces a demagnetizing field (stray field) within the magnetic body, which creates a preferential ordering of magnetic moments along the long axis, resulting an anisotropy. The stray field and its energy association for a uniformly magnetized body can be given by [1, 2],

$$\langle H_d \rangle = N \langle M \rangle \tag{1.6}$$

$$E_d = -\frac{1}{2}\mu_o \int M.H_d.d^3r \quad (1.7)$$

Where H_d and N are stray field and demagnetization factor (3x3 tensor depends on the sample geometry), respectively.

The effect of shape anisotropy can be illustrated by considering a prolate ellipsoid (Figure 1.7).

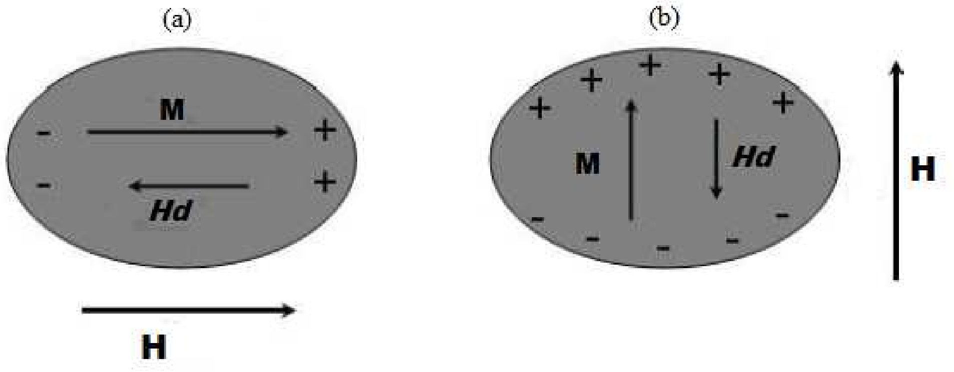

Figure 1.7 – Magnetostatic energy of a prolate ellipsoid a) lower magnetostatic b) high magnetostatic energy configurations (adopted from ref [17]).

If demagnetization factors of configuration (a) and (b) are N_a and N_b respectively, the shape anisotropy K_{shape} is given from the magnetostatic energy density difference between configuration (b) and (a) (magnetization perpendicular to the easy axis (E⊥) and parallel to the easy axis (E∥).

$$K_{shape} = \frac{1}{2}\mu_0 (N_b - N_a) M_s^2 \quad (1.8)$$

For an example, if we consider an ellipsoid with c/a (long axis/short axis) = 10, $N_b - N_a \sim 0.477$. For Fe ($M_S = 1700$ KAm^{-1}), this gives an anisotropy of $8.7\text{x}10^5$ Jm^{-3} that is larger than it's intrinsic anisotropy, $5\text{x}10^4$ Jm^{-3}.

Ferromagnetic thin films have different properties than that of their bulk counterparts as the surface atoms have a different environment than the bulk ones. This symmetry breaking at the interface (surface) and reduced coordination number results surface magnetocrystalline anisotropy, which is different from bulk magnetocrystalline anisotropy. This can be accounted to the decrease of magnetic moments of free Fe and Ni surfaces upon coating with non-magnetic metals or upon exposed to gases [18, 19].

Further, when thin films are not atomically smooth, an anisotropy can be created from surface roughness as it creates magnetic charges at the surface [20]. Dubowik derived an expression for surface anisotropy due to surface roughness by considering the magnetostatic energy of a surface in the form of 2-D array of cylinders with diameter a, separation b and height t (Figure 1.8) [21].

$$K_s = 2\pi M^2 3\sigma\varepsilon f(1-f) \tag{1.9}$$

Where ε and f are ellipticity factor and packing fraction (determined by a/b ratio), respectively.

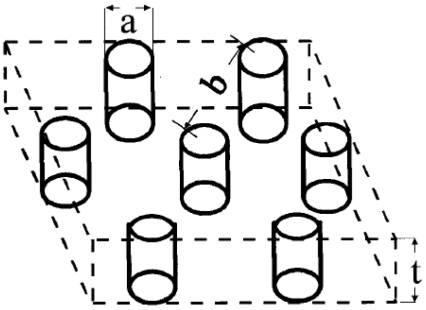

Figure 1.8 - Two-dimensional finite array of cylindrical particles of diameter *a*, height *t*, and separation *b* (adopted from ref [21]).

In addition, surface (interface) roughness generate domain wall pinning centers that induces extra coercivity. This will be discussed in details later in this chapter.

Moreover, magnetic properties of many thin films strongly depend on the substrate as properties change due to crystal match/mismatch and strain. Crystal match/mismatch or epitaxy as commonly quoted, plays an important role in almost all thin film based manufacturing processes from semiconductor to magnetic applications and it refers to registry of crystal between overlayer and substrate or underlayer. In magnetism, epitaxy is commonly used in aligning moments in-plane or perpendicular to the substrate and to control the grain size especially in hard magnetic or exchange-coupled magnetic thin films. One such example is $SmCo_5$ deposited on Cr underlayer shows high in-plane anisotropy [22, 23], while $SmCo_5$ deposited on Ru or Ti/Cu underlayer show high perpendicular anisotropy [24, 25]. Contribution of strain has been observed in variety thin film samples [26-28].

Even though it is practically difficult to isolate the anisotropy arising from surface roughness from surface magnetocrystalline anisotropy and strain anisotropy, domination of each factor has been studied in details [29-32]. So in general, the cooperative contribution of surface effects to the total anisotropy is considered. Hence, the effective anisotropy of a thin film with thickness t is given by [1],

$$K_{eff} = K_v + \frac{2K_s}{t} \tag{1.10}$$

Where Kv and Ks are total volume anisotropy and total surface anisotropy, respectively. At large thicknesses, the volume term dominates and the magnetization lies in-plane, driven mainly by shape anisotropy. With reducing thickness, surface anisotropy term starts dominating that eventually favors magnetization aligning perpendicular to the plane, below a critical thickness (Figure 1.9). In other words, the perpendicular anisotropy is attributed to surface anisotropy which has great technological interests such as magnetic data storage and magneto-optic devices.

1.3 Magnetic Domains

Magnetic domain is small region where all magnetic moments are aligned in one direction or in other words, magnetic moment is saturated within the domain. Each grain of the magnetic body consists number domains and each has local magnetization oriented in different directions. In general, domains are created to minimize the stray field as if all magnetic moments align in one direction throughout the body, it creates a large stray field. This is not energetically favorable as it costs $\mu_o H^2/2$ energy per unit volume, unless it is supported by anisotropy (Figure 1.10).

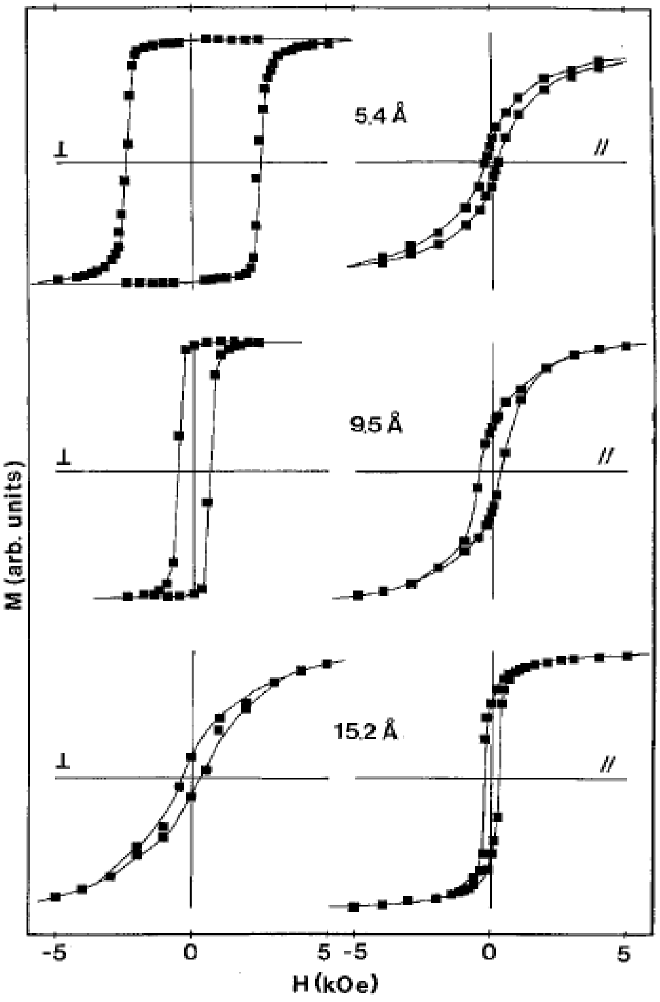

Figure 1.9 - Hysteresis loop with H perpendicular and parallel to the film plane for Au/Co/Au sandwiches with t_{Co}= 5.4 A, 9.5 A and 15.2 A, at T=10 K (adopted from ref [20])

Domains are separated by a singularity called domain wall, a transition between two domains that undergoes an angular displacement up to 180°. Creation of domains costs energy as it needs to do work against exchange interaction therefore, the domain size is determined by the balance of exchange, magnetostatic and anisotropic energy terms. Larger exchange energies and smaller anisotropies results smaller domains while smaller exchange energies and larger anisotropies results larger domains ($SmCo_5$ ~ 1.3 μm). In thin films, there can be two types of domain walls (Figure 1.11), depending on the thickness; Bloch walls and Neel walls. The common type is Bloch wall but Neel walls are energetically favorable in ultra-thin films [6].

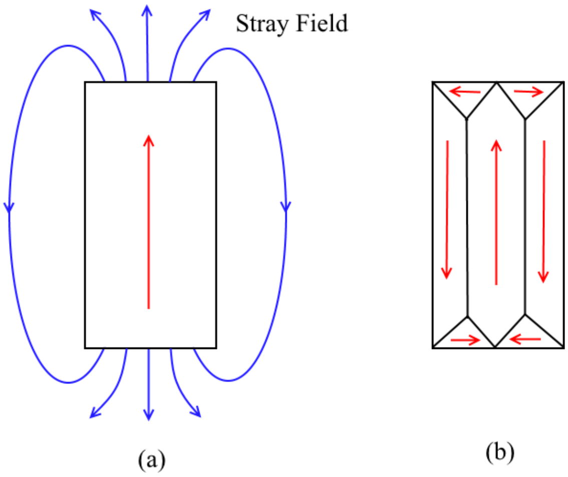

Figure 1.10 - Magnetic body in a) single domain state with maximum stray field b) multi-domain (closure domain) state with no stray field.

The domain wall thickness (δ) and its energy per unit area (σ) are given by [1],

$$\delta = \pi\sqrt{\frac{A}{K}} \tag{1.11}$$

$$\sigma = \pi\sqrt{AK} \tag{1.12}$$

Where A and K are exchange stiffness and anisotropy constant, respectively.

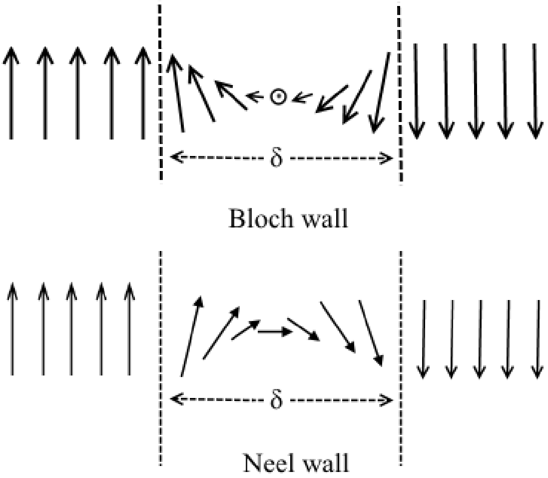

Figure 1.11- Magnetization rotation of 180^0 a) Bloch wall - rotates perpendicular to the plane of the wall b) Neel wall - rotates in-plane to the plane of the wall.

These two equations suggest that materials with low anisotropies have broad domain walls and low domain walls energies, which favors domain formation, while highly anisotropic materials with narrow domain walls and large domain wall energies resist domain formation, hence such materials have large domains.

Formation of domains leads to a significant reduction of actual magnetic moment (which is the vector sum of individual domain moments), in comparison to the saturated state, where all domains are aligned by an external field. However, when the size of the magnet body is reduced, the domain formation is more costly and below a critical dimension, it exceeds the dipolar energy of the magnetic body. This leads to the removal of all domain walls and the magnet becomes single domain. A single domain body has essentially only two magnetic states (spin-up and spin-down) and its dynamics is described by Stoner-Wohlfarth model, which assumes a single domain to a macroscopic spin. Figure

1.12 shows the magnetization dynamics of a Stoner particle when an external field *H* is applied.

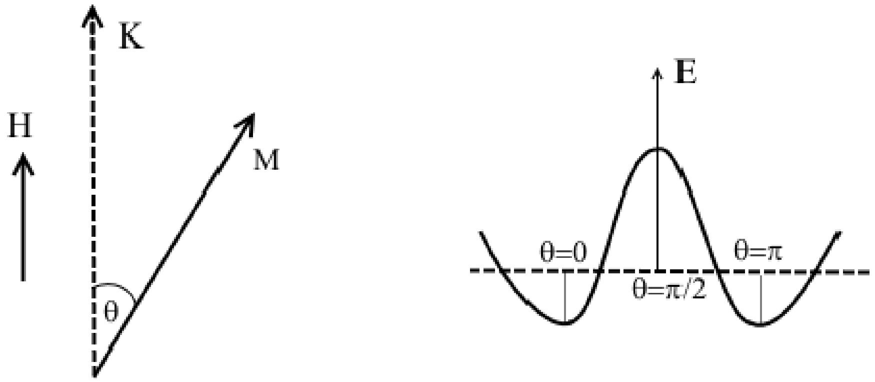

Figure 1.12 - Stoner-Wohlfarth model for single domain particle. Minimum energy configuration realized when the particle axis aligned to external field.

Where, *K* and *M* are anisotropy and magnetization. Here, the energy of the magnetic moment is given by,

$$. E = K\sin^2\theta - \mu_0 HM\cos\theta \qquad (1.13)$$

If the magnet size is further reduced then magnetization fluctuates as thermal energy come into play, as the anisotropy energy (energy barrier) decreases with the volume ($E_{an} = KV$). If the magnet is made sufficiently small as such the thermal energy overcomes the energy barrier, the magnetic spin starts to flip its direction randomly (between θ=0 and θ=π). If the time between two flips, which is called Neel relaxation time, is smaller than the measurement time of the instrument, the net magnetization appears to be zero. This effect is called superparamagnetism.

1.4 Magnetization Reversal

In general, magnetization reversal is changing the state of a magnet most commonly by applying an external magnetic field. However, electric field or electric current induced magnetization reversal for certain materials has been reported [33, 34]. The reversal process is typically represented by a magnetic hysteresis loop which shows the change in magnetic state with respect to the applied field. Figure 1.13 shows the hysteresis of a common magnetic material such as iron in bulk, which is usually in a demagnetized state due to random orientation of domains in the absence of an external field. So when a field which is large enough is applied, the magnet becomes saturated with all magnetic moments align with the external magnetic field achieving the highest moment M_S. This is called the saturated state. When the field is removed the magnetic moment drops and domains become relatively disoriented in comparison to the saturated state, but a net magnetic moment Mr retains in the system (along the magnetized direction), and the magnet is said to be in the remanent state. In order to demagnetize the magnetic body, an opposite field is applied and the required field is called the coercivity or coercive field H_C. At this state, magnetic domains are randomly oriented resulting a zero net magnetization. By increasing external magnetic field further the magnet can be saturated to the negative saturation $-M_S$, so all magnetic moments are aligned once again but in the opposite direction. By applying a positive magnetic field, the magnetization can be reversed to M_S, hence the process is cyclic.

The actual reversal mechanism depends on the material, size, geometry as well as metallurgical conditions. If the magnet is multi-domain then the dominant reversal mechanism is domain wall motion. When an external field is applied, domains oriented in the same direction grow with the expense of domains oriented in other directions.

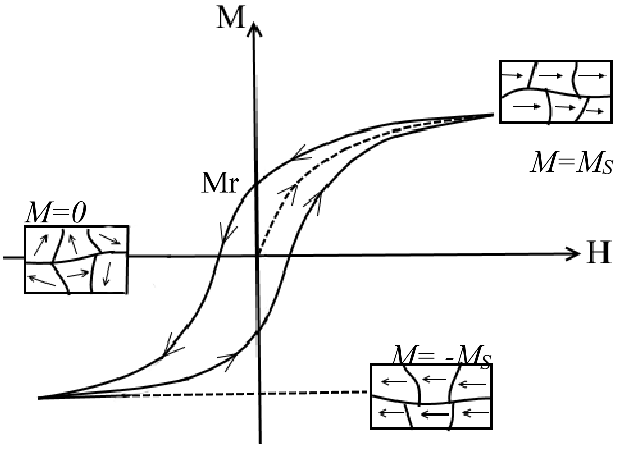

Figure 1.13 - Non-linear M-H curve (hysteresis curve) of a typical ferromagnetic material.

This process conserves energy as it avoids the necessity of rotating each domain with the magnetic field, which requires higher energies. However, with increasing external field domain rotation occurs, so that domains try to align with the easy axis closest to the external field. At high magnetic fields, all magnetic moments can rotate coherently regardless their original direction. This process is called coherent rotation and it requires larger energies which is not favorable for multi domain samples. Thus in general, when magnetizing a multi-domain sample, it first undergoes domain wall motion followed by domain rotation [1, 13].

However, if the magnet is single domain then the reversal can take two pathways; coherent rotation and incoherent reversal. The incoherent reversal can take many modes derived from two main modes called curling and bucking. The crossover between these two pathways depends on the size and the shape of the magnetic body [35]. For a small spherical particle (nanoparticle), all magnetic moments rotate coherently with no relative motion between magnetic spins if the particle size is smaller than the critical diameter given by $D_{cric} = \sqrt{26A / \mu_0 M_S^2}$. However, in curling reversal mode, the dominating reversal mechanism of finite size magnetic nanostructures such as magnetic nanorods and nanostripes, a small volume of the sample called activation volume undergoes nucleation. This region is called the nucleation core and it propagates throughout the sample until all magnetic spins are reversed (discussed in details in Chapter 2).

Domain wall pinning is another important factor that affects the magnetization reversal process. In the presence of structural defects and rough interfaces [36-38] which serve as pinning centers, magnetic moments ‘trapped’ in local energy minima. This hinders domain wall motion, so extra energy is required to release (de-pin) these trapped spins to continue with the reversal process. In addition to random inhomogeneities, narrow domain walls specially in hard magnetic layered structures also cause pinning effects that has been considered a dominant contribution to their higher coercivities [39, 40]. Also, pinning effect is induced in magnetic heterostructures such as spring-exchange or exchange-bias systems (will be discussed later in the chapter) which has great technological implications.

1.5 Permanent Magnets

A permanent magnet can be defined as those materials capable of creating its own persistent magnetic field. These materials include pure transition metals such as iron, cobalt, nickel and some alloys of rare earth metals and minerals such as lodestones and ferrite. Permanent magnets have been used for navigation as early as the 5th century BC, but today they are used in every major industry from electronics to power generation, from a simple refrigerator magnet to advanced medical equipments. Since the beginning of the 20th century the permanent magnetic materials have transformed from magnetic steels to intermetallic composites and oxides.

The most important parameter in describing a permanent magnetic is its maximum energy product $(BH)_{max}$. That is a measure of the power of the magnet or the maximum magnetic energy stored in the magnet. On the other hand, (BH) product can be considered as the combination of magnetic field generated by the magnet (Br) and its stability (H_C) in a particular direction (Figure 1.14). This is an essential quality of permanent magnets as they generate high fields simultaneously maintaining its stability, as represented by the maximum of the combined effect, $(BH)_{max}$. Magnetic materials are divided into two categories based on their response to an external field. The "soft" magnetic materials have high Mr, high permeability and low H_C. Transition metals and their alloys fall into this category. Most of rare earth metal based magnets are considered "hard" magnetic materials with their high H_C and relatively low Mr. Their $(BH)_{max}$ is significantly larger than that of soft magnets which is an essential property of permanent magnets [13, 14].

Alnico family is the first realistic permanent magnetic material class with H_C starting from 300 Oe and they made the strongest permanent magnets before the development of rare earth magnets in 1970's. The quest for creating a large energy product has been achieved by alloying transition metals with light rare earth metals and small atoms such as oxygen, carbon, boron and nitrogen. Here, the transition metal provides the necessary remanence while the exchange interactions between 3d-4f electrons at sites having uniaxial symmetry produce a large uniaxial anisotropy to get higher H_C [41]. The addition of small atoms such as carbon or nitrogen to interstitial sites increases the crystal field by further orbital deformation. The first of such materials is Sm-Co family that has high magnetic energy densities of up to 30 MGOe. In 1983, a new generation of rare-earth magnets based on Nd, Fe and B was discovered by Sumitomo Special Metals and General Motors [42,43]. They are not only more efficient and have higher energy densities but also less expensive as Co and Sm are replaced by much cheaper and abundant Fe and Nd. Later, $L1_0$ phase (*fct* phase) rare earth materials such as FePt and CoPt have been introduced and their perpendicular anisotropy in thin films has revolutionized the idea of high density magnetic recording media [44-48]. Recent reports of successful fabrication of $L1_0$ FeNi [49-51] and $Fe_{16}N_2$ [52,53] have caught great attention in the industry as the cost of such materials is a fraction of rare earth magnets. However, these rare earth free magnets are still at the research level in regards to their behavior and stability.

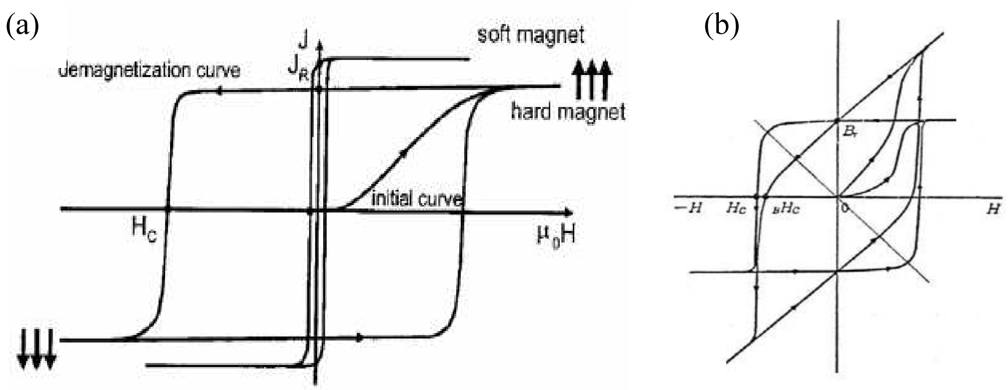

Figure 1.14 – a) M(H) vs H for soft and hard magnetic materials b) M(H) vs. H and B(H) vs. H of a permanent magnet (figure adopted from ref [17]).

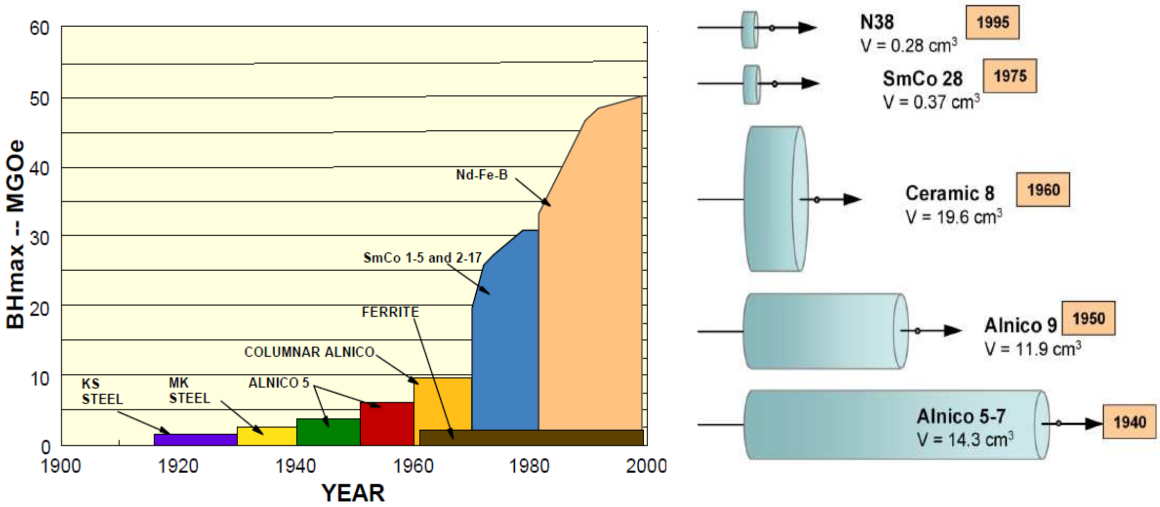

Figure 1.15 - a) Progress in development of permanent magnets and b) size required to generate 1000 Oe field (adopted from ref [54])

1.6 Spring-Exchange magnets

Despite being used as permanent magnets, rare earth intermetallics suffer from low remanence, as a result of a significant portion of its volume being occupied by non-magnetic materials. Also, their low Curie temperatures (<600 ^{0}C) limit their usage in high temperature applications. The quest for magnets with megajoule (>100 MGOe) energy densities is still a long way with intermetallic modification, however nanotechnology has enabled a possible means to engineer composite materials that can reach megajoule energy products with existing materials. These magnets are called spring-exchange or exchange-coupled magnets, which are engineered composites magnet of hard and soft magnetic materials. However, this should be done in nanoscale in such a way that the soft phase is rigidly coupled or pinned to the hard phase which prevents the soft phase nucleating (reversing) at lower applied fields [41,55,57,58]. The magnetization reversal of the composite magnet is driven by the large uniaxial anisotropy of the hard phase, while the soft phase provides large remanence, if both phases are tailored in appropriate dimensions in nanoscale. This not only increases the energy product and thermal stability but also reduces the overall cost as a result of less usage of rare earth metals.

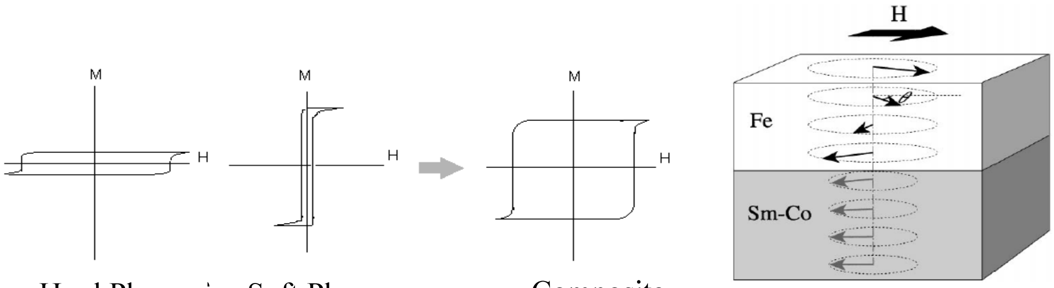

Hard Phase Soft Phase Composite

Figure 1.16 – Illustration of the principle of two phase composite magnet (adopted from ref [56])

The idea of spring-exchange magnets was first proposed by Kneller and Hawig in 1991

[55] based on the results reported by Coehoorn *et al.* for $Fe_3B/\alpha\text{-}Fe/Nd_2Fe_{17}N_2$ composites [56], which is outlined here in brief. A fundamental equation for energy product was proposed by Skomski and Coey [41].

Starting from a saturated state of a simple one dimensional model magnet with alternating soft (*m*) and hard (*k*) magnetic layers with a thickness of $2b_m$ and $2b_k$ respectively and their uniaxial anisotropies along z-direction (Figure 1.17), we can derive key equations as follows [55]. When an external field (H) is applied in the opposite direction and gradually increased, the magnetic reversal can take two pathways depending on the soft phase thickness ($2b_m$). The critical soft phase thickness ($2b_{cm}$) is the maximum possible $2b_m$, so that it's rigidly coupled to the hard phase.

If the soft phase is confined ($2b_m < 2b_{cm}$), with increasing external field the magnetic reversal attempts at the center of the soft phase. This results the energy density of the soft phase to go up but the large uniaxial anisotropy/of the hard phase (K_k) holds the soft phase from nucleation. However, it undergoes twisting away from its original direction and spans towards the external field (Figure 1.3 d). If the external field is removed the hard phase realigns the soft phase to its original direction as in a spring, so the soft phase is essentially reversible. The energy of the soft phase rises with external field and attains a maximum (maximum torsion) at the equilibrium state, but the hard phase remains unaffected. At this point, spins in soft phase are non-collinear and take the configuration of two 180^o block walls. If the field is increased beyond this equilibrium value but below the critical field (H_C), domain walls get suppressed at interfaces until they get enough energy to invade the hard region. If the external field surpasses the critical field ($H > H_C$) the hard phase can no longer hold; the equilibrium collapses and domain walls penetrate the interface to the hard phase. At this point the hard phase nucleates together with the soft phase, coherent nucleation.

If the soft layer is large, the center of the soft phase and the coupled region behave independently as the center region is not exchange hardened by the hard phase. So the nucleation starts at a lower field. Upon increasing the field, the domain walls move from the center to the interface but the process is still reversible although the soft phase is not rigidly pinned. If the soft layer is large, the center of the soft phase and the coupled region behave independently as the center region is not exchange hardened by the hard phase. So the nucleation starts at a lower field. Upon increasing the field the domain walls move from the center to the interface but the process is still reversible although the soft phase is not rigidly pinned. If the field is increased beyond its critical value, at some point the domain wall propagates through the interface to the hard region and causes a complete nucleation. However, the clear difference in this situation is that the central region and the interface-hard phase regions nucleate incoherently, hence the magnet has two nucleation fields (Figure 1.18). Since $\delta M_{(H=Hc)} = 0$, the lower nucleation field of soft phase reduces the coercivity and the energy product significantly.

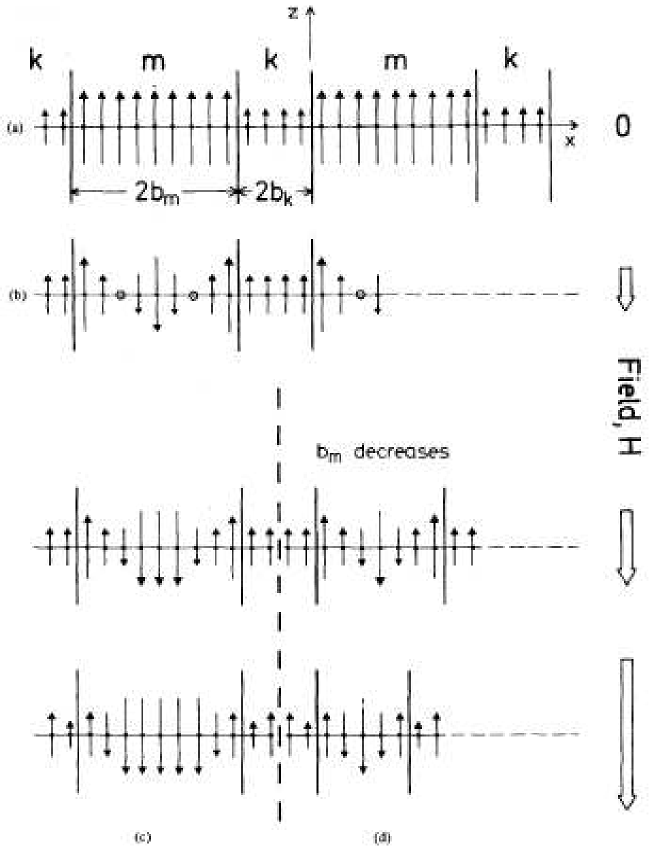

Figure 1.17 - Microstructure of the exchange-coupled composite material as a basis for the calculation of critical dimensions of phase regions a) Saturation remanence b)-c) Demagnetization in an increasing reverse field H at a constant overcritical width of the m-phase, $b_m >> b_{cm}$ d) Demagnetization at decreasing width $b_m \rightarrow b_{cm}$ (adopted from ref[55]).

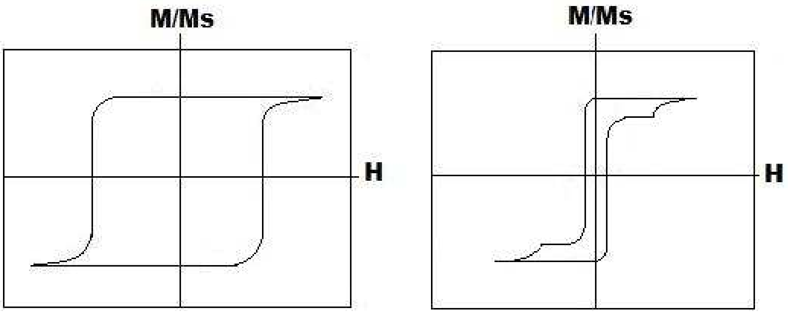

Figure 1.18 – Hysteresis of spring-exchange magnets with a) confined soft phases b) over sized soft phases.

Critical soft phase thickness (b_{cm}):

Critical soft phase thickness can be determined by reconsidering the situation where soft region is confined ($2b_m<2b_{cm}$). As mentioned before, the soft phase takes non-collinear configuration with increasing the external field. When the domain wall barely penetrates the hard phase at critical field, the hard phase acquires equilibrium configuration just before nucleation. This non-collinear configuration permits us to apply physics of domain walls to find critical soft phase thickness.

The energy per unit area of a 180° domain wall of a pure magnetic materiel is given by,

$$\gamma \simeq \delta K + \delta A\left(\frac{\pi}{\delta}\right)^2 \tag{1.14}$$

Where δ, K and A are domain wall width, anisotropy and stiffness, respectively. By taking $d\gamma/d\delta=0$, the equilibrium energy per unit area and domain wall width are given by,

$$\gamma_o = 2\pi\sqrt{A.K} \tag{1.15}$$

$$\delta_o = \pi\sqrt{\frac{A}{K}} \tag{1.16}$$

Now, let us apply this to the hard phase at critical field where the domain wall just penetrates to the hard region, at which the hard phase is considered in equilibrium. From above two equations, the energy per unit volume of the hard phase is,

$$E_{ok} = \frac{\gamma_{ok}}{\delta_{ok}} = 2K_K \tag{1.17}$$

However, the energy density of the soft region has surpassed its equilibrium value, hence it's given by,

$$E_m = \frac{\gamma_m}{\delta_m} = K_m + A_m\left(\frac{\pi}{\delta_m}\right) \tag{1.18}$$

By matching these energies at the interface,

$$2K_K = K_m + A_m\left(\frac{\pi}{\delta_m}\right) \tag{1.19}$$

Since $2b_{cm}=2\delta_m$, setting K_m~0 ($K_k >> K_m$) gives critical dimensions of soft phase.

$$b_{cm} = \pi\sqrt{A_m / 2K_K} \tag{1.20}$$

Although the critical dimensions of the hard phase can not be derived, it's believed that the hard phase thickness should be greater than its equilibrium domain wall thickness.

$$\delta_K = \pi\sqrt{A_K / K_K} \tag{1.21}$$

From energy density (eq. 1.17),

$$E_{ok} = (BH) \Rightarrow H_n = \frac{2K_K}{\mu_0 M_{eff}} \tag{1.22}$$

With,

$$M_{eff} = \nu_K M_K + (1-\nu_K) M_m \qquad (1.23)$$

Where, M_m , M_k and ν_k are remanent magnetization of soft phase and hard phase, and volume fraction of hard phase respectively. Also, H_C has an inverse square relation to soft phase dimensions.

$$H_C \approx \frac{A_m \pi^2}{2\mu_0 M_m} \frac{1}{b_m^2} \qquad (1.24)$$

Skomski and Coey showed how the energy product can substantially be increased in oriented exchange-coupled magnets. They derived analytic results for energy product and nucleation field by minimizing the free energy F [41].

$$F = \int \left[A(r).\left(\frac{\nabla m}{M_S}\right)^2 - K(r).\frac{(M.n)^2}{M_S^2} - \mu_0 MH \right].dr \qquad (1.25)$$

The nucleation field ($H_C \geq H_N$) is given by,

$$H_N = \frac{2\left[\nu_K K_K + \nu_m K_m\right]}{\mu_0\left[\nu_K M_K + \nu_m M_m\right]} \qquad (1.26)$$

$$K_{eff} = \nu_K K_K + \nu_m K_m \qquad (1.27)$$

Where ν_k, ν_m are volume fractions of hard and soft regions.

The energy product is given by,

$$(BH)_{\max} = \frac{1}{4}\mu_0 M_m^2 \left[1 - \frac{\mu_0 (M_m - M_K) M_m}{2K_K} \right] \tag{1.28}$$

Maximum *(BH)max* is obtained when all domains are aligned in one direction, which corresponds to an ideal rectangular hysteresis loop with the theoretical *(BH)max* of $\frac{1}{4}\mu_0 M_S^2$, where μ_0 is the permeability of free space. If hard phase is thinner than its equilibrium domain wall thickness, soft regions would interact and can destroy the coercivity, as illustrated in Figure 1.19.

Therefore, to obtain the maximum energy product, spring-exchange magnet should be carefully engineered with proper dimensions of soft and hard phases. As an example, for a $SmCo_5$/Co bi-layer, the Co thickness should be 5 nm or smaller and $SmCo_5$ layer thickness should be greater than 5 nm for a single nucleation field.

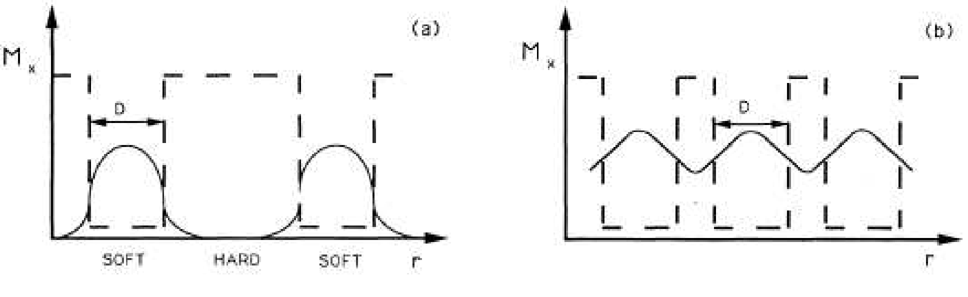

Figure 1.19 – Effect of interaction between soft regions when distances between soft regions are (a) large (b) small (adopted from ref [41])

$(BH)_{max}$ values as high as 110 MGOe and 137 MGOe have been predicted for $Sm_2Fe_{17}N_3$/Fe and $Sm_2Fe_{17}N_3/Fe_{65}Co_{35}$ bi-layer systems with volume fractions of hard phases as little as 7% and 9%, respectively. These values are about two times as high as the current record of 64 MGOe for $Nd_2Fe_{14}B_2$. However, in practice such high values have not been obtained due to partially aligned or isotropic grains, and complicated magnetization dynamics instead of coherent reversal. In principle, when grains are randomly oriented, the effective magnetization is about half of its oriented version [55]. This reduces the $(BH)_{max}$ as a result of $(BH)_{\max} \propto M^2$.

1.7 Antiferromagnetism and Exchange Bias Effect

Antiferromagnetic (AFM) arrangement occurs when the exchange integral J_{ij} between neighboring atoms is negative, which favors magnetic spins to align anti-parallel to each other, resulting zero net magnetization at 0 K. However, non-zero magnetic moments have been observed for certain antiferromagnetic materials at low temperatures due to spin canting [59,60], a slight tilt from co-parallel axis due to antisymmetric exchange interaction [6]. As in ferromagnetic materials, antiferromagnetic materials also have a characteristic temperature called Neel temperature T_N, above which the material loses anti-parallel arrangement and takes a random arrangement. To incur antiferromagnetic ordering, the material should be cooled from higher temperature ($>T_N$) in the presence of a magnetic field through its T_N.

The exchange bias effect is defined as the unidirectional alignment of a ferromagnetic phase by an adjacent antiferromagnetic phase. This unidirectional preference can be observed in hysteresis loop by an offset in field axis that results unequal coercivities H_{C1} and H_{C2} (Figure 1.20), suggesting that magnetic moments preferentially align along one direction on the easy-axis. Exchange bias effect has been observed in variety of systems including bi-layer, multilayer thin films and core-shell nanoparticles [61]. This phenomenon was discovered in 1956 by Meiklejohn and Bean in Co-CoO particles [62], and employed in applications as early as in 1970s with IBM's magnetoresistance recording head.

Origin of exchange bias effect is the exchange interaction between the ferromagnetic (FM) and antiferromagnetic (AFM) phases at the interface. AFM materials, if cooled down from high temperature through it's T_N in the presence of a field (field cooling), have almost zero magnetic moment. So, no change in spin configuration can be expected in AFM phase when an external magnetic field is applied. On the other hand, adjacent FM phase responds to the external field however, the exchange interaction it has with uncompensated spins of AFM phase creates a pinning effect at the interface.

As the FM spins are exchanged hardened by the exchange coupling and essentially creates Neel domain wall at the interface, this extra energy results a larger coercive field (H_C). But when a negative external field is applied, the exchange-spring at the interface supports the reversal process in addition to the external field, creating the reversal more economical. This results a lower coercive field and the hysteresis is appeared to be biased towards one direction that makes magnetic moments unidirectional along the easy-axis instead of uniaxial.

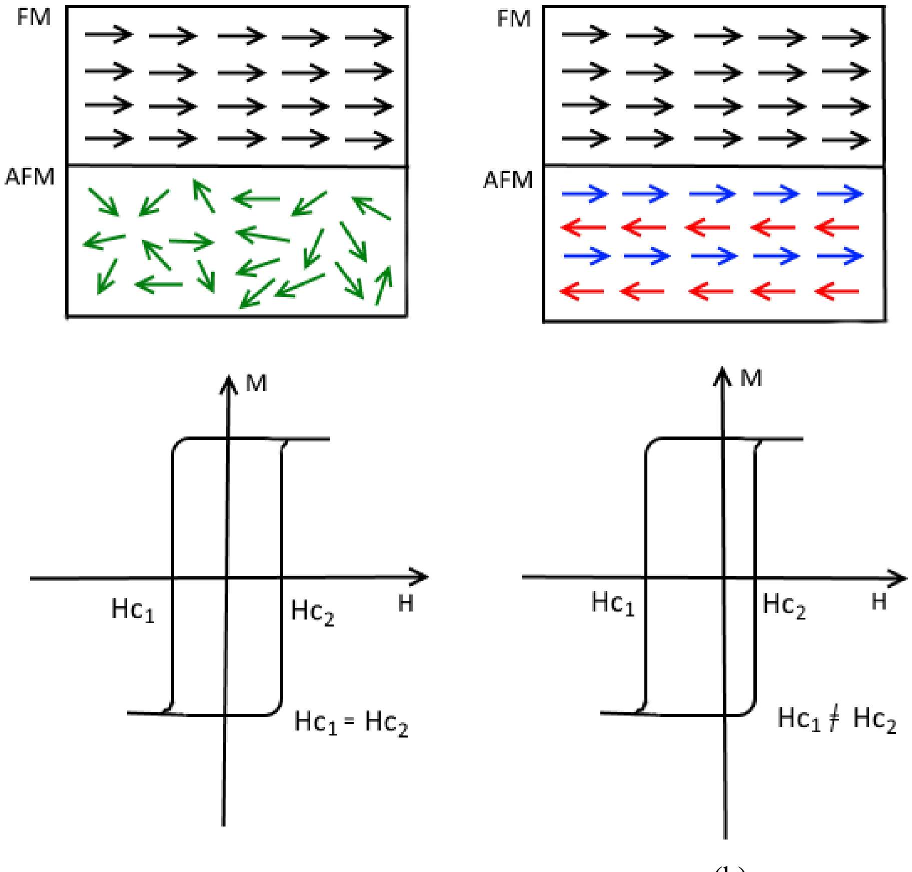

(a) (b)

Figure 1.20 - Phenomenological model of an exchange bias bilayer system. a) Spin arrangement of the system at high temperature ($>T_N$) or when AFM phase is not field cooled through T_N. Hysteresis loop is symmetric due to the absence of exchange bias effect. b) Spin arrangement of the system when AFM material is ordered ($T < T_N$).

Further, it is possible to observe a vertical shift in hysteresis as the magnetic moment slightly changed due to pinning effect. The exchange bias field H_{EB} is the offset of the hysteresis and given by,

$$H_{EB} = \frac{H_{C1} + H_{C2}}{2} \tag{1.29}$$

Despite the fact that exchange bias effect was discovered in 1956, there is still no complete theoretical understanding of the phenomenon in all cases. The first model to explain exchange bias effect is proposed by Meiklejohn and Bean (MB theory) [61, 62]. Although the model predicted values are off orders of magnitudes found in experiments, it gives a phenomenological understanding about the exchange bias effect. The model was developed based on following assumptions.

- FM/AFM interface is atomically smooth
- FM and AFM are single domains
- AFM interface is fully uncompensated and has in-plane uniaxial anisotropy
- AFM phase is magnetically rigid (not affected by external *B* field) while FM phase rotates coherently.
- FM/AFM coupled by exchange interaction across the interface.

Since the model assumes coherent rotation and single domain state, Stoner-Wolfwarth model can be applied to interfacial spins. If the anisotropy axis of both AFM and FM phases are parallel to the interface (Figure 1.21), the energy per unit area is given by [63],

$$E = -\mu_0 H M_F t_F \cos(\theta - \beta) + K_F t_F \sin^2 \beta - J_{EB} \cos \beta \tag{1. 30}$$

Where, M_F, t_F and K_F are magnetization, thickness and anisotropy of the ferromagnetic material, respectively.

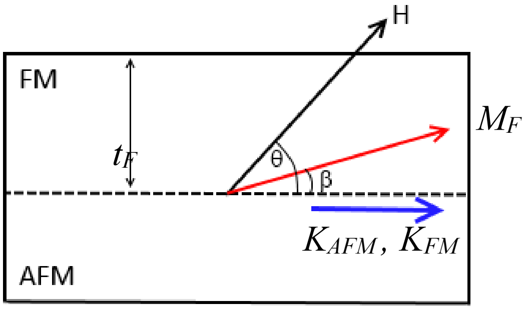

Figure 1.21 - Stoner-Wohlfarth model for exchange bias system after field cooling along the interface (easy axis).

Taking $\partial E/\partial\theta = 0$ and $\partial E/\partial\beta = 0$, and setting $\theta=0$ for field applied along interface, equations for H_{C1} and H_{C2} can be obtained for $\beta=0$ and π.

$$H_{C1} = \frac{-2K_F t_F - J_{EB}}{\mu_0 M_F t_F} \tag{1.31}$$

$$H_{C2} = \frac{2K_F t_F - J_{EB}}{\mu_0 M_F t_F} \tag{1.32}$$

So the exchange bias field is given by,

$$H_{EB} = \frac{-J_{EB}}{\mu_0 M_F t_F} \tag{1.33}$$

The above equation shows that the exchange bias is a surface effect as H_{EB} is indirectly proportional to the FM layer thickness ($H_{EB} \propto 1/t_F$), so the effect is only realistic for thin films. However, experiments reveal that epitaxially grown films which have smooth interfaces have lower H_{EB} in comparison to rough interfaces. This shows that interfacial defects play a major role. Newer models have been proposed by taking the random nature of the interface, continuity at the interface and domain formation in AFM phases into consideration, that predicts reasonably accurate results [61,63-65]. One such model is Mauri-Siegmann model that predicts the maximum values of H_{EB} is given by [61],

$$H_{EB} = \frac{J_{EB} S_{AFM} S_{FM}}{\xi a M_F t_F} \tag{1.34}$$

Where S_{AFM} and S_{FM} are spin densities of FM and AFM phases at the interface, and ⌧ and a are interface thickness and in-plane atomic separation, respectively.

Also, as in ferromagnetic particles, exchange-bias systems have blocking temperatures T_B, above which the exchange bias effect disappears. T_B of the AFM material is governed by the size of AFM phase. For thicker films, T_B and T_N are closer ($T_N \approx T_B$) however, T_B of thinner films can be much smaller than the T_N [63, 66].

1.8 Reference

[1] Magnetism in Condensed Matter (Oxford Master Series in Physics) (06 December 2001) by Stephen Blundell.

[2] Introduction to Solid State Physics, Charles Kittal, 7th edition.

[3] Kimling, J., PhD Dissertation, Hamburg University (2013).

[4] Negishi, Y., Tsunoyama, H., Suzuki, M., Kawamura, N., Matsushita, M. M., Maruyama, K., Tsukuda, T., *Journal of the American Chemical Society*, *128*(37), 12034-12035 (2006).

[5] Michael, F., Gonzalez, C., Mujica, V., Marquez, M., Ratner, M. A., *Physical Review B*, *76*(22), 224409 (2007).

[6] Maitra, U., Das, B., Kumar, N., Sundaresan, A., Rao, C. N. R., *ChemPhysChem* *12*(12), 2322-2327 (2011).

[7] Dutta, P., Pal, S., Seehra, M. S., Anand, M., Roberts, C. B., *Applied Physics Letters*, *90*(21), 213102-213102 (2007).

[8] Luo, W., Pennycook, S. J., Pantelides, S. T., *Nano Letters*, 7, 3134 (2007).

[9] Hurd, C. M., Shiozaki, I., McAlister, S. P., *Physical Review B*, *26*(2), 701 (1982).

[10] Kato, M., Nishino, Y., Mizutani, U., Asano, S., *Journal of Physics: Condensed Matter*, *12*(8), 1769 (2000).

[11] James, P., Eriksson, O., Johansson, B., Abrikosov, I. A., *Physical Review B*, *59*(1), 419 (1999).

[12] Schrefl, T., Fischer, R., Fidler, J., Kronmüller, H., *Journal of Applied Physics*, *76*(10), 7053-7058 (1994).

[13] Skomski, R. (2008). *Simple models of magnetism*. Oxford: Oxford University Press.

[14] Coey, J. M. (2010). *Magnetism and magnetic materials*. Cambridge University Press.

[15] Sayama, J., Asahi, T., Mizutani, K., Osaka, T., *Journal of Physics D: Applied Physics*, *37*(1), L1 (2004).

[16] Herbst, J. F., Croat, J. J., Pinkerton, F. E., Yelon, W. B., *Physical Review B*, *29*(7), 4176 (1984).

[17] N. D. The, Master Thesis, Vietnam National University (2006).

[18] Elmers, H. J., and U. Gradmann., *Surface Science* 193(1) 94-108 (1988).

[19] Gradmann, U., T. Dürkop, and H. J. Elmers., *Journal of magnetism and magnetic materials* 168(3), 94-108 (1997).

[20] Bruno, P., J-P. Renard., *Applied Physics A: Materials Science & Processing* 49(5), 499-506 (1989).

[21] Dubowik, J., *Physical Review B* 54(2), 1088 (1996).

[22] Zhang, L. N., Hu, J. F., Chen, J. S., Ding, J., *Journal of Magnetism and Magnetic Materials*, *321*(17), 2643-2647 (2009).

[23] Saravanan, P., Hsu, J. H., Reddy, G. L. N., Kumar, S., Kamat, S. V., *Journal of Alloys and Compounds*, *574*, 191-195 (2013).

[24] Sayama, J., Mizutani, K., Asahi, T., Osaka, T., *Applied Physics Letters*,*85*(23), 5640-5642 (2004).

[25] Seifert, M., Neu, V., Schultz, L., *Applied Physics Letters*, *94*(2), 022501-022501 (2009).

[26] Fritzsche, H., Kohlhepp, J., Gradmann, U., *Physical Review B*,*51*(22), 15933 (1995).

[27] Bhowmik, R. N., Ranganathan, R., Nagarajan, R., Ghosh, B., Kumar, S., *Physical Review B*,*72*(9), 094405 (2005).

[28] Vaz, C. A. F., Bland, J. A. C., *Physical Review B*, *61*(4), 3098 (2000).

[29] Rusponi, S., Cren, T., Weiss, N., Epple, M., Buluschek, P., Claude, L., Brune, H., *Nature Materials*,*2*(8), 546-551 (2003).

[30] Liedke, M. O., Körner, M., Lenz, K., Fritzsche, M., Ranjan, M., Keller, A., Fassbender, J., *Physical Review B*, *87*(2), 024424 (2013).

[31] Bisio, F., Moroni, R., de Mongeot, F. B., Canepa, M., Mattera, L., *Physical review letters*, *96*(5), 057204 (2006).

[32] Rusponi, S., Cren, T., Weiss, N., Epple, M., Buluschek, P., Claude, L., Brune, H., *Nature Materials*,*2*(8), 546-551 (2003).

[33] Zavaliche, F., Zheng, H., Mohaddes-Ardabili, L., Yang, S. Y., Zhan, Q., Shafer, P., Ramesh, R., *Nano letters*, *5*(9), 1793-1796 (2005).

[34] Mangin, S., Ravelosona, D., Katine, J. A., Carey, M. J., Terris, B. D., Fullerton, E. E., *Nature Materials*, *5*(3), 210-215 (2006).

[35] Zheng, H., Skomski, R., Menon, L., Liu, Y., Bandyopadhyay, S., Sellmyer, D., *Physical Review B* 65 (2002).

[36] Parkin, S. S., Hayashi, M., Thomas, L., *Science*, *320*(5873), 190-194 (2008).

[37] Chappert, C., Bernas, H., Ferré, J., Kottler, V., Jamet, J. P., Chen, Y., Launois, H., *Science*, *280*(5371), 1919-1922 (1998).

[38] Huse, D. A., Henley, C. L., *Physical review letters*, *54*(25), 2708 (1985).

[39] Burrowes, C., Mihai, A. P., Ravelosona, D., Kim, J. V., Chappert, C., Vila, L., Attané, J. P., *Nature Physics*, *6*(1), 17-21 (2009).

[40] Boulle, O., Kimling, J., Warnicke, P., Kläui, M., Rüdiger, U., Malinowski, G., Faini, G., *Physical review letters*, *101*(21), 216601 (2008).

[41] Skomski, R., Coey, J. M. D., *Physical Review B* 48(21) 15812 (1993).

[42] Sawaga, M., Fujimura, S., Togawa, N., Yamamoto, H., *Journal of Applied Physics* 55 2083 (1984).

[43] Croat, J. J., Herbst, J. F., Lee, R. W., Pinkerton, F. E., *Journal of Applied Physics* 55 2078 (1984).

[44] Farrow, R. F. C., Weller, D., Marks, R. F., Toney, M. F., Cebollada, A., Harp, G. R., *Journal of Applied Physics*, *79*(8), 5967-5969 (1996).

[45] Visokay, M. R., Sinclair, R., *Applied Physics Letters* 66(13) 1692-1694 (1995).

[46] Yan, M. L., Sabirianov, R. F., Xu, Y. F., Li, X. Z., Sellmyer, D. J., *IEEE Transactions on Magnetics*, *40*(4), 2470-2472 (2004).

[47] Visokay, M. R., Bruce M. L., Sinclair, R., U.S. Patent No. 5,603,766 (1997).

[48] Sun, S., Murray, C. B., Weller, D., Folks, L., Moser, A., *Science*, *287*(5460), 1989-1992 (2000).

[49] Miura, Y., Ozaki, S., Kuwahara, Y., Tsujikawa, M., Abe, K., Shirai, M., *Journal of Physics: Condensed Matter*, *25*(10), 106005 (2013).

[50] Kotsugi, M., Mizuguchi, M., Sekiya, S., Ohkouchi, T., Kojima, T., Takanashi, K., Watanabe, Y., *Journal of Physics: Conference Series* 266 (1) 012095 (2011).

[51] Kotsugi, M., Mizuguchi, M., Sekiya, S., Mizumaki, M., Kojima, T., Nakamura, T., Watanabe, Y., *Journal of Magnetism and Magnetic Materials*, *326*, 235-239 (2013).

[52] Ji, N., Lauter, V., Sun, C. J., Allard, L. F., Ambaye, H., Heald, S. M., Wang, J. P., *arXiv preprint arXiv:1211.0553* (2012).

[53] Ji, N., Liu, X., Wang, J. P., *New Journal of Physics*, *12*(6), 063032 (2010).

[54] Constantinides, S., *The demand for rare earth materials in permanent magnets*, Arnold Magnetic Technologies.

[55] Kneller, E. F., Hawig, R*., IEEE Transactions on Magnetics*, *27*(4), 3588-3560 (1991).

[56] Coehoorn, R., De Mooij, D. B., De Waard, C., *Journal of Magnetism and Magnetic Materials*, *80*(1), 101 (1989).

[57] Fullerton, E. E., Jiang, J. S., Bader, S. D., *Journal of Magnetism and Magnetic Materials*, *200*(1), 392-404 (1999).

[58] Fullerton, E. E., Jiang, J. S., Grimsditch, M., Sowers, C. H., Bader, S. D., *Physical Review B*, *58*(18), 12193 (1998).

[59] Morales, M. P., Veintemillas-Verdaguer, S., Montero, M. I., Serna, C. J., Roig, A., Casas, L., Sandiumenge, F., *Chemistry of Materials*, *11*(11), 3058-3064 (1999).

[60] Parker, F. T., Foster, M. W., Margulies, D. T., Berkowitz, A. E., *Physical Review B*, *47*(13), 7885 (1993).

[61] Stöhr, J., Siegmann, H. C., Magnetism. *Solid-State Sciences. Springer, Berlin, Heidelberg*, 5 (2006).

[62] Meiklejohn, W. H., Bean, C. P., *Physical Review*, *105*(3), 904 (1957).

[63] Radu, F., Zabel, H., *Magnetic heterostructures*. Springer Berlin Heidelberg, 97-184 (2008).

[64] Nogués, J., Schuller, I. K., *Journal of Magnetism and Magnetic Materials*, *192*(2), 203-232 (1999).

[65] Kiwi, M., *Journal of Magnetism and Magnetic Materials*, *234*(3), 584-595 (2001).

[66] Ali, M., Marrows, C. H., Al-Jawad, M., Hickey, B. J., Misra, A., Nowak, U., Usadel, K. D., *Physical Review B*, *68*(21), 214420 (2003).

CHAPTER 2

MAGNETIZATION REVERSAL OF ORIENTED MAGNETIC THIN FILMS WITH LARGE IN-PLANE UNIAXIAL ANISOTROPY

This chapter discusses high-throughput fabrication and characterization of densely packed Fe nanostripe-based magnetic thin film samples. This starts with an introduction to previous work and concepts related to the study, followed by the fabrication process, material and magnetic characterization and micromagnetic simulations. In this study, samples exhibit large in-plane uniaxial anisotropies and nearly square hysteresis loops at room temperature. Also, the anisotropy dependence on film thickness, the effect of dipolar interactions and the reversal mechanism were investigated.

2.1 Introduction

Thin films based on arrays of densely packed magnetic nanostripes are of great interest in novel applications and fundamental studies as they exhibit unique properties with greater designed controllability than those of their bulk counterparts. They are widely used in studying domain wall dynamics induced by current and fields [1-3] due to their potential use in applications such as information storage and logic devices [4, 5-7], cell biology [8] and more recently in manipulating superconductivity [9]. Fabrication of nanostripe samples has been achieved by utilizing both top down and bottom up techniques. Although bottom up methods such as epitaxial growth can produce nanostructures with ultrasmall dimensions compared to traditional lithography based methods, their usage is limited due to requirement of ultra-high vacuum conditions and restrictive lattice match between the substrate and materials. In addition, such epitaxially grown samples show room temperature superparamagnetism [10,11] due to size effects, and are sensitive to defects. Borca *et. al.* employed sequential pulse laser deposition technique to epitaxially grow ultrafine nanostripes on single crystal sapphire and Mo substrates [10,12], however observed blocking temperatures T_B were under 175 K. Tripati *et al* [13] fabricated self-assembled α-FeSi$_2$ nanostripes, using solid phase epitaxy of a monolayer of Fe on vicinal Si(111) followed by annealing at 550 °C. Magnetic measurements revealed that these nanostripes are superparamagnetic at room temperature.

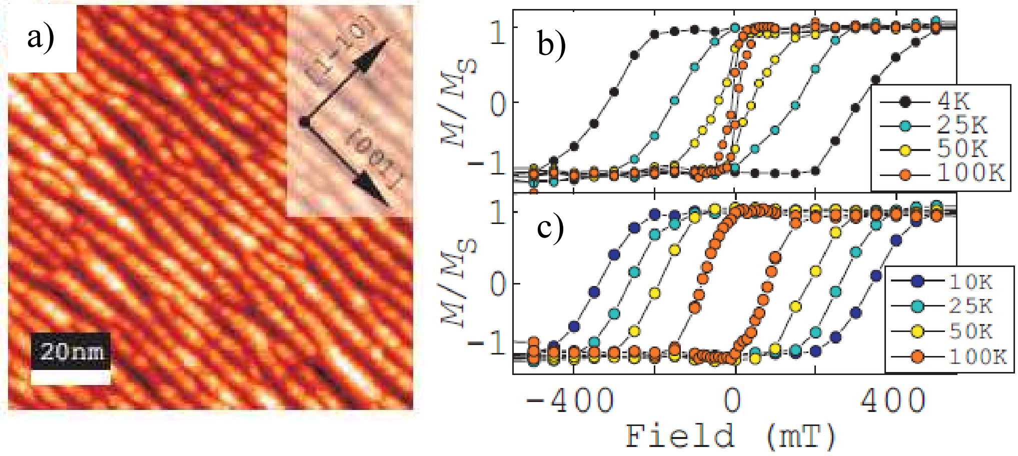

Figure 2.1 - Induce of shape anisotropy of Fe by the W underlayer. a) STM image (100 nm x 100 nm) of the W(110) grown on Mo/Sapphire substrate and b) hysteresis curves at varies temperatures of Mo/Fe/W and Mo/Fe/Mo/W multilayer samples (ref [12]).

In contrast, template based methods have been explored and remain popular for their high precision and great designed controllability, although such techniques usually result nanostructures with larger dimensions. Shallow angle deposition of materials onto pre-patterned/vicinal templates is one common route exploited by many researchers. In this method, materials are deposited at smaller angles (< 4^0) such that the deposition flux directed towards one side of the terrace while the other side being masked. Arora *et al.* [14, 15] followed this technique to fabricate Co nanostripe thin films which exhibited room temperature ferromagnetism with in-plane coercivities as high as 920 Oe. However, one drawback of this technique is that the step height is only a few nanometers, so observed properties are realistic for low material thickness (< 10 nm). This results samples with lower magnetic moments. Li *et al* [16] fabricated a range of Co nanostructures including nanostripes of 1.5 μm by microcontact printing using polymer based molds.

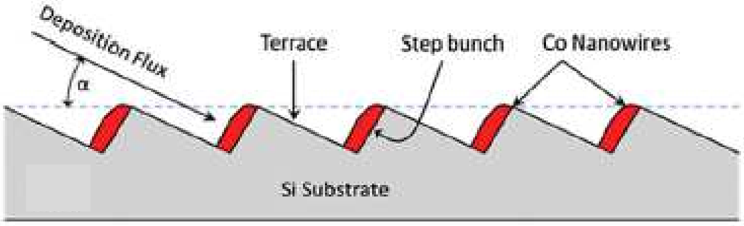

Figure 2.2 - Schematic of deposition geometry of shallow angle deposition technique. The Co flux is directed towards the uphill direction of the miscut of Si(111) substrate (ref [14]).

In the current study, a novel method suitable for a high volume device manufacturing, UV assisted nanoimprint lithography (NIL) with the roll-to-roll option has been used for nanostripe patterning on a flexible plastic substrate. The main advantage of NIL was high volume production of sub 100 nm scale nanostructures.

2.2 Sample Fabrication

Fe-nanostripe based thin films were fabricated by physical vapor deposition of Fe on topographical gratings on a substrate made by custom made roll-to-roll nanoimprinter housed in the UMass Nanoimprint Lithography Laboratory. The choice of substrate was polyethylene terephthalate (PET) due to its ready availability, flexibility, mechanical and chemical stability and ultra-low cost in comparison to silicon wafer substrates. These properties make PET an attractive candidate for mass production by direct patterning with roll-to-roll nanoimprint lithography for high-throughput device fabrication. Here, the grating width and the depth were fixed at 70 nm and 50 nm, respectively. A schematic representation of roll-to-roll nanoimprinting process is shown in Figure 2.3 (a). The stamp is made from perfluoropolyether acrylate (PFPE) mold on PET using a Si master mold, which made it flexible to use in the roll-to-roll process. The UV photoresist employed was Norland 81 (Norland Inc., USA) and was used as received. A detailed description of the roll-to-roll NIL process can be found elsewhere [17].

To fabricate magnetic nanostripe thin films on PET gratings, a thin layer of Fe (5 nm - 45 nm) was deposited by electron beam evaporation (CHA SE-600 electron beam evaporator) at normal incidence in high vacuum of 5×10^{-7} torr. A 3 nm layer of Ag was also deposited on Fe film as a capping layer to protect Fe from oxidation. Deposition rates were kept constant at 0.05 nm/s for all samples to promote continuous films. Films were also deposited on planar PET pieces with the same dimensions under identical deposition conditions as a control.

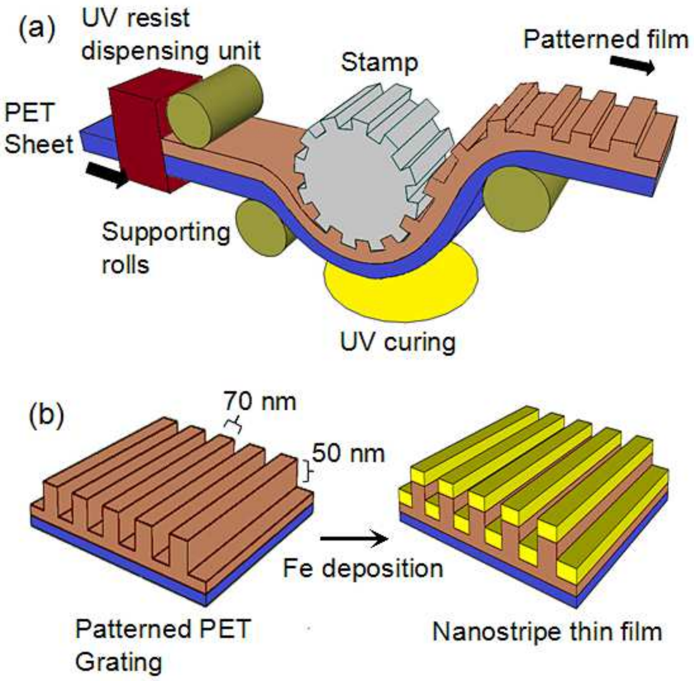

Figure 2.3. a) Schematic representation of the UV-assisted roll-to-roll nanoimprint lithography process used in this work and b) fabrication of nanostripe-based thin film by metal evaporation.

2.3 Structural Characterization

The sample surface and microstructure were analyzed with atomic force microscopy (AFM) and scanning electron microscopy (SEM). For AFM studies, Vecco Nanoscope IV equipment with TESPA-V2 tapping mode probes was used, and image data were analyzed by NanoScope Analysis v1.4 (Bruker, Inc.) software. For SEM studies, a JOEL 7001F thermal field emission electron microscope has been used. Figure 2.5 shows AFM and SEM figures of a 15 nm thick Fe nanostripe array.

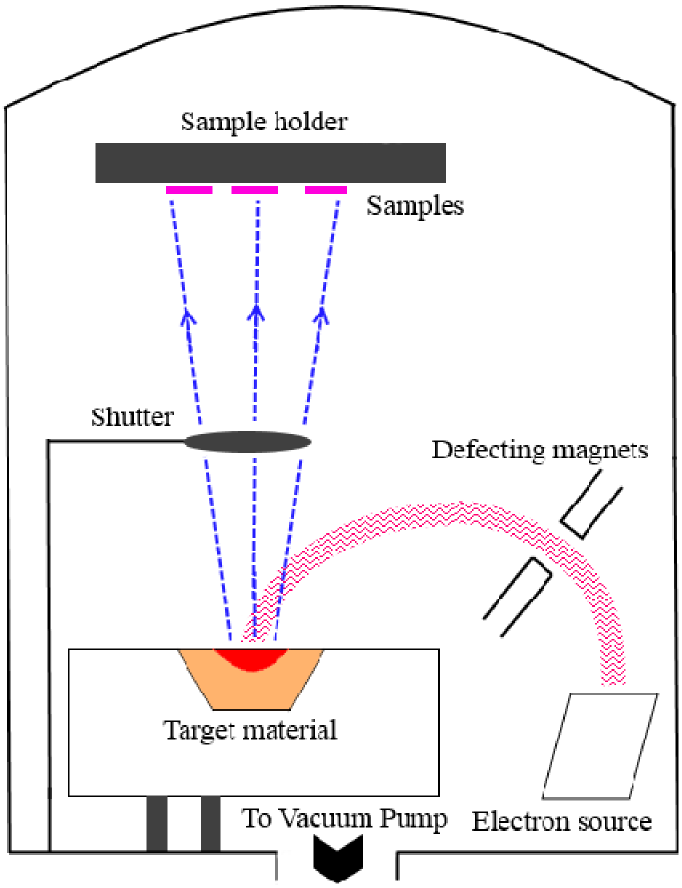

Figure 2.4 - Schematic representation of electron beam evaporation. The target is heated by the electron beam that results an emission of material vapor that solidifies upon interacting with the samples.

It can be seen that the nanostripes are mostly continuous with a few discontinuities as a result of defects on the grating. Further, AFM measurements confirm that there is a noticeable roughness of +/- 3 nm which could have originated from grating imperfections, dewetting between Fe and PET and the deposition itself. The cross section SEM image shows material deposition that also forms narrower nanostripes on sidewalls. Further, Figure 2.6 shows the microstructure of nanostripes of 15 nm thick Fe layer. The average grain size of Fe is 40 nm.

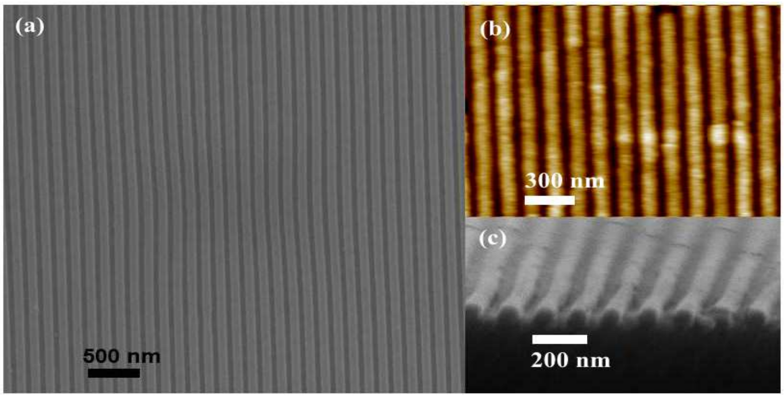

Figure 2.5 a) SEM and b) AFM and c) Cross section SEM micrographs of 30 nm Fe nanostripe thin film. SEM and AFM figures suggest that these films have a noticeable roughness and cross section SEM shows the material deposition on sidewalls.

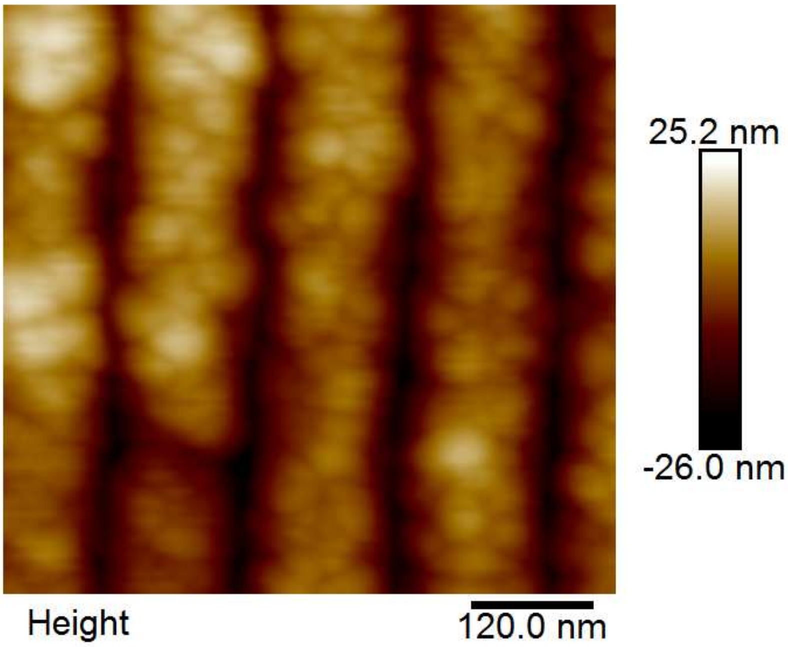

Figure 2.6 - High resolution AFM micrograph of 15 nm thick Fe nanostripes. The average grain size is 40 nm.

Elemental analysis of selected samples were performed by X-ray photoelectron spectroscopy (XPS) and the spectrum was acquired from Physical Electronics PHI 5000 dual anode/fixed lens spectrometer equipped with a monochromatic Al X-ray source. Survey spectra were taken to check the presence of any impurities and subsequent high resolution spectra in the 700-735 eV range were acquired to check the oxidation state of Fe. The data were analyzed using PHI MultiPak software. Figure 2.7 shows the XPS spectra of 15 nm Fe thin film capped with a 3 nm Ag layer. The sample was sputter etched with Ar at 4 keV for 5 and 30 seconds to do a depth profiling. As shown, top layer (or the surface) Fe layer is oxidized to Fe_2O_3 while the interior still has elemental Fe. This shows that a 3 nm Ag capping layer is not thick enough to protect the magnetic material from oxidation. Also the exchange interaction between Fe_2O_3 and Fe phases can create an exchange bias system below a critical temperature as Fe_2O_3 is antiferromagnetic with T_N~260 K, however it's insignificant if the antiferromagnetic region (Fe_2O_3) is too thin in comparison to ferromagnetic region (Fe).

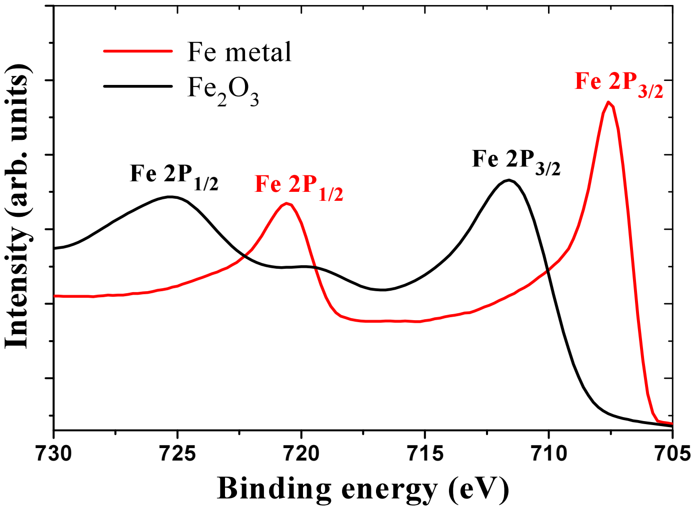

Figure 2.7 - XPS spectra of 15 nm Fe nanostripe sample capped with a 3 nm Ag layer. The sample was sputter etched for 5 s (black) and 30 s (red) to analyze the interface and the interior region, respectively.

2.4 Magnetic Measurements

Magnetic properties were measured by Superconducting Quantum Interference Device (SQUID) magnetometer with a 7 T maximum applied field (MPMS XL-7, Quantum Design). Thin film samples were diced into 3 mm x 3 mm pieces to measure in-plane magnetic properties along (parallel) and across (perpendicular) the long dimension of the nanostripes at various temperatures from 10 K to 300 K. Samples were first saturated at 500 Oe for 60 seconds to align magnetic moments in one direction prior to take magnetic measurements. Figure 2.8 shows the hysteresis curves measured along and across nanostripes for 30 nm thick Fe sample. These measurements reveal that the easy axis lies parallel to nanostripes as a result of uniaxial anisotropy induced by the shape anisotropy due to elongated shape.

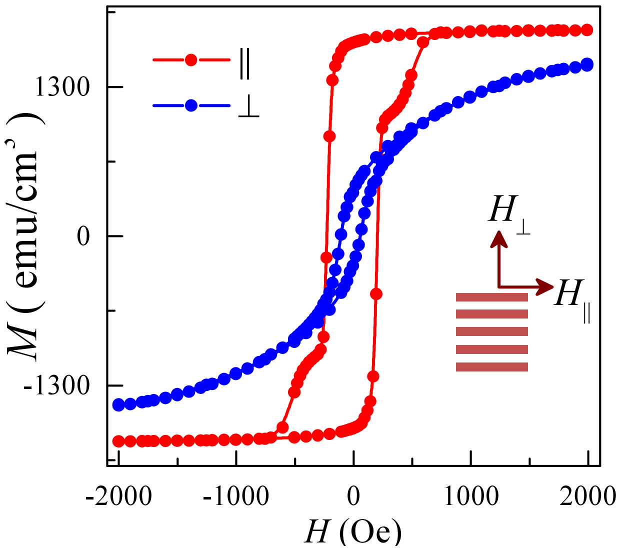

Figure 2.8 - M-H curve for 30 nm Fe nanostripe thin films measured parallel and perpendicular to nanostripes at 300 K.

Figure 2.9 shows demagnetization curves of nanostripe and planar samples. As shown in both Figure 2.9 and Figure 2.10, the coercivity (H_C) has a clear thickness dependence which first increases with the Fe nanostripe thickness from 194 Oe at 5 nm to reach the maximum of 257 Oe at 15 nm, and gradually decreases to 162 Oe at 45 nm. The maximum energy product $(BH)_{max}$ values also follow the same trend giving a maximum of 3.5 MGOe for the 15 nm thick nanostripe sample. This variation of H_C with the thickness for thin nanostripes is in line with previous reports [14, 18, 19].

The low in-plane H_C in the 5-15 nm Fe thickness regime can come from the effect of surface anisotropy as it plays a dominant role in thin films and favors out-of-plane magnetic orientation (see chapter one).

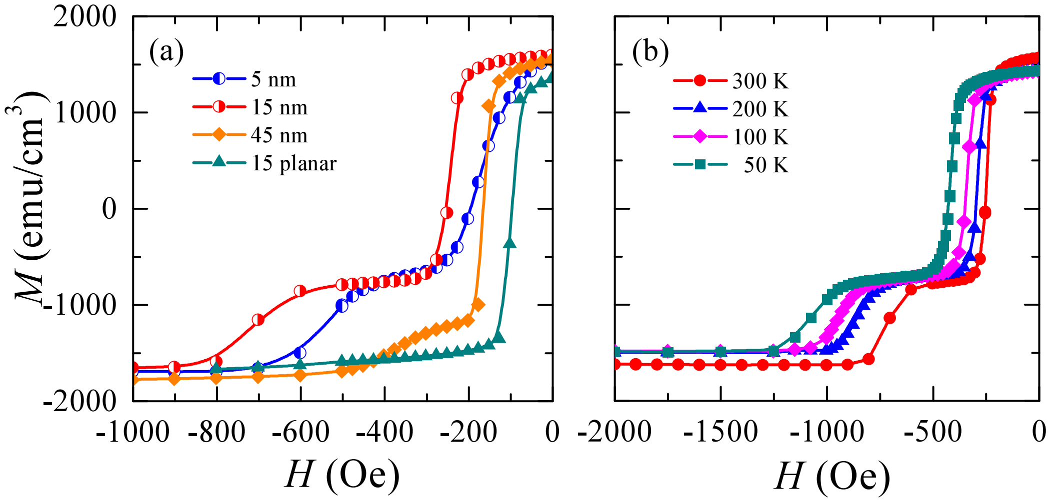

Figure 2.9 - Demagnetization curves of a) 5, 15, 45 nm thick nanostripe films (field applied along the long-axis of nanostripes) and 15nm thick planner film at 300K and b) 15 nm nanostripe film at different temperatures. Only the second and third quadrant of the hysteresis loop is shown for the clarity. The H_C of nanostripe samples are significantly higher than those of planer samples. Nanostripe with 15 nm Fe layer has the highest coercivity, and the coercivity of samples rises with reducing the temperature.

In addition, as evident by AFM figures discussed in the previous section, these nanostripes have a noticeable roughness due to grating imperfections and possible dewetting conditions between Fe and PET. The latter effect can result isolated-like nanograins with no ferromagnetic coupling for thinner Fe layers, which minimizes the effect of shape anisotropy hence reduces the coercivity. In order to interpret the decrease in H_C for thicker nanostripes (> 15 nm), we need to consider the influence of magnetic dipolar interactions to the reversal process, as such interactions promote antiparallel alignment of the magnetization in neighboring nanostripes. First, consider the state where all nanostripes are homogeneously magnetized in the same direction with magnetic charges at both ends, $\sigma=|M|$. If N nanostripes are reversed by dipolar interactions, assuming each reversal reduces the total magnetostatic energy by E_V, the interaction

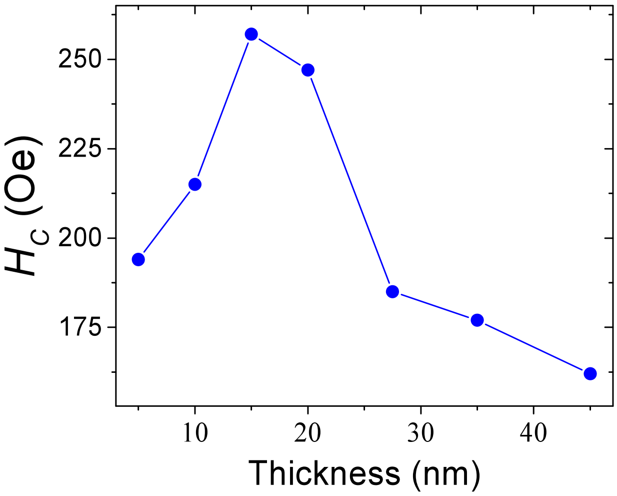

Figure 2.10 - Thickness dependence of the coercivity (H_C) of nanostripes samples with field applied along the long axis at 300 K. H_C increases with Fe layer thickness up to 15 nm and decreases due to effect of dipolar interactions which increases with the layer thickness.

energy between two nanostripes, the effective coercivity of the sample can be given by [14, 20]

$$H_C = \frac{2K}{\mu_0 M_S}\left[1 - \left(\frac{N|E_V|}{K}\right)^{\frac{1}{2}}\right] \tag{2.1}$$

Where the prefactor $2K/\mu_0 M_S$ denotes the intrinsic coercivity due to anisotropy K, of an isolated nanostripe. For a pair of interacting cylindrical nanowires, the E_V is given by,

$$E_V = \left(\frac{\mu_0}{8\pi}\right) M_1 M_2 \left(\frac{D}{L}\right)\left(\frac{d}{D}\right)^2\left[1 - \left(1 + \left(\frac{L}{D}\right)^2\right)^{-\frac{1}{2}}\right] \qquad (2.\ 2)$$

Where d, D and L are diameter, center-to-center wire distance and length respectively, and M_1 and M_2 are the axial components of magnetization along the long axis of each nanostripe. For a constant D, the E_V increases with the diameter of nanowire or with the thickness of a rectangular nanostripe with a constant width. Thus, equation (1) and (2) manifest a reduction in H_C with increasing the nanostripe thickness, which explains the observed reduction in H_C from 15 nm to 45 nm samples. Table 1 shows the reduced remanence (M_r/M_S), coercivity (H_C) and maximum energy product $(BH)_{max}$ values for nanostripe samples of 5 - 45 nm Fe thickness.

As expected for large aspect ratio nanostripes, the hysteresis loop along the long axis is closer to a square and reduced remanence (M_r/M_S) is closer to 1 for all thicknesses except 5 nm sample which is very sensitive to template roughness and imperfections.

Table 2.1- Reduced remanence (Mr/M_S), coercivity (Hc) and maximum energy product (BH_{max}) for Fe nanostripe samples with 5 - 45 nm thickness (*t*).

Sample	***t* (nm)**	**M_r/M_S**	**H_C (Oe)**	**BH_{max} (MGOe)**
1	5	0.78	194	1.5
2	10	0.89	215	2.2
3	15	0.96	257	3.5
4	20	0.96	247	3.1
5	27.5	0.92	185	2.7
6	35	0.87	177	2.3
7	45	0.86	162	2.1

However, the observed switching field values fall well below the theoretical values given by $2\pi M_S$ (for Fe, $2\pi M_S$ = 10.8 kOe), suggesting that the reversal is not governed by coherent reversal mode. In addition, the temperature dependent hysteresis measurements (Figure 2.9 b) show that the shape-dominated uniaxial anisotropy has an inverse relation with the temperature. Figure 2.11 shows the variation of H_C with the temperature for selected samples. To elucidate the reversal mechanism, data were first fitted into the model proposed by He *et al* [19, 21] for temperature dependence of coercivity $H_C(T)$ of shape anisotropy dominated soft ferromagnetic structures (dashed line in Figure 2.11) which is an extension of early work by Neel [22] and Brown [23] to study magnetic reversal process. However, a mismatch between the model and the experiment can be seen in low temperature regime (< 100 *K*). As an example, H_C values at 10 K are about 50% higher than model predicted values. In order to match with data in the low temperature regime, the original equation derived by He *et al.* was extended with a second term, which predicts an exponential decay of H_C with the temperature. So the extended equation can be given as,

$$H_C(T) = H_1(0)\frac{M_S(T)}{M_S(0)}\left[1-\left(\frac{25K_BTM_S^2(0)}{E_0M_S^2(T)}\right)^{\frac{1}{\alpha}}\right]+H_2(0).\exp\left(-\frac{T}{T'}\right) \tag{2.3}$$

Here, $H_1(0)$ and E_0 are the coercivity at 0 K and the energy barrier of reversal governed by shape, respectively as predicted by original He's model. $M_S(0)$ and $M_S(T)$ are the magnetizations at 0 K and T, respectively. The exponent α is 3/2 for curling mode and 2 for coherent rotation mode. Since the width of the nanostripe is beyond the critical size for coherent rotation given by $\sqrt{26}A^{1/2}/M_S$ which is 12 nm for Fe[27], data were fitted with $\alpha = 3/2$ to estimate $H_1(0)$, $H_2(0)$, E_0 and T' (Table 2). Here, the temperature variation of saturation magnetization has been ignored as it is negligible for the temperature range in concern. Further, we found that $H_2(0)$ has a rough linear relation to the film thickness that takes the form $H_2(0) = 410 - 8.7t$. The exponential increase in coercivity with decreasing the temperature has been observed for thin garnet films [24,25], and understood as a result of defects, which act as pinning traps at lower temperatures that hinders the reversal process by the mutual interaction with domain walls [26,27]. However, at higher temperatures this interaction potential is overcome by thermal energy, hence minimizes the defect-generated coercivity at higher temperatures. The approximate linear relation between $H_2(0)$ and t values suggest that the interfacial defects are dominated over point defects. The coercivity at 0 K, $H_C(0)$ is the addition of $H_1(0)$ and $H_2(0)$ from which the activation volume V^*, the region that the reversal process is localized (nucleation core), can be calculated using the relation $E_0 = V^*M_S(0)H_C(0)$. Table 3 shows estimated values of V^* and nucleation core size, L ($V=L^3$) for selected samples. The size of the nucleation core (15-22 nm) is much smaller than the physical size of the nanostripe, confirming that the nanostripe as a whole does not undergo coherent reversal.

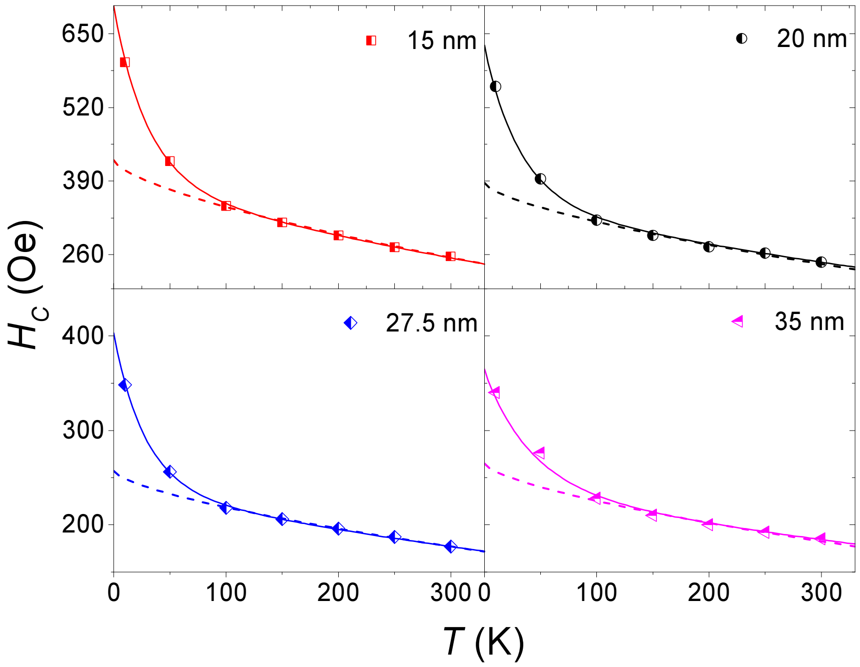

Figure 2.11 - Temperature dependence of H_C with field applied along the long axis for selected samples. The continuous line represents the fitted curve using eq. (3) for α = 3/2.

Table 2.2- Parameters of $H_1(0)$, $H_2(0)$, E_0 and T' estimated by fitting equation (3) with H_C vs. T data by taking α = 3/2 for selected samples.

Sample	***t* (nm)**	**$H_1(0)$ (Oe)**	**$H_2(0)$ (Oe)**	**E_0 (eV)**	**T' (K)**
3	15	420	280	2.6	30
4	20	380	250	3.1	32
5	27.5	253	150	3.9	28
6	35	255	110	4.4	42

Table 2.3- Zero temperature coercivity $H_C(0)$, activation volume V* and nucleation core size L, estimated from parameters in Table 1.2.

Sample	***t* (nm)**	**$H_C(0)$ (Oe)**	**V* (nm^3)**	**L (nm)**
3	15	700	3410	15
4	20	630	4518	16.5
5	27.5	403	8886	20.7
6	35	365	11069	22.3

Also, the exponential increase in H_C at lower temperatures (< 100 K) can also come from the exchange-bias effect (exchange anisotropy) as exchange-bias pinning hinders magnetic reversal. It is evident from elemental analysis by XPS (Figure 2.7) that these films contain oxides at the Fe-Ag interface that results an exchange interaction between antiferromagnetic Fe_2O_3 and elemental Fe, for temperatures below blocking temperatures of the grains. This is in agreement with previous discussions on exchange bias effect driven magnetization reversal at low temperatures [28]. Another striking feature is that easy-axis hysteresis curves (Figure 2.9) have 'shoulders' for all thicknesses at all temperatures and their width is about 250% of the H_C of the primary nanostripes (principle hysteresis). This two-step reversal can be accounted to the hard magnetic properties of narrow nanostripes formed on sidewalls, as they nucleate at higher fields due to enhanced shape anisotropy.

2.5 Micromagnetic Simulations

To visualize the reversal mechanism, T = 0 K micromagnetic simulations using OOMMF

[29] micromagnetic simulation package developed by NIST has been used. The chosen dimensions of the nanostripe were 70 nm (width), 350 nm (length), and 20 nm (thickness) with 2 nm cell size which is smaller than the exchange length of Fe (3.2 nm). Choosing 350 nm as the length is justifiable as it is reported that simulations for structures with aspect ratios greater than 5 yield the same result [18]. A 1% hard axis field was applied to break the symmetry. Figure 2.12 shows a snapshot of the reversal process of an isolated nanostripe with above dimensions, just before the magnetization turns to zero (or $H \rightarrow H_C$). As shown, nucleation core is generated at the corner of nanostripe and then propagates through the nanostripe with increasing the field. This affirm that the magnetization reversal is governed by curling mode for these nanostripes.

To understand the effect of dipolar interaction, a geometry with three-wire, five-wire and seven-wire nested systems have been simulated using NMAG [30], a finite element package developed at University of Southampton. Here, the length, the width and the thickness of nanostripes were kept at 150 nm. 30 nm and 15 nm, respectively to perform the simulation in a reasonable time. The cell size has been set to 3.0 nm and a 1% hard axis field was applied to break the symmetry as in the previous case. Figure 2.13 shows the spin configuration of each geometry just before the magnetization becomes zero. It can clearly be seen that the nucleation begins at an end nanostripe and propagates to the neighboring nanostripe and sweeps throughout the entire film, regardless the number of nanostripes.

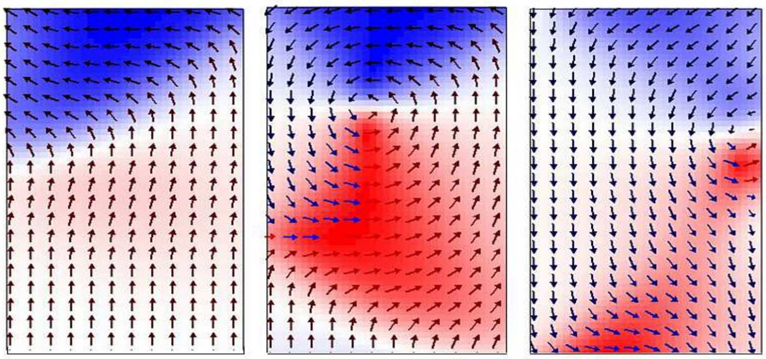

Figure 2.12 - Snapshots of three stages of magnetization reversal of a 350 nm x 70 nm x 20 nm nanostripe simulated at 0 K using OOMMF. The reversal begins at one end of the nanostripe and sweeps across the volume.

This coordinated reversal process instead of individual reversal of each nanostripe, signifies the strong dipolar attraction between nanostripes in this arrangement. However, this contradicts a previous report which describes that for a linear system (all nanostripes are on the same plane), the central nanostripe switches first due to maximum intensity of dipolar fields created by surrounding nanostripes [31], suggesting that the reversal process strongly correlated to nanostripe arrangement.

2.6 Conclusions and Future work

Fe nanostripe based thin films exhibiting larger uniaxial anisotropies were fabricated by UV-assisted nanoimprint lithography. PET film was chosen as the substrate due to its good mechanical properties, low cost, and demonstrated high volume direct patterning capabilities in roll-to-roll nanoimprinting [17].

The in-plane H_C along nanostripes, induced by shape, changes with the film thickness giving the maximum value of 257 Oe for 15 nm thick nanostripes at room temperature. This variation has been attributed to size effects for thin films and growing dipolar interactions for thick films, which reduces in-plane H_C.

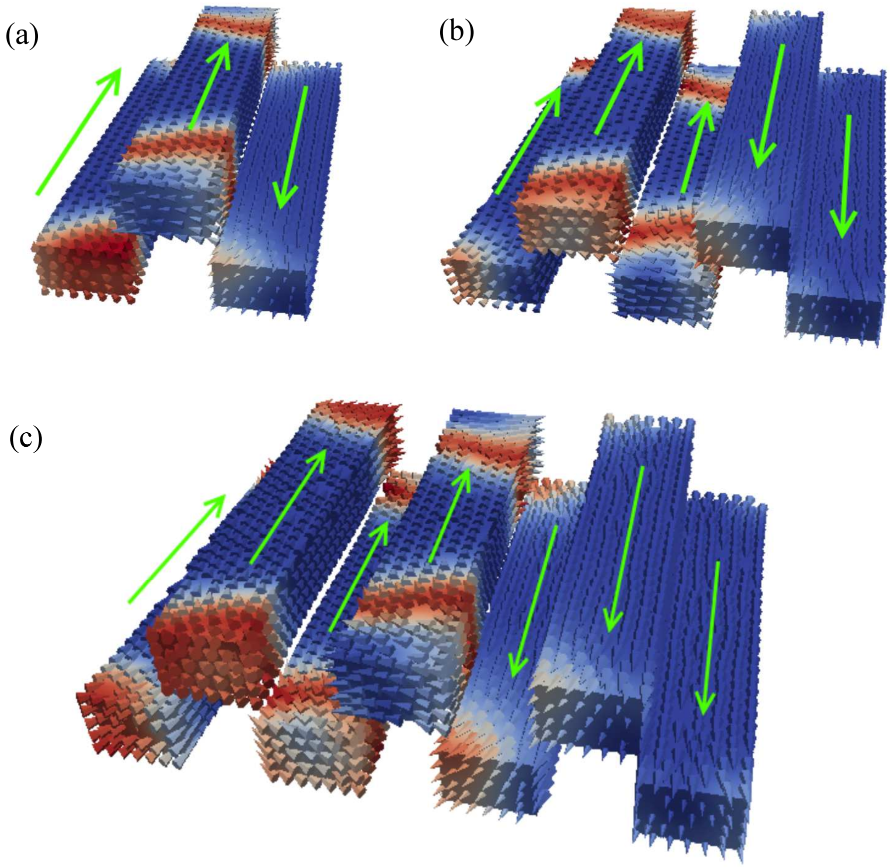

Figure 2.13 - Snapshots of nanostripes with three, five, and seven wires at M→0. The reversal begins from rightmost nanostripe and propagates thought the film.

By combining magnetic measurements at different temperatures with extended He *et al* [21] model, the magnetization reversal process found to be dominated by curling and the size of the nucleation core is much smaller than the physical volume of the nanostripe.

Furthermore, macromagnetic simulations illustrate that the nucleation core is formed at one corner of the nanostripe and propagates through the entire volume of the nanostripe. Also simulations performed on multi-stripe assemblies show that dipolar interactions between nanostripes couple the reversal resulting in a coordinated reversal from one end of the thin film to the other end, hence avoiding individual reversal of each nanostripe. The exponential increase in H_C with reducing the temperature is ascribed to defect-generated pinning traps at low temperatures. I propose that the 'shoulders' observed in easy axis hysteresis loops are due to narrow nanostripes formed on sidewalls. One noteworthy advantage of nanostripe based thin films fabricated in this work is that they are highly anisotropic but maintain the same magnetic moment per unit area as of flat thin films, which can be further enhanced by reducing the width of nanostripes. As an extension of this project, it is interesting to study how hard magnetic and exchange-spring magnetic thin films would perform when they are transformed from planar to nanostripe geometry. Combining the magnetocrystalline anisotropy and the shape anisotropy would result perfect orientation of magnetic moments in the entire body which can substantially increase the remanence magnetization, and hence the maximum energy product of the magnet as discussed in Chapter 1.

To conclude, this straightforward fabrication method can be implemented for high volume fabrication of a range of future ferromagnetic nanoscale thin film based devices, where low cost and high performance will dominate future needs.

2.7 Reference

[1] Tretiakov, O. A., Clarke, D., Chern, G. W., Bazaliy, Y. B., Tchernyshyov, O., *Physics Review Letters* 100, 127204 (2008).

[2] Lee, J. Y., Lee, K. S., Kim, S. K., *Applied Physics Letters,* 91, 122513 (2007)

[3] Lee, J. Y., Lee, K. S., Choi, S., Guslienko, K. Y., Kim, S. K., *Physics Review B* 76, 184408 (2007)

[4] Hayashi, M., Thomas, L., Moriya, R., Rettner, C., Parkin, S. S., *Science* 320, 209-211 (2008).

[5] Hayashi, M., Thomas, L., Rettner, C., Moriya, R., S. P. Parkin, S., *Nature Physics*, 3, 21-25 (2006).

[6] Grollier, J., Boulenc, P., Cros, V., Hamzić, A., Vaurès, A., Fert, A., Faini, G., *Applied Physics Letters*, 83, 509 (2003).

[7] Allwood, D., Xiong, G., C. Faulkner, C. , Atkinson, D., Petit, D., P. Cowburn, R., *Science* 309, 1688 (2005).

[8] Huang, H. T., Ger, T. R., Lin, Y. H., Wei, Z. H., *Lab Chip*, 3098-3104 (2013).

[9] Bang, W., Kim, K., Rathnayaka, K. D. D., Teizer, W., Lyuksyutov, I. F., Naugle, D. G., *Physica C Superconductivity* 493, 89-92 (2013).

[10] Borca, B., Fruchart, O., Meyer, C., *Journal of Applied Physics,* 99, 08Q514 (2006).

[11] Cheng, R., Guslienko, K., Fradin, F., Pearson, J., Ding, H., Li, D., Bader, S., *Physics Review B* 72, 014409 (2005).

[12] Borca, B., Fruchart, O., David, P., Rousseau, A., Meyer, C., *Applied Physics Letters*, *90*(14), 142507 (2007).

[13] Tripathi, J. K., Markovich, G., Goldfarb, I., *Applied Physics Letters*, *102*(25),

251604(2013).

[14] Arora, S. K., B. J. O’Dowd, B. Ballesteros, P. Gambardella, I. V. Shvets, *Nanotechnology* 23, 23 (2012).

[15] K Arora, S., J O'Dowd, B., Thakur, P., B Brookes, N., Ballesteros, B., Gambardella, P., V Shvets, I., *Current Nanoscience*, *9*(5), 609-614 (2013).

[16] Li, S. P., Natali, M., Lebib, A., Pepin, A., Chen, Y., Xu, Y. B., *Journal of Magnetism and Magnetic Materials* 241, 447-452 (2002).

[17] John, J., Tang, Y., Rothstein, J. P., Watkins, J. J., Carter, K. R., *Nanotechnology* 24.50, 505307 (2013).

[18] Uhlig, W. C., Shi, *Applied Physics Letters*. 84, 5 (2004).

[19] Zheng H, Skomski R, Menon L, Liu Y, Bandyopadhyay S, Sellmyer D, *Physical Review B* 65 (2002).

[20] Vázquez, M., K. Pirota, M. Hernandez-Velez, V. M. Prida, D. Navas, R. Sanz, F. Batallan, and J. Velazquez, *Journal of Applied Physics* 95, 11 (2004).

[21] He, L., Chen, C., *Physical Review B* 75, 184424 (2007).

[22] Néel, L., *Annals of Geophysics* 5, 99 (1949).

[23] Brown, W. F., *Physical Review* 130, 1677 (1963).

[24] Prados, C., Hattink, B. J., Pina, E., Batlle Gelabert, X., Labarta, A., González-Miranda, J. M., Hernando, A., *IEEE Transactions on Magnetics,* 36, 6 (2000).

[25] Vertesy, G., Tomas, I., *Journal of Applied Physics*, *77*(12), 6426-6431 (1995).

[26] Vértesy, G., Tomáš, I., Půst, L., Pačes, J., *Journal of Applied Physics*, 71(7), 3462-3466 (1992).

[27] Gaunt, P., *Philosophical Magazine B*, 48(3), 261-276 (1983).

[28] Pardavi-Horvath, M., *IEEE Transactions on Magnetics*, 21(5), 1694-1699 (1985).

[29] Donahue, M. J., Porter, D. G., OOMMF User's guide, NIST (1999).

[30] Fischbacher, T., Franchin, M., Bordignon, G., Fangohr, H., *IEEE Transactions on Magnetics*, *43*(6), 2896-2898 (2007).

[31] Zighem, F., Maurer, T., Ott, F., Chaboussant, G., *Journal of Applied Physics*, *109*(1), 013910 (2011)

CHAPTER 3

SUBSTRATE DEPENDENT MAGNETIZATION REVERSAL OF $SmCo_5$ AND $SmCo_5/Co$ EXCHANGE-SPRING THIN FILMS

This chapter discusses how magnetization reversal of hard and exchange-spring magnetic thin films is affected by the substrate properties such as crystallinity, roughness and wetting conditions using single crystal MgO(100) and glass substrates. The chapter begins with prior work and related concepts (theory of hard and exchange-spring magnetic materials were introduced in the first chapter) followed by fabrication, surface and structural characterization and magnetic property measurements. This study shows that magnetic properties greatly depend on the substrate properties, which is vital for thin film based applications.

3.1 Introduction

Exchange-coupled magnetic materials (spring-exchange materials) that are composites of soft and hard magnetic materials have important properties such as enhance remanence, high energy products $(BH)_{max}$, high T_C and lower cost, making them ideal candidates as next generation permanent magnets. So understanding non-trivial magnetic nucleation and pinning dynamics of both hard and exchange-coupled materials is vital in tailoring them more efficiently.

Although dynamics of soft ferromagnetic materials have been widely studied and well understood, a little progress has been made in the quest of understanding dynamics of hard magnetic or exchange coupled magnetic materials. This is due to the fact that dynamic properties strongly correlated to crystal structure, epitaxy, substrate effects and processing conditions as they determine the grain size and microstructure of these materials. As an example, the reversal of $SmCo_5$ in bulk is governed by nucleation but Sm_2Co_7 is dominated by domain wall pinning when thermally processed [1]. However, when it comes to thin films, pinning is expected to dominate due to interface properties. Further, no clear agreement can be found in literature on how physical parameters such as thickness, texture and roughness change microstructure and magnetic properties [2, 3], as it is often difficult to isolate the effect of each parameter as they are strongly coupled to epitaxy and processing conditions [4]. $SmCo_5$ thin films grown on MgO(100) and MgO(110) single crystal substrates with Cr buffer layer show strong in-plane hard magnetic properties, however the microstructure of $SmCo_5$ grown on MgO(100) is bi-crystalline (twisted c-axis) with Sm-Co$(11\bar{2}0)$ phase while $SmCo_5$ grown on MgO(110) results Sm-Co$(1\bar{1}00)$ phase, which is uniaxial [2,5]. This difference of microstructure is clearly reflected in their magnetic properties, as the coercivity of Sm-Co$(11\bar{2}0)$ show no dependence with the film thickness, while the coercivity of Sm-Co$(1\bar{1}00)$ decreases with increasing film thickness (Figure 3.1).

High H_C of these films at thin film limit has been attributed to initial island growth. When the film thickness is increased these islands coalesce to create large grains that reduces H_C. Also the underlayer also plays a major role in controlling the grain growth.

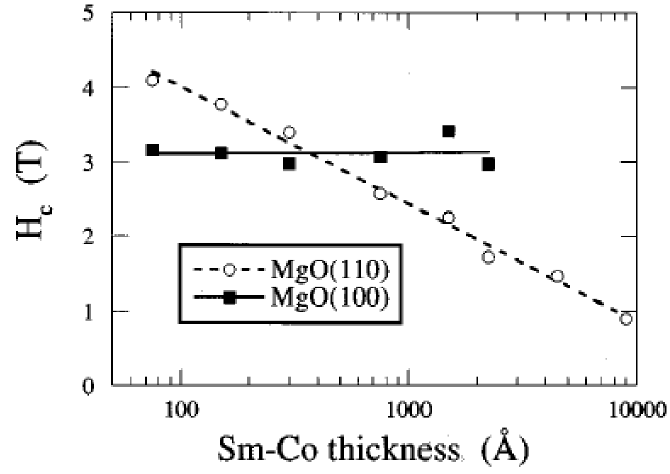

Figure 3.1 - Variation of coercivity with film thickness for Sm-Co(11$\bar{2}$0) and Sm-Co(1$\bar{1}$00) grown on MgO(100) and MgO(110), respectively (adopted from ref[2]).

As an example Sm-Co films deposited on thin Cr buffer layers have smaller grain structure [6], which has made such a texture an excellent candidate for high density recording media. When a magnetic thin film consists of large number of grains or if the magnet has an amorphous nature, the effective anisotropy is given by the random anisotropy model which is an analysis of the interplay between exchange and anisotropy energies in a randomly oriented grain structure. If grains are ferromagnetically coupled, the effective anisotropy is given by (for $D<<l_{ex}$) [7],

$$\langle K \rangle = \frac{K_1^4 D^6}{A^3} \tag{3.1}$$

Where D, K_1, l_{ex} and A are average grain size, magnetocrystalline anisotropy, exchange length and exchange stiffness, respectively. However, when grains are isolated and only coupled via dipolar fields, $<K>$ strongly depends on the grain size as well as the grain shape.

In addition to pinning induced by structural defects, these alloyed hard magnetic materials have high degree of chemical inhomogeneity [2-5]. These chemical inhomogenieties found in single grains in the form of stacking faults are considered to be inducing pinning effects. As an example both Sm_2Co_7 and $SmCo_5$ phases co-exist in Sm-Co magnets so the local reversal of each grain can be entirely different and is highly correlated to this composition variation that creates different number of pinning centers in each grain. Scanning or tunneling electron microscopy studies can reveal this local inhomogeneity in thin film magnetic samples.

Reversal of spring-exchange magnetic materials is closely resemble that of hard magnets as the reversal of a spring-exchange magnet is dictated by the reversal of hard phase, so domain wall pinning is considered to be the prime mechanism [1,5,8,9]. However, the structure defined non-collinearity at the interface also come into play in addition to structural and chemical inhomogenieties of hard phase that creates pinning centers.

This study was performed to further explore the reversal mechanism of exchange spring thin films grown on two different substrates. $SmCo_5$/Co was selected as the exchange-coupled bi-layer thin film and it was grown on MgO(100) and glass substrates at varies temperatures with varying layer thickness of $SmCo_5$ and Co. Room temperature magnetic measurements confirm spring-exchange behavior with large energy products while temperature dependent magnetic measurements show an increase in H_C for all films due to lower spin fluctuation and pinning ability by defects at low thermal energies. However, in addition to rise in H_C, films grown on glass show a transformation from one step to two step reversal when reducing the measuring temperature, suggesting a weakening of exchange interaction. Structure of each film was analyzed by x-ray diffraction and atomic force microscopy to explore the crystalline nature, substrate roughness and grain formation on each substrate.

3.2 Sample Preparation

$SmCo_5$ hard magnetic and $SmCo_5$/Co exchange spring bi-layer films were fabricated by DC and RF magnetron sputtering (AJA Orient 8 sputter coater) at high vacuum of 10^{-8} Torr on MgO(100) and glass with a 60 nm and a 30 nm Cr seed and capping layers, respectively. An alloy target with nominal composition was used to deposit $SmCo_5$, and both the seed layer and $SmCo_5$ were deposited at 500° C, which is adequate enough to induce in-plane hard magnetic properties of $SmCo_5$ layer [10, 11]. After the growth of Cr and $SmCo_5$ layers, samples were allowed to cool for 6 hours before depositing Co and Cr capping layer, to minimize the inter-diffusion at the $SmCo_5$/Co interface that changes the composition of the hard phase. The thickness of $SmCo_5$ and Co layers were varied between 15 nm-50 nm and 5 nm-25 nm, respectively to find the optimal thickness of each layer that delivers a single step reversal with highest H_C. Prior to film growth, all substrates were cleaned with toluene, acetone followed by oxygen plasma cleaning for 2 mins at 150 W with a gas flow of 50 cc/min. The base pressure of the sputter chamber was maintained below $1\text{x}10^{-7}$ Torr to reduce oxidation, and more importantly all targets were etched for 2 mins at 6 cc/min Ar flow rate to remove the top oxide layer. Further, substrates were pre-heated for 10 mins at growth temperature, and were ramped up in steps from room temperature to deposition temperature to avoid substrate deformation and cracks. All layers were sputtered at 4 mTorr Ar pressure and sputtering powers were fixed and kelp low (75 W DC for $SmCo_5$, Cr and 100 W RF for Co) to promote continues film growth. In order to exclude artifacts arising from the capping Cr layer and also to analyze the surface properties of Cr seed layer, 60 nm Cr seed layers were grown on both substrates under identical conditions.

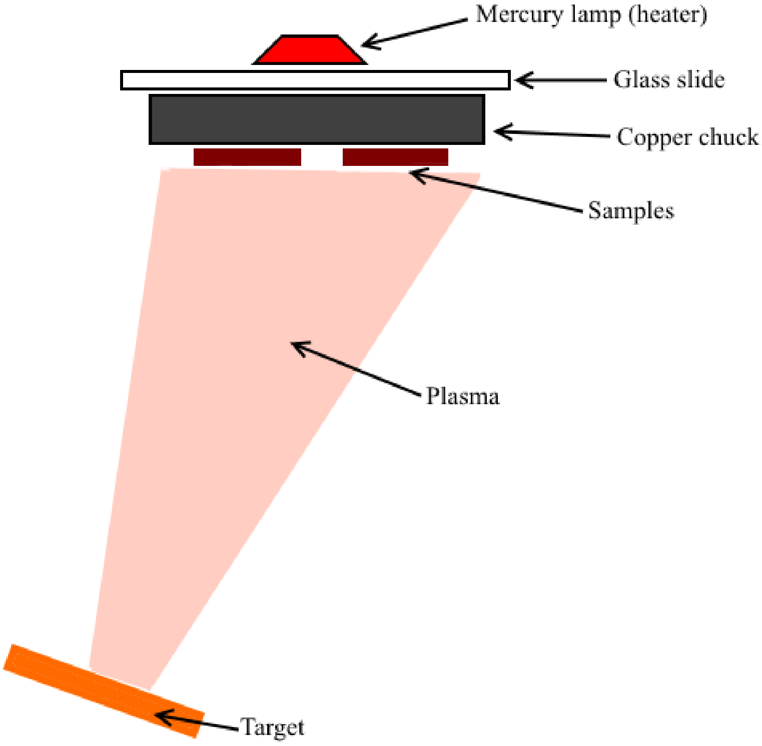

Figure 3.2 - Schematic of sputter deposition at high temperature and high vacuum. Samples were ramped to high temperature in steps to avoid any substrate deformations.

3.3 Structure and Surface Analysis

Structural properties of the samples have been studied by x-ray diffraction using Panalytical X'Pert MRD spectrometer with Cu K_α radiation and phase analysis was performed by X'Pert Highscore Plus and MAUD software. Figure 3.3 shows the $\theta-2\theta$ XRD pattern of $SmCo_5$ (30 nm)/Co (7.5 nm) grown on MgO(100) substrate with a Cr seed layer at 500° C. As shown, MgO(100) single crystal results epitaxial growth of Cr(200) which guides the growth of highly textured $SmCo_5(11\bar{2}0)$ phase [3]. Small Full width of half maximum (FWHM) values of Cr(200) and $SmCo_5(11\bar{2}0)$ which are 0.17° and 0.72°, respectively show high degree of texture of this epitaxial assembly. The x-ray diffraction pattern of Cr (60 nm)/MgO(100) grown under identical conditions confirms the Cr(200) phase, excluding any artifacts coming from the capping Cr layer (Figure3.4).

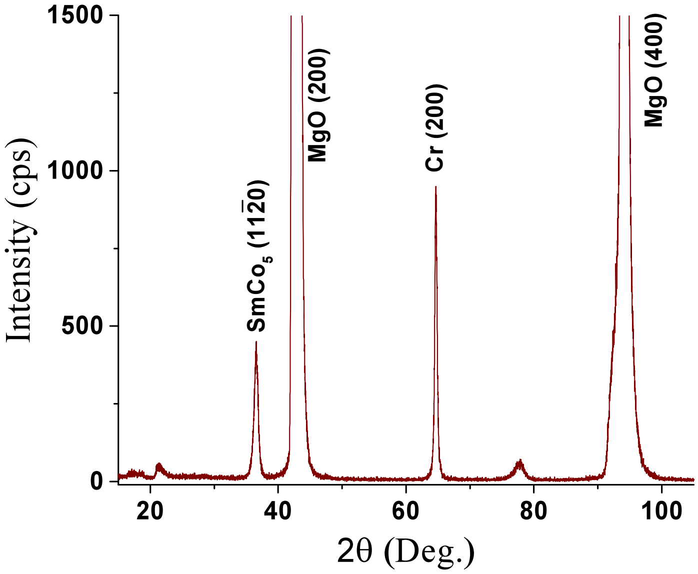

Figure 3.3 - X-ray diffraction pattern of Cr (60 nm)/$SmCo_5$ (30 nm)/Co (7.5 nm)/Cr (30 nm) grown on MgO(100) at 500° C.

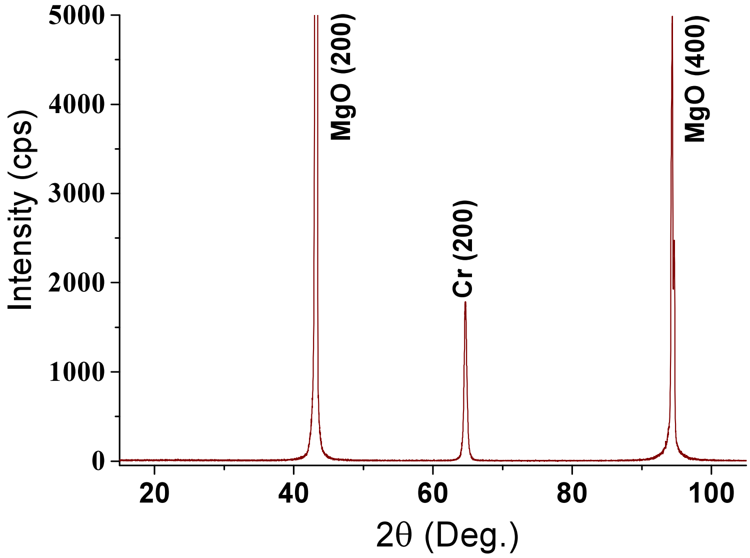

Figure 3.4 - X-ray diffraction pattern of Cr (60 nm) grown on MgO(100) at 500º C.

As shown, Cr layer has only the Cr(200), which suggests a good epitaxial growth on MgO(100) and Figure 3.5 illustrates the epitaxial relation between MgO, Cr and $SmCo_5$ films.

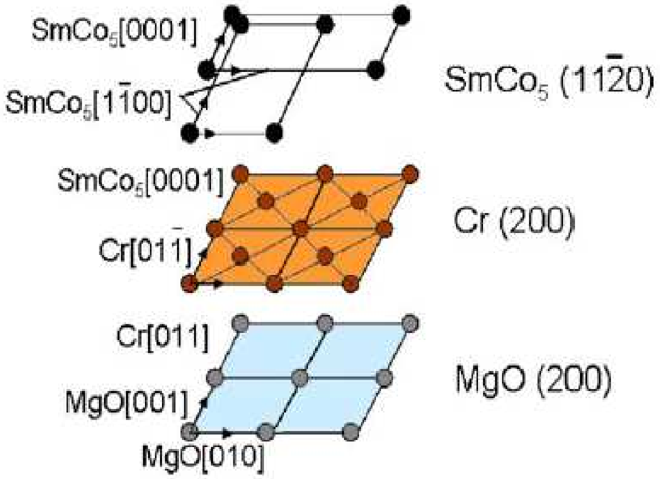

Figure 3.5 - The illustration of epitaxial relationship between $SmCo_5(11\bar{2}0)$ || Cr(200) || MgO(200) (adopted from ref [3]).

However, $SmCo_5$/Co spring magnets made on glass substrates show low crystalline nature evident by its XRD peak intensities, suggesting that $SmCo_5$ grains are randomly distributed resulting a random distribution of easy-axis. Here, in contrast to samples grown on MgO(100), both Cr(110) and Cr(200) phases exist in almost equal intensities, however, $SmCo_5$ exhibits only the twined epitaxy with $(11\bar{2}0)$ orientation (Figure 3.6 & Figure 3.7). In addition, the XRD pattern of Cr(60)/$SmCo_5$(50 nm) on glass (Figure 3.8) deposited at room temperature shows only the Cr(110) phase. This suggests that Cr(200) orientation is possible only at higher temperatures and $SmCo_5$ $(11\bar{2}0)$ phase is essentially driven by the Cr(200) phase, re-affirming the proper crystal match between the buffer layer and the hard magnetic layer plays a critical role in orienting the c-axis in-plane. In addition, broader XRD peaks observed for samples on glass can be attributed to wide size distribution of grains.

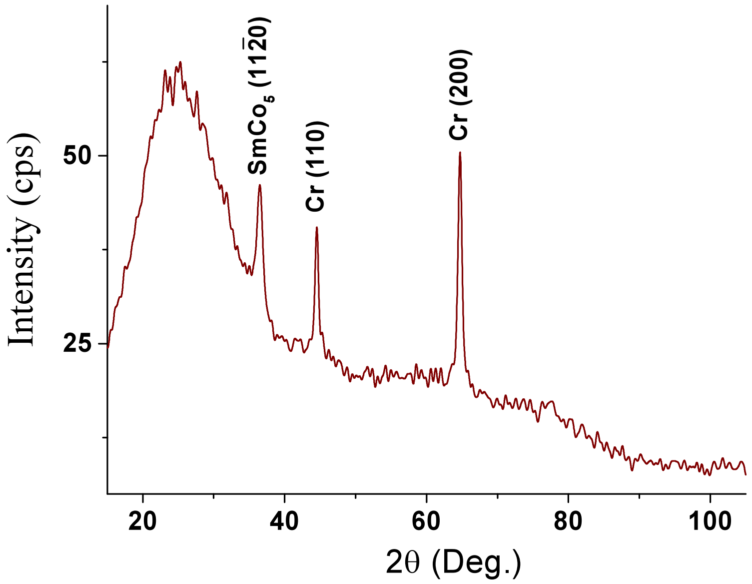

Figure 3.6 - X-ray diffraction pattern of Cr (60 nm)/$SmCo_5$ (30 nm)/Co (7.5 nm)/Cr (30 nm) grown on glass at 500° C.

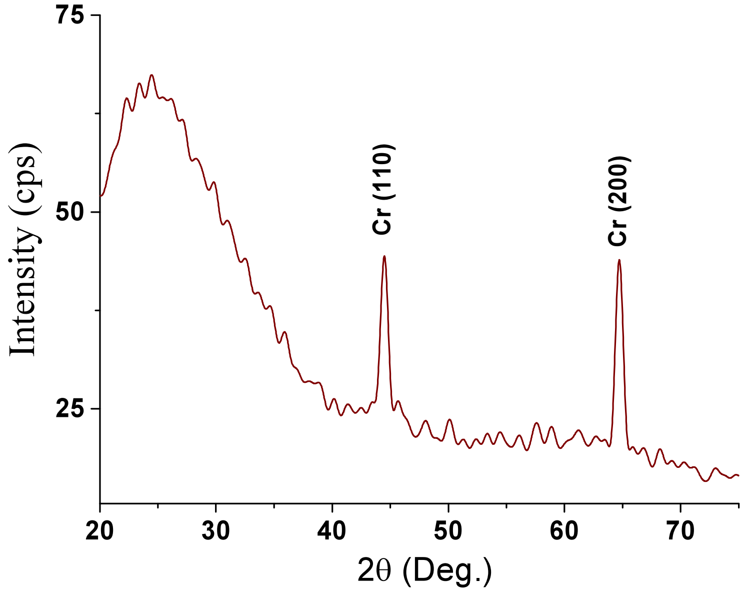

Figure 3.7 - X-ray diffraction pattern of Cr (60 nm) on glass at 500° C

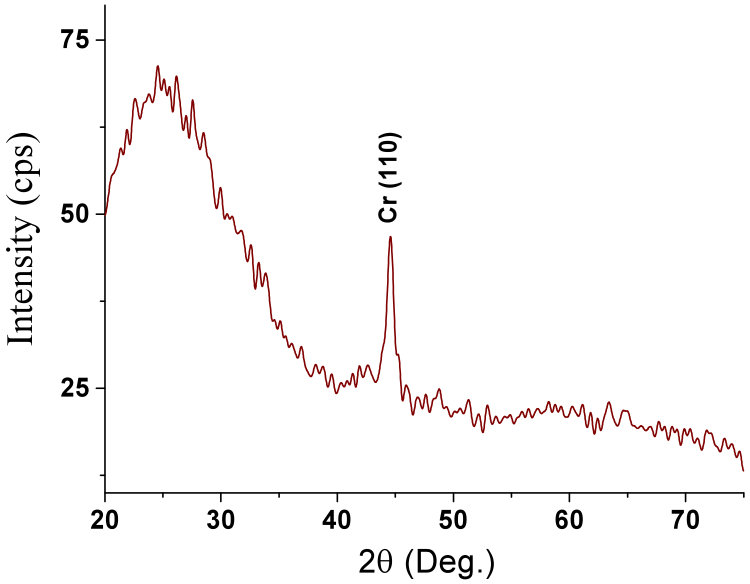

Figure 3.8 - X-ray diffraction pattern of Cr (60 nm)/$SmCo_5$ (50 nm)/Cr (30 nm) grown on Glass at room temperature.

In order to understand the effect of pinning, which is expected to be the dominant reversal mechanism of hard magnetic thin films, Atomic force microscopy (AFM) was used to study the surface properties of substrate and Cr grain formation of seed layer. Image data were analyzed by NanoScope Analysis v1.4 (Bruker, Inc.) software.

Figure 3.9 shows AFM figures of MgO(100) and glass substrates. While both substrates are relatively smooth, MgO(100) has peak-to-peak roughness about 5 nm in contrast to glass, which is approximately 2 nm. AFM figures of the Cr seed layer deposited at 500^{o} C on MgO(100) and glass show different surface properties (Figure 3.10). The average grain size of Cr on MgO(100) is approximately 38±17 nm. Also, grains are squarer and have narrow size distribution showing good epitaxial growth. In addition, the peak-to-peak roughness of this film is about 4 nm, suggesting that the Cr underlayer is essentially continuous as a result of good epitaxial growth.

However, large and isolated grain (~170±82 nm) formation can be seen in Cr layer deposited on glass at 500^{o} C. This island-like grain formation is most likely due to the low adhesion between glass and Cr at high temperature. In addition to the grain size, Cr islands on glass shows pillar like growth with heights about 40 nm in comparison to 4 nm peak-to-peak roughness for Cr layer on MgO(100). This suggests that magnetization reversal of the sample on glass is largely driven by island-like growth of $SmCo_5$ in addition to interfacial defects, as this island formation results isolated $SmCo_5$ grains which essentially behave as single domain particles due to large anisotropy constant of

$SmCo_5$.

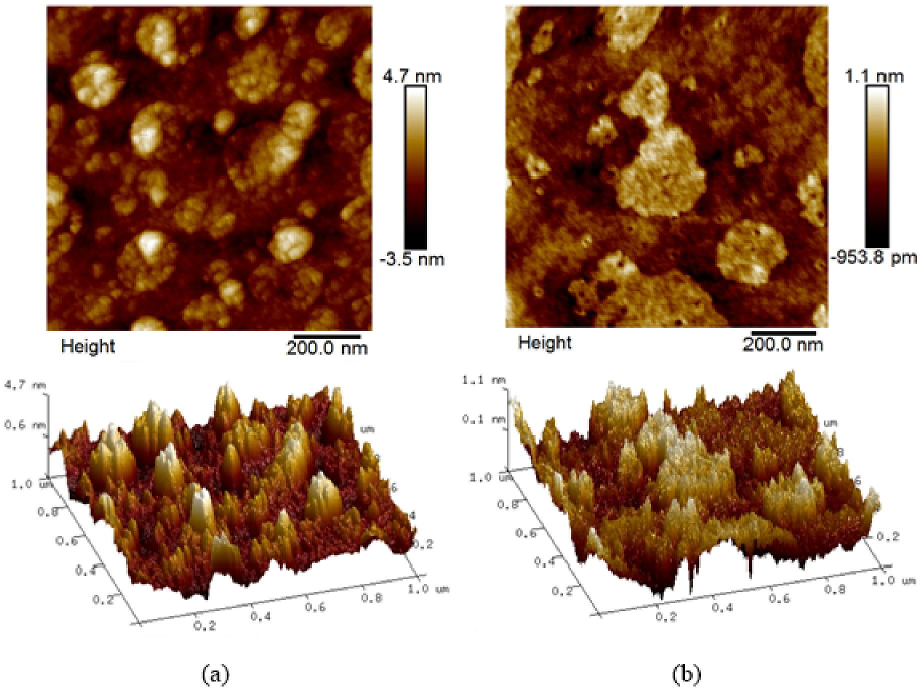

Figure 3.9 - AFM figures of the surface of a) MgO) substrate b) glass substrate

3.4 Magnetic Measurements

Magnetic properties were measured using a Superconducting Quantum Interference Device (SQUID) magnetometer (MPMS, Quantum Design, Inc) with 7 T maximum applied field. Based on measurements of samples grown on MgO(100) substrates, ideal thickness of $SmCo_5$ and Co are 30 nm and 7.5 nm, respectively for 500° C growth temperature. Figure 3.13 shows the hysteresis curves of Cr/$SmCo_5$ on MgO (Sample A) and glass (Sample B) grown at 500° C. Coercivities of Sample A and Sample B are 17.2

KOe and 18.5 KOe, respectively.

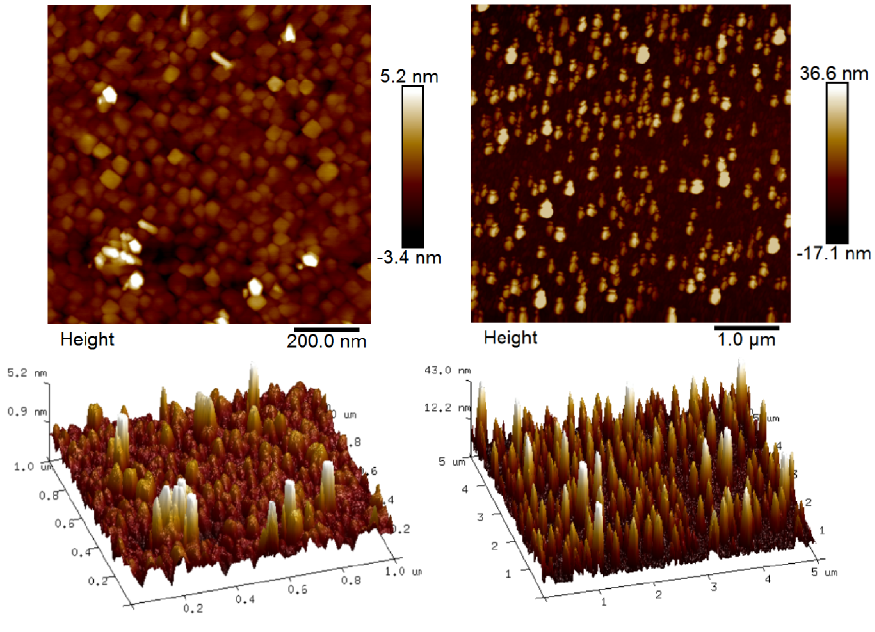

(a)

(b)

Figure 3.10 - AFM figures of the surface of Cr deposited a) MgO(100) substrate b) Glass substrate at 500° C.

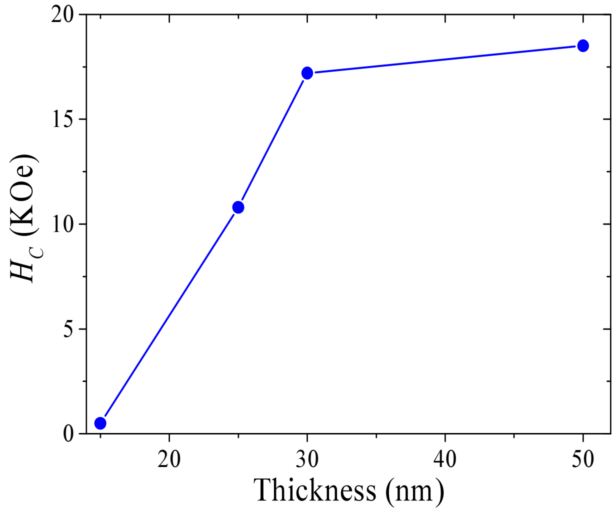

Figure 3.11 - Dependence of coercivity with $SmCo_5$ layer thickness, grown on Cr (60 nm)/MgO(100) layer at 500° C.

Higher coercivity in Sample B is induced by high degree of pinning arise due to high interface roughness and isolated-like $SmCo_5$ grain growth, which indeed increase H_C, as discussed in the previous section.

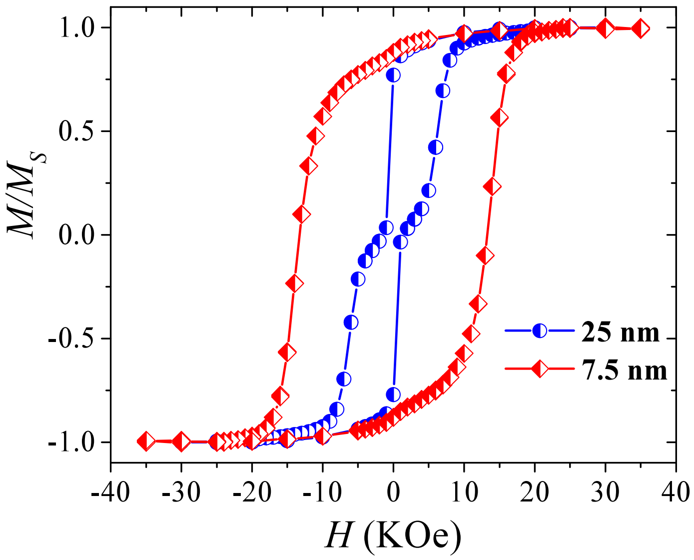

Figure 3.12 - Normalized room temperature hysteresis curves for exchange-spring bi-layers with over-sized (25 nm) and critical (7.5 nm) Co layer on 30 nm $SmCo_5$ layer.

However, the maximum energy product of Sample B is just 5.5 MGOe in contrast to 12.8 MGOe of Sample A. This significant reduction in the energy product of the sample on glass is due to random orientation of magnetic moments due to the absence of epitaxial guidance or structural orientation by the amorphous glass substrate. When grains are randomly oriented in 3D space, the effective remanence Mr is given by,

$$Mr = \int_0^{\pi/2} M_S.\cos\theta.\sin\theta.d\theta = 0.5M_S \tag{3.2}$$

Since the maximum energy product $(BH)_{\max} \propto M^2$, random grain orientation results lower energy products even though the sample has a high H_C.

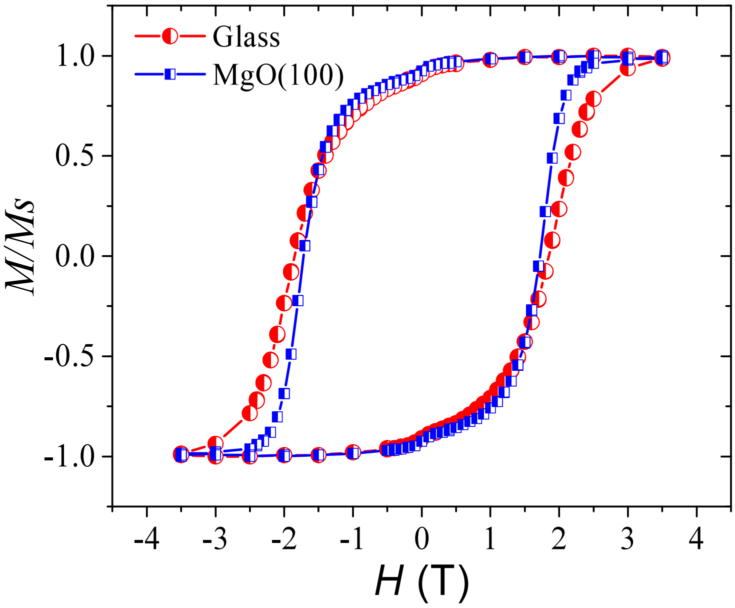

Figure 3.13 - Normalized room temperature hysteresis curves of Cr/SmCo$_5$ on MgO(100) and glass substrates grown at 500º C.

Figure 3.14 shows room temperature hysteresis curves of exchange-spring magnet thin films with SmCo$_5$ (30 nm)/Co (7.5 nm) composition. As expected, for samples grown on both MgO (Sample C) and glass (Sample D), the H_C drops and the M_S rises due to the inclusion of soft phase, compared to hard magnetic thin film samples (Sample A & B). However, in contrast to Sample A&B, here the bi-layer on MgO(100) shows a higher resistance to reversal with a H_C of 13.2 KOe, while the bi-layer on glass has a slightly lower coercivity (H_C=12.5 KOe). Maximum energy products $(BH)_{max}$ are 14.5 MGOe and 5.3 MGOe for Sample C & D, respectively. Although a clear enhancement in $(BH)_{max}$ can be seen between hard and exchange-spring samples grown on MgO(100), no enhancement is seen between hard and exchange-spring samples grown on glass. This shows that the remanence enhancement by the soft phase is compensated by the random orientation of grains. Table 3.1 shows estimated H_C, M_S and $(BH)_{max}$ values of Sample A-D.

Table 3.1 - Estimated values H_C, M_S and $(BH)_{max}$ of hard magnetic and exchange-spring thin films grown on MgO(100) and glass substrates.

Sample	**H_C (KOe)**	**M_S (emu/cc)**	**BH_{max} (MGOe)**
A	17.2	663	12.8
B	18.5	424	5.5
C	13.3	754	14.5
D	12.5	465	5.3

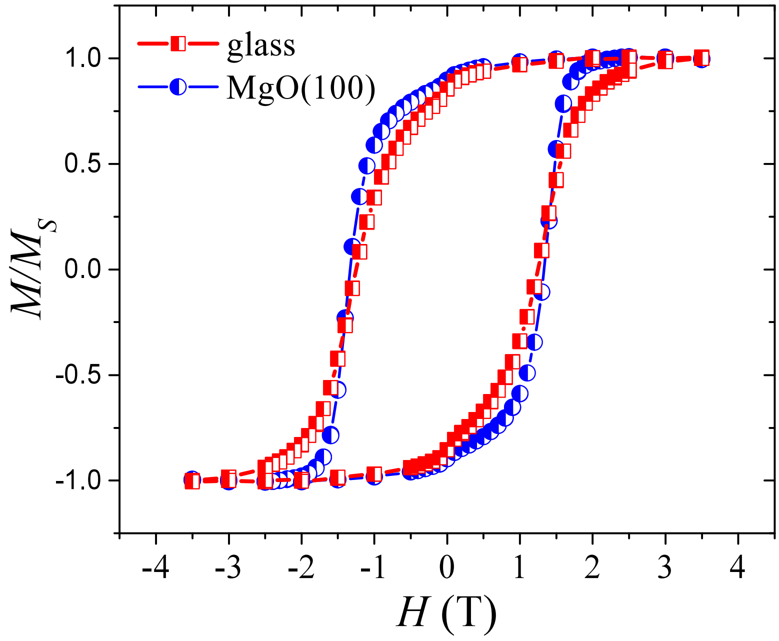

Figure 3.14 - Normalized room temperature hysteresis curves of exchange-spring bilayers on MgO(100) and Glass substrates grown at 500° C.

The temperature dependent magnetic properties of exchange-spring bi-layer samples on both MgO(100) and glass were measured from 300 - 100 K. Figure 3.15 shows hysteresis curves at each temperature of the sample on MgO(100). The H_C increases linearly (Figure 3.16) from 13.2 KOe at 300 K to 22 KOe at 100 K while preserving the original single step reversal behavior. This single step behavior can be ascribed to strong exchange coupling between soft-hard phases and the increase in H_C is due to increase in effective magnetocrystalline anisotropy and pinning as a result of low thermal fluctuations at lower temperatures. In addition, with lowering the temperature, a slight decrease in the squareness of the hysteresis loop can be noticed. A similar observation has been reported by Zhang *et al* [13] for Sm-(Co, Cu)/Fe exchange-spring multilayers grown on SiO_2. However, they observed that the H_C increases exponentially with reducing the measuring temperature (18.2 KOe at 10 K versus 3.7 KOe at 400 K) while preserving the single step reversal.

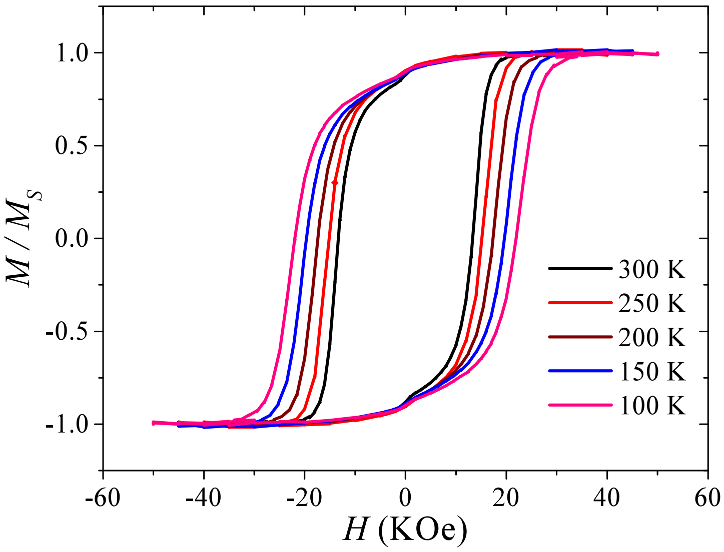

Figure 3.15 - Normalized hysteresis curves measured at varies temperatures of exchange-spring bi-layer sample on MgO(100)*.

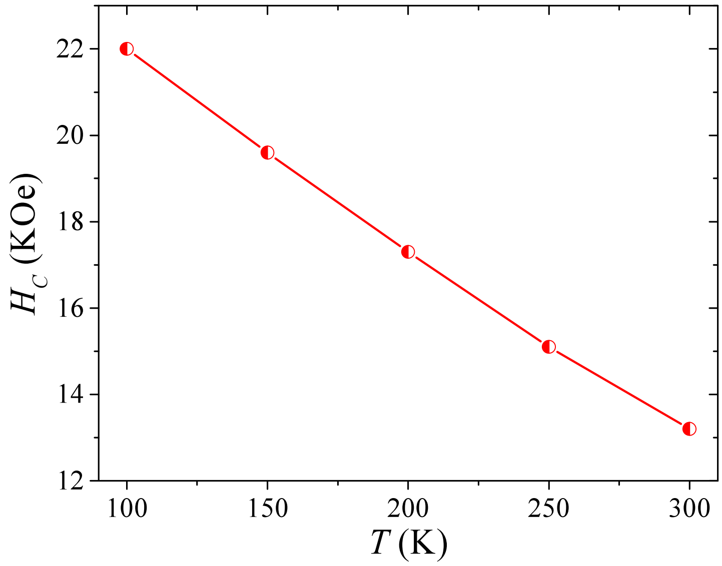

Figure 3.16 - Variation of coercivity with measurement temperature of exchange-spring bi-layer sample on MgO(100).

Figure 3.17 shows the development of the hysteresis for the sample on glass upon reducing the measuring temperature. Although the H_C rises with decreasing the temperature as observed for the sample on MgO, 'shoulder' formation can be seen in reversal curves measured at 150 K and 100 K. This conversion from single step to two step reversal suggests an exchange decoupling is taking place below a critical temperature. Previous studies that has observed this phenomena for magnetic nanocomposites account this to decoupling of soft-hard phases at lower temperatures [14, 15]. In general, for an effective exchange coupling between soft-hard phases, the soft phase size is required to be in the range of domain wall width of the hard phase δ_B, as explained in Chapter 1. However, δ_B is sensitive to the effective anisotropy K, as $\delta_B \propto 1/\sqrt{K}$, which increases with decreasing the temperature. So the δ_B drops when decreasing the temperature, mandating a smaller soft region to keep the exchange coupling intact at lower temperatures. Since the physical size of the soft region remains unchanged, this results partially or fully decoupled magnetic state, making the reversal a two step process which is the superposition of individual reversals of uncoupled regions. However, the sample on MgO(100) does not show such development at lower temperatures, suggesting that this decoupling phenomena is strongly correlated to microstructure. AFM measurements of the Cr seed layer suggests that the sample grown on glass have large $SmCo_5$ grains in contrast to the sample on MgO(100). In nanocomposite samples, the soft phase size is determined by the soft phase grain size, so this decoupling phenomena is straightforward for composites with larger soft grains (or composites with high soft phase volume) [14, 15]. However, in thin films the critical dimension is still the thickness that is same for both Sample C and D, so the presence of decoupling in Sample D but not in Sample C at low temperatures does not fall into the above trivial explanation.

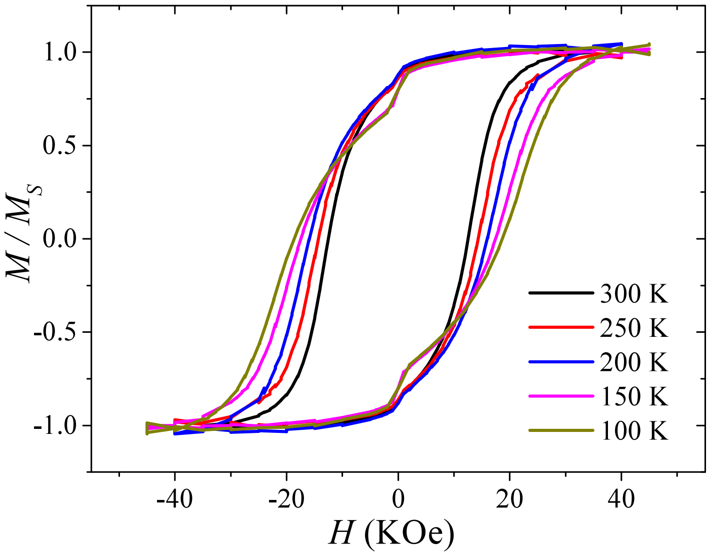

Figure 3.17 - Normalized hysteresis curves measured at varies temperatures of exchange-spring bi-layer sample on glass*.

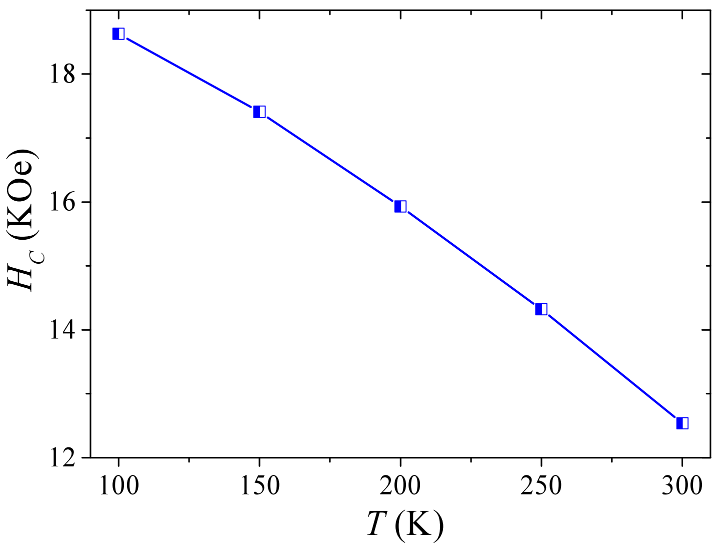

Figure 3.18 - Variation of coercivity with measurement temperature of exchange-spring bi-layer sample on glass.

So this peculiar decoupling behavior of the exchange-coupled sample grown on glass should be accounted to microstructure as any difference should arise from the microstructure as material volumes of both samples are identical.

3.5 Conclusions and future work

In this work, I investigated magnetization reversal process of hard and exchange-coupled magnetic thin films grown on single crystal MgO(100) and amorphous glass substrates with a 60 nm Cr seed layer. Growth temperature was set at 500°C and optimum $SmCo_5$ thickness based on coercivity estimations was found to be 30 nm to align moments in-plane to the substrate. For exchange-coupled samples, the soft layer thickness was set at 7.5 nm for single step reversal. X-ray diffraction studies on samples grown on both substrates show that in-plane hard magnetic properties are due to the formation of twisted-crystalline phase, $SmCo_5$ $(11\bar{2}0)$ guided by the Cr (200) seed layer. Although the epitaxial match between Cr(200) and MgO(200) can be considered the underlying cause for Cr(200) phase on MgO(100) substrate, x-ray diffraction patterns of Cr(60 nm) grown on glass at room temperature and high temperature (500^{o} C) affirm that high temperature growth conditions are required to get Cr(200) phase. AFM measurements show that both glass and MgO(100) substrates have an average roughness below 5 nm, however, different growth properties of Cr seed layer on MgO(100) and glass can be seen. AFM figures show Cr on MgO(100) forms square shape grains of 38±17 nm and Cr on glass results steep and large island-like grains of 170±82 nm. High coercivity is dominated by the island-like grain growth and pinning by interface roughness, evident by larger coercivity of 18.5 KOe for $SmCo_5$ on glass in contrast to 17.2 KOe for $SmCo_5$ on MgO. Maximum energy products of hard magnetic samples on MgO and glass are 12.8 MGOe and 5.5 MGOe, respectively, wherein the low value for sample on glass can be ascribed to random spin orientation due to the absence of epitaxial guidance from the glass substrate. When hard magnetic samples are transformed to exchange spring samples, magnetization rises and coercivity drops as expected, giving rise to higher energy product for sample on MgO from 12.8 MGOe to 14.5 MGOe. However, for the sample on glass the energy product drops from 5.5 MGOe to 5.3 MGOe due to reduced magnetization as a result of random spin orientation.

Temperature dependent studies on exchange-spring samples show a linear increase in coercivity with reducing the temperature in the 300 K - 100 K regime. The sample on MgO preserves its single step reversal behavior at lower temperature however, a shoulder develops in the hysteresis of the sample on glass at 150 K and 100 K, making the reversal a two-step process. This suggests that an exchange decoupling takes place at lower temperatures. This was attributed to microstructural effects as otherwise both samples should show this behavior as they both were grown under identical conditions.

As an extension of this project, it can be suggested that this decoupling behavior be studied in details by taking hysteresis measurements in the full temperature regime (5 K - 300 K) with an external field above 7 T (which is a limitation of our instrument that forbade saturating samples below 100 K). In addition, the soft layer thickness can be fine-tuned (1 nm - 10 nm) to see at what critical thickness the shoulder appears. Since single step reversal is vital for exchange-spring magnets for low temperature applications, a full understanding is necessarily before employing them.

* For temperature dependent *M-H* curves, *-H* to *+H* curve is manipulated based on *+H* to *-H* data to obtain a full hysteresis curve. Data was taken only for half hysteresis with the assumption that *M-H* curves are symmetric.

3.6 Reference

[1] Singh, A., Neu, V., Fähler, S., Nenkov, K., Schultz, L., Holzapfel, B., *Physical Review B*,*77*(10), 104443 (2008).

[2] Fullerton, E. E., Jiang, J. S., Rehm, C., Sowers, C. H., Bader, S. D., Patel, J. B., Wu, X. Z., *Applied Physics Letters*, *71*(11), 1579-1581 (1997).

[3] Zhang, L. N., Hu, J. F., Chen, J. S., Ding, J., *Journal of Magnetism and Magnetic Materials*, *321*(17), 2643-2647 (2009).

[4] Zangari, G., Lu, B., Laughlin, D. E., Lambeth, D. N., *Journal of Applied Physics*, *85*(8), 5759-5761 (1999).

[5] Benaissa, M., Krishnan, K. M., Fullerton, E. E., Jiang, J. S., *IEEE Transactions on Magnetics*, *34*(4), 1204-1206 (1998).

[6] Velu, E. M. T., Lambeth, D. N., *IEEE Transactions on Magnetics*, *28*(5), 3249-3254 (1992).

[7] Herzer, G., *IEEE Transactions on Magnetics*, *26*(5), 1397-1402 (1990).

[8] Neu, V., Häfner, K., Schultz, L., *Journal of Magnetism and Magnetic Materials*, *322*(9), 1613-1616 (2010).

[9] Skomski, R., *Journal of Applied Physics*, *76*(10), 7059-7064 (1994).

[10] Saravanan, P., Hsu, J. H., Reddy, G. L. N., Kumar, S., Kamat, S. V., *Journal of Alloys and Compounds*, *574*, 191-195 (2013).

[11] Malhotra, S. S., Liu, Y., Shan, Z. S., Liou, S., Stafford, D. C., Sellmyer, D.

J., *Journal of Applied Physics*,*79*(8), 5958-5960 (1996).

[12] Fischer, R., Schrefl, T., Kronmüller, H., Fidler, J., *Journal of Magnetism and Magnetic materials*,*153*(1), 35-49 (1996).

[13] Zhang, J., Song, J. Z., Zhang, Y., Wang, F., Chen, B. C., Shen, B. G., Sun, J. R., *IEEE Transactions on Magnetics*, *47*(10), 2792-2795 (2011).

[14] Goll, D., Seeger, M., Kronmüller, H., *Journal of Magnetism and Magnetic Materials*, *185*(1), 49-60 (1998).

[15] Shao, Y. Z., Zhong, W. R., Lan, T., Lee, R. H., *International Journal of Modern Physics B*, *20*(01), 61-72 (2006).

[16] Alben, R., Becker, J. J., Chi, M. C., *Journal of Applied Physics*, *49*(3), 1653-1658 (1978).

[17] Herzer, G., *Properties and Applications of Nanocrystalline Alloys from Amorphous Precursors* (pp. 15-34). Springer Netherlands (2005).

CHAPTER 4

FIELD-COOLED AND TEMPERATURE DEPENDENT MAGNETIC PROPERTIES OF $Au_{25}(SC_6H_{13})_{18}$ SPHERICAL NANOCLUSTER

The discovery of single molecule magnets (SMM's) has attracted great attention due to its importance in understanding magnetism in confined structures with finite numbers of spins and its applicability in a range novel applications from molecular memory to quantum computing [1-6], where well-defined ultra-small nanostructures are desired. Well-established SMM families such as Mn_{12}, Mn_4 and Fe_8 believed to have high-spin ground state, high-zero field splitting and very weak intermolecular magnetic interactions, so their magnetic properties were ascribed to an intramolecular origin [7,8]. These molecules showed interesting magnetic properties such as magnetic tunneling and slow relaxation at low temperatures [9-11]. Observation of ferromagnetism in confined nanostructures such as nanoparticles (NPs), nanowires (NWs) and nanoclusters (NCs) made of materials that are diamagnetic when in bulk form has generated wide attention in the past decade. This experimental work creates an impetus for understanding the origin of magnetism in nanoscale systems lacking magnetic atoms. In this chapter, an investigation of field-cooled (FC) and temperature-dependent magnetic properties of negatively charged $Au_{25}(SC_6H_{13})_{18}$ spherical nanoclusters of 1.3±0.1 nm is presented. The chapter begins with a general overview of previous reports on ferromagnetism observed in ultrafine diamagnetic systems and possible explanations followed by sample synthesis, structural analysis and magnetic measurements.

4.1 Ferromagnetism in ultrafine diamagnetic systems

Diamagnetism, a weak opposite response to an external magnetic field, is inherited with all materials to certain extent, yet its contribution is only effective in materials with no paramagnetic or ferromagnetic properties, that is materials with closed electronic shells. Noble metals such as Au, Ag and Pt are diamagnetic in bulk despite some of them have an unpaired electron (Au and Ag) due to closed *d* shells. However, they can exhibit exotic magnetic properties when the size is reduced to a few nanometers, and such properties have a strong correlation to the diameter [12-15]. In 1999, Hori *et al* [16] reported unusually large magnetic moments of up to 22 μ_B per particle for polyvinyl piridine (PVP) coated Au and Pd nanoparticles of 3 nm. Since then many researchers reported observation of non-zero magnetic properties in various diamagnetic systems both coated and non-coated with ligands.

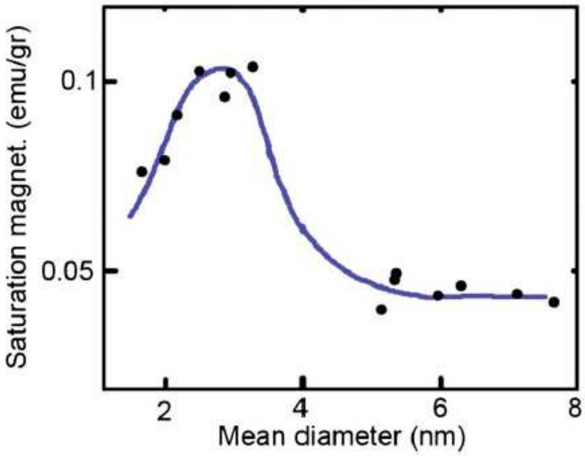

Figure 4.1 - Variation of saturation magnetic moment per unit mass with particle size for dodecannethiol-coated Au. Highest moment observed for 3 nm Au particles (adopted from ref[17], however this depends on the capping agent as some result linear variation with particle size [17].

In the prospect of band ferromagnetism (itinerant ferromagnetism), spontaneous ferromagnetism appears if the system meets the well-known Stoner criteria, i.e. $I.D(E_F) \geq 1$, where $D(E_F)$ and I are density of states (DOS) at the Fermi level and coupling constant which is a measure of Coulomb energy, respectively. When this condition is satisfied, a single band is split into two bands causing unequal spin (up and down) separation. Although I can be mostly a material dependent property, reduction of particle size which increases the surface atom fraction and also the influence from the outside environment (by ligands) can readily modify DOS, which may have re-enforced the Stoner criteria of these systems (see Chapter 1 for more details). Additionally, in the confined nanostructure limit, where the NP has a finite number of atoms and its diameter approaches the De Broglie wavelength, the quantum confinement effect kicks in [15, 18], which makes particles trapped in a potential well. Quantum confinement is responsible for narrow bands or discrete energy levels and opens up band gaps [17, 19] which can indeed induce ferromagnetic properties. Luo e*t. al.* [20] showed that bare Au clusters up to 147 atoms can have non-zero magnetic moments (1-5 μ_B) using first principle DFT spin-polarized calculations.

The most widely accepted theory of induced ferromagnetism is the creation of Fermi *d* holes on surface atoms, due to withdrawal of electrons from *d* shell (surface atoms have a reduced coordination which makes an electron withdrawal creates a net spin imbalance). So the filled *d* bands in the bulk state can now be considered partially filled. The creation of *d* holes can be a result of charge transfer from surface atoms to core atoms in order to stabilize the core in ultrafine limits or the interaction of surface atoms with outside environment (ligands) which may create electron deficiency on surface atoms due to pulling effect by ligands. He *et. al.* [21] argues, based on DFT calculations for ultrafine Ag clusters performed by Pereiro et al [22, 23], that noble metals which are non-magnetic in bulk due to equal and opposite spin populations, may create a state with a net magnetic moment due to charge transfer from the surface to the core, resulting holes in the *d* band of surface atoms. If the charge transfer is spin dependent this makes the NP ferrimagnetic-like [24] with opposite spins on the surface and in the core.

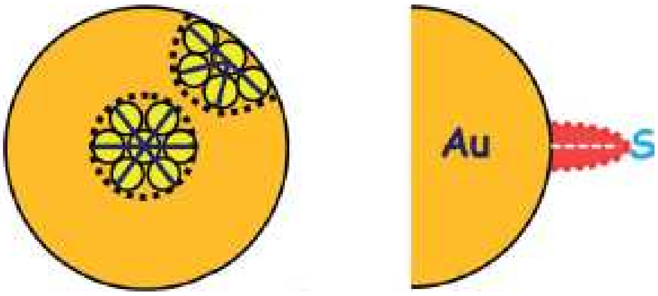

Figure 4.2 - Schematic illustration of polarization of Au surface atoms by which leads to Fermi hole creation. This shows that such holes exist on surface atoms due to low symmetry and coordination (adopted from ref [17]).

In practice, most of these NPs are coated with ligands to avoid aggregation. As an example Au is mostly coated with thiols, so the interaction of outermost Au atoms and the S atom (Au-S bond) is considered to be responsible for Fermi *d* holes due to electron pulling by S atom. This is supported by studies showing strong ferromagnetic properties in thiol stabilized ultrasmall Au NPs [25, 26]. However, it is important to mention that observed ligand induced magnetic properties have a strong co-relation to diameter and the strength of the ligand as shown in Figure 4.3. In general, this suggests that Au-S bond strength is primarily responsible but in contrary, some studies show that there is no significant enhancement with changing the ligand [21, 27, 28]. Also the closed nature of these NPs by ligands suggests that the magnetism is essentially local and it is argued that magnetic ordering in such systems is not due to exchange interaction as in itinerant magnets, but due to extremely high local anisotropy that blocks magnetic reversal. Particles as small as 1.5 nm show stable hysteresis loops even above room temperature or in other words they exhibit unusually large superparamagnetic blocking temperatures T_B that can be attributed to high anisotropy ($K_{aniso}.V = k_B.T_B$).

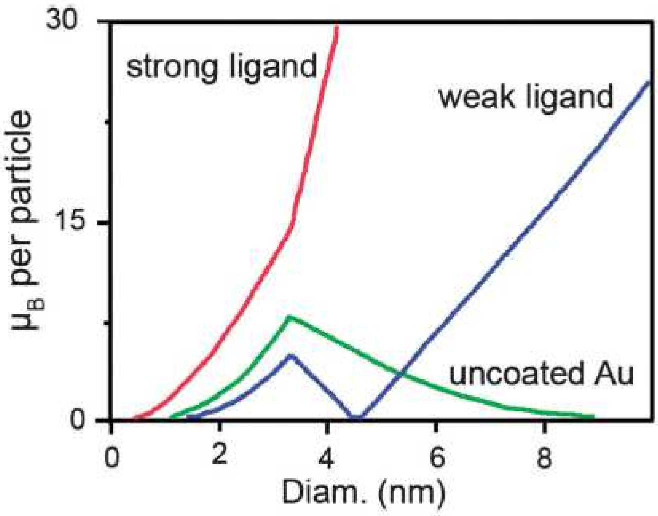

Figure 4.3 - Correlation between the ligand strength and the NP diameter. This shows that loss of moment with particle size for bare particles as predicted in DFT calculations, can be altered by the influence of the outside environment (adopted from ref [17, 21]).

Turning now to the reported values, the record coercivity value for Au NPs is 860 Oe at 5

K (250 Oe at 300 K) for 1.4 nm dodecanethiol (DT) capped Au particles [29] and the record saturation moment value, 5 emu/g at 5 K reported for 1.9 nm DT capped particles [30]. However, non-uniform size distribution and lack of controllability of number of Au atoms in each NP drive contradictory observations. Also it is not clear what fraction of surface atoms interact with ligands and whether it is consistent for all particles in the assembly. So well-defined nanostructures such as nanoclusters (NC) consisting finite number of atoms and well-defined size and composition is essential to overcome above statistical drawbacks in understanding the magnetism of ultrafine diamagnetic structures.

In this study, we examined a stable NC of 25 gold atoms and 18 thiol groups, $[Au_{25}(SC_6H_{13})_{18}]^-$. $Au_{25}(SC_6H_{13})_{18}$ cluster is spherical and atomically monodisperse with an icosahedral Au_{13} core surrounded by a shell of remaining 12 Au atoms, and stable in (-1) charge state. Figure 4.4 shows the common crystal structure of a spherical $Au_{25}(SR)_{18}$ nanocluster.

Figure 4.4 - Crystal structure of spherical $Au_{25}(SR)_{18}$ NC. This was derived based on DFT calculations. Color labeling-Orange(Au), Yellow(S), Gray(C), White(H). Adopted from ref [31].

Previous studies on Au_{25} clusters with other ligands show either paramagnetic or diamagnetic behavior biased by capping ligands [32]. Also, one study show that magnetic properties can be switched between diamagnetic and paramagnetic by changing the net charge of the cluster using oxidizing and reducing agents [33]. In contrast, here we observe strong ferromagnetic properties with an unprecedented temperature dependence, suggesting that such properties may be chemically induced.

4.2 Sample Preparation and Structure Analysis

Synthesis of $Au_{25}(SC_6H_{13})_{18}$ was carried out following a procedure published by Kim *et. al.* [34] with slight modifications to the purification steps [35]. These NCs were supplied by the E. Sinn group at the Chemistry Department of Western Michigan University. Further, they concluded that these NCs are molecularly precise with 7031 m/z ratio and (-1) charge state by mass spectroscopy studies. NCs were dissolved in acetonitrile to avoid any aggregation and used as is upon receiving. Sample preparation for magnetic measurements was done by drop casting the NC solution into a gelatin capsule and air dry it for several hours in a fume hood. This ensures that sample is properly attached to the sample holder (gelatin capsule in this case) that voids any relative motion between the sample and the holder, hence reduces measurement errors. For x-ray crystallography and x-ray photoelectron spectroscopy (XPS), samples were made by drop casting NC solution onto a cleaned Si wafer and air drying for several hours.

Structural properties of the sample has been studied by x-ray diffraction using a Panalytical X'Pert MRD spectrometer with Cu K_α radiation with 2θ varying from 10°-100°. X-ray spectrum (Figure 4.5) shows a narrow peak at $2\theta=33.03^0$ with the FWHM value 0.12^0. The wave vector length S corresponds to the above diffraction peak is 3.7 nm^{-1}, which was calculated using the relation,

$$S = \frac{2\sin\theta}{\lambda} \tag{4.1}$$

where λ is the wavelength of Cu K_α radiation (0.154 nm). This value of S agrees with reported values (~ 4 nm^{-1}) for other $Au_{25}(SR)_{18}$ nanoclusters with FCC crystal structure determined by DFT calculations [36-38].

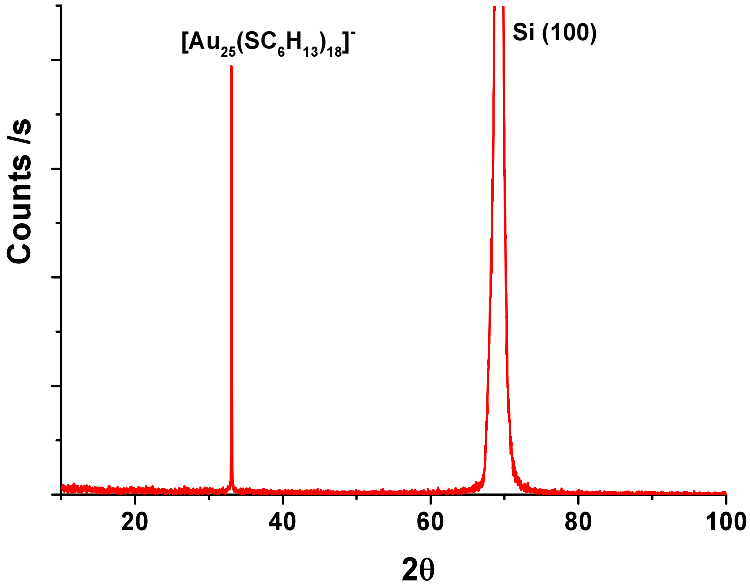

Figure 4.5 - Room temperature X-ray diffraction pattern of $[Au_{25}(SC_6H_{13})_{18}]^-$ sample.

In addition, an elemental analysis was performed by XPS for the drop casted sample to identify any magnetic impurities. Both the survey spectra (Figure 4.6a) and subsequent high resolution spectra (Figure 4.6b) for suspected impurities were acquired from Physical Electronics PHI 5000 dual anode/fixed lens spectrometer equipped with a monochromatic Al x-ray source. The full range (0-1100 eV) survey spectra shows the presence each element; Au, C, S, O. There is no signal in the 650-900 eV range, the range corresponds to Fe, Co, Ni and Mn, can be observed in the survey spectra. The high resolution spectra confirms the absence of any ferromagnetic elements as no signal for Fe, Co, Ni and Mn 2p3 spectral line can be detected.

4.3 Magnetic Measurements

Magnetic properties were measured using a Superconducting Quantum Interference Device (SQUID) magnetometer (MPMS, Quantum Design, Inc) with 7 T maximum applied field. Three types of measurements were obtained. First, hysteresis measurements were obtained at 7 K for different cooling fields followed by measurements at different temperatures at constant and no cooling field. Finally, thermomagnetic curves (FC/ZFC) for temperatures 5-310 K were obtained. Figure 4.7 shows selected hysteresis curves (for clarity) measured at 7 K under different cooling fields, varied from 0-7000 Oe, after the subtraction of high field diamagnetic contribution. It can be seen that there is a clear correlation between magnetic properties and cooling field. The wide and short hysteresis curves observed at low cooling fields have transformed to narrow and tall hysteresis with increased remanence and saturation moments at large cooling fields. This behavior is similar to a magnetic phase transformation from hard magnetic to soft magnetic surprisingly by field cooling.

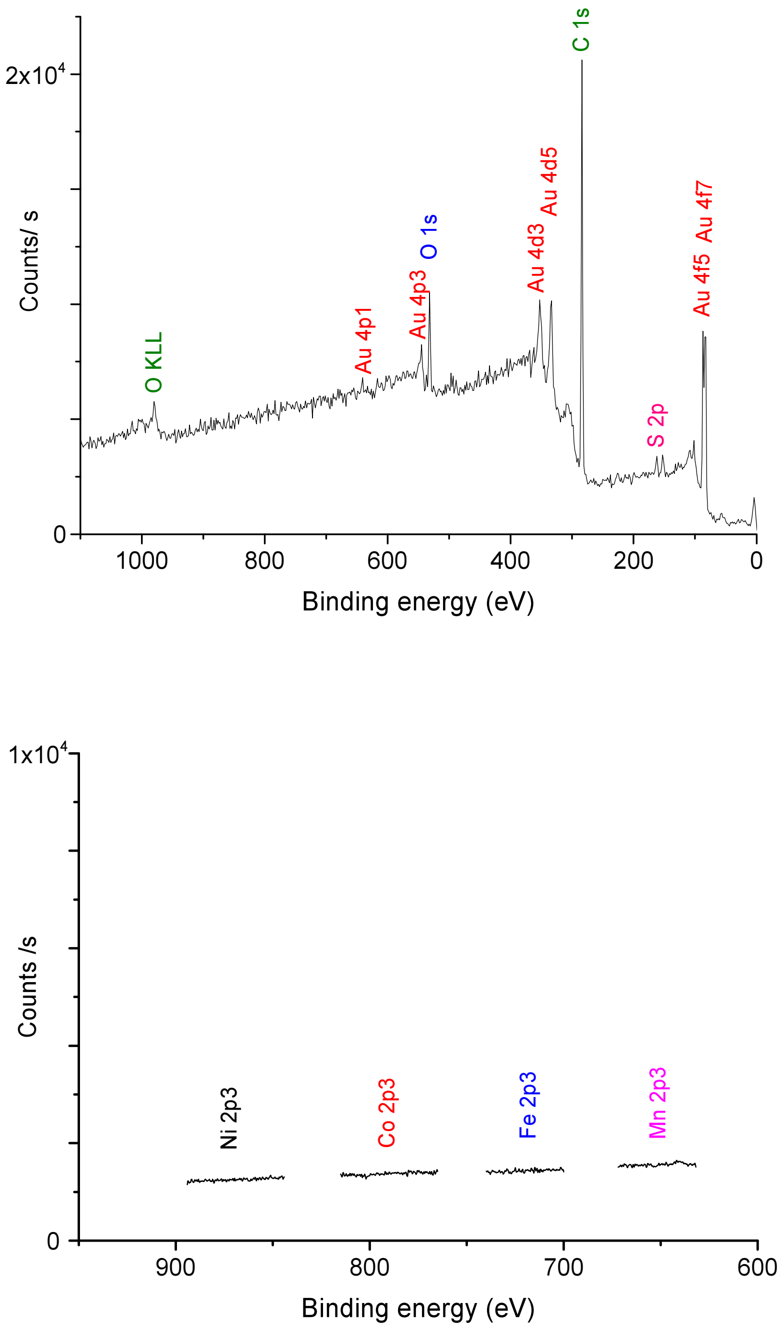

Figure 4.6 a) XPS survey spectra and b) High resolution spectra for Fe, Co, Ni and Mn 2p3 peaks (Au, C, S, O peaks not shown for clarity).

Also observation of a slight offset of the FC hysteresis loops (exchange-bias field, H_{EB}) that changes with the cooling fields, suggests that the cluster has “memory effect”, usually originated by a ferromagnetic/antiferromagnetic (or ferromagnetic/ferrimagnetic) interface that creates a non-zero exchange-bias (EB) field. Previous studies which observed EB like effect in Au NP assemblies argue that it arises due to wide distribution of sizes [15] or “locked” spins (spins remains unaffected when the field is reversed) at “vulnerable” lattice sites that creates a magneto-elastic effect on neighboring spins [39]. However, we stress that observed H_{EB} values may have been slightly affected by the trapped flux of SQUID coils although the superconducting magnet was relaxed by oscillate mode to minimize the effect of trapped flux.

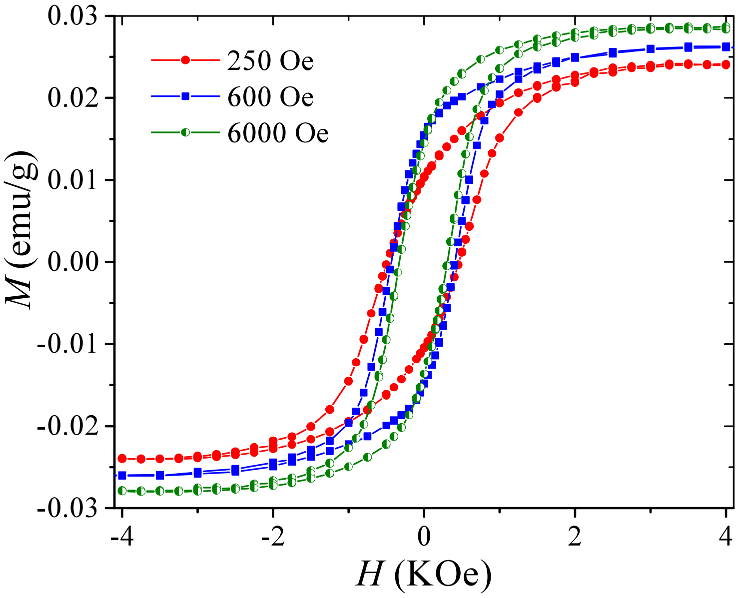

Figure 4.7 - Hysteresis curve variation with the cooling field at 7 K. With increasing the cooling field the saturation magnetization increases while the coercivity decreases.

Figure 4.8a-d show the variation of coercivity (H_C), exchange-biased field (H_{EB}), remanence (M_r) and saturation (M_S) magnetic moments with the cooling field at 7 K. At small cooling fields, M_r increases rapidly while M_S stays nearly constant. This indicates that the FM phase attempts to align with the cooling field but shows no growth in size at smaller fields (< 100 Oe). With increasing the cooling field, both Mr and M_S increase rapidly indicating the growth and aligning of the FM phase, but that trend starts changing for cooling fields above 2000 Oe with Mr slightly decreasing before saturation, which could be due to the fact that the FM phase shifts from a single domain-like state to an inhomogeneous magnetic state (multi domains) with its growth. In addition, H_C and H_{EB} show a unique dependency with the cooling field. At smaller cooling fields (< 600 Oe), both H_C and H_{EB} increase with the cooling field which reveals that the H_C is primarily driven by the EB effect that depends on the AFM ordering indeed. This also implies that the AFM phase has been fully ordered by FC=600 Oe from a frozen state at lower cooling fields. In the large cooling field regime (600-7000 Oe), H_C decreases exponentially while H_{EB} decreases slowly with increasing the cooling field. The maximum H_C and H_{EB} are 480 Oe and 17 Oe for FC=600 Oe, respectively. This behavior can be attributed to the growth of the FM phase with increasing the cooling field. As the FM phase grows, the EB effect diminishes as it is a surface effect. This is observed in layered FM/AFM structures where the FM layer thickness determines the strength of the EB effect. Moreover, the exponential decay in H_C suggests that the growth of the FM phase is unprecedented in the 600-4000 Oe cooling field regime before it saturates at higher cooling fields.

Also, the magnitude of the H_{EB} in contrast to H_C suggests that this magnetic cluster is dominated by the FM phase. A similar discussion can be found elsewhere [40] for

FC-dependent magnetic properties of hole-doped perovskite cobaltite compounds. Also here, the absence of spin-flop behavior at both low and high cooling fields affirm that the system is predominantly FM.

To investigate the temperature dependence, hysteresis measurements were taken for various temperatures from 7 K to 310 K with and without applying any cooling fields. Figure 4.9 and Figure 4.10 show hysteresis curves for selected temperatures for FC=1000 Oe and ZFC after removing high field diamagnetic contribution, respectively.

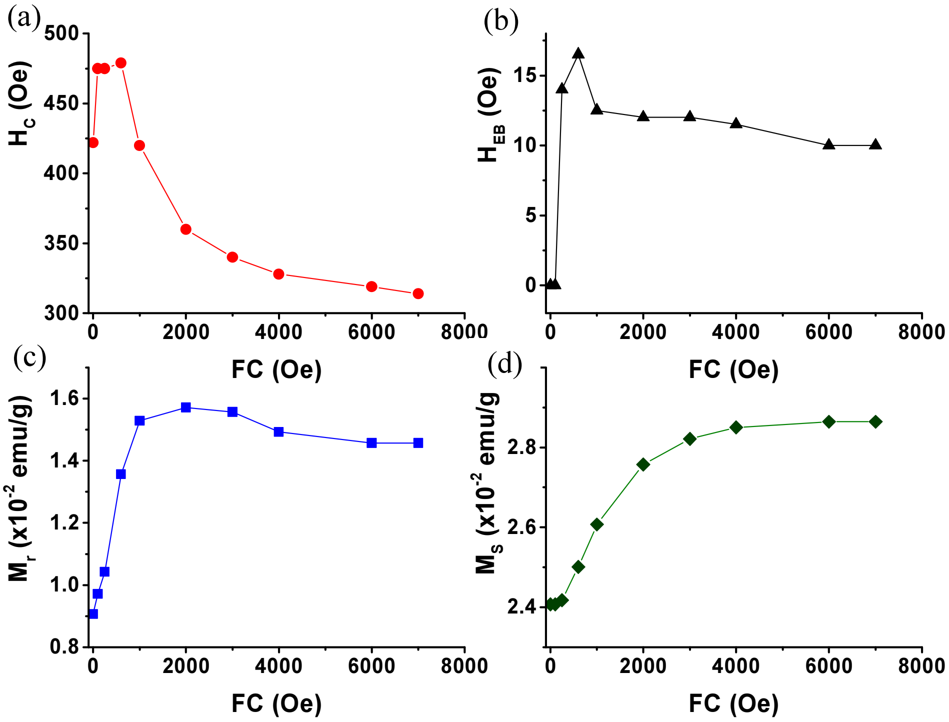

Figure 4.8a-d - Variation of H_C, H_{EB}, Mr, M_S with the cooling field at 7 K, respectively.

The choice of cooling field was 1000 Oe, because H_C values at 7 K for FC and ZFC measurements were very close, which will help us to understand the effect of temperature with minimum interference of cooling field. In both cases, it can clearly be seen that the hysteresis curves first shrink and then widen at higher temperatures.

To further understand this behavior, the variation of H_C, H_{EB}, Mr, M_S with the temperature were plotted (Figure 4.11a-d) from data extracted from FC and ZFC hysteresis curves. H_C shows a clear inverse relation with the temperature for 7-125 K temperature regime (low temperature regime) under both FC and ZFC conditions.

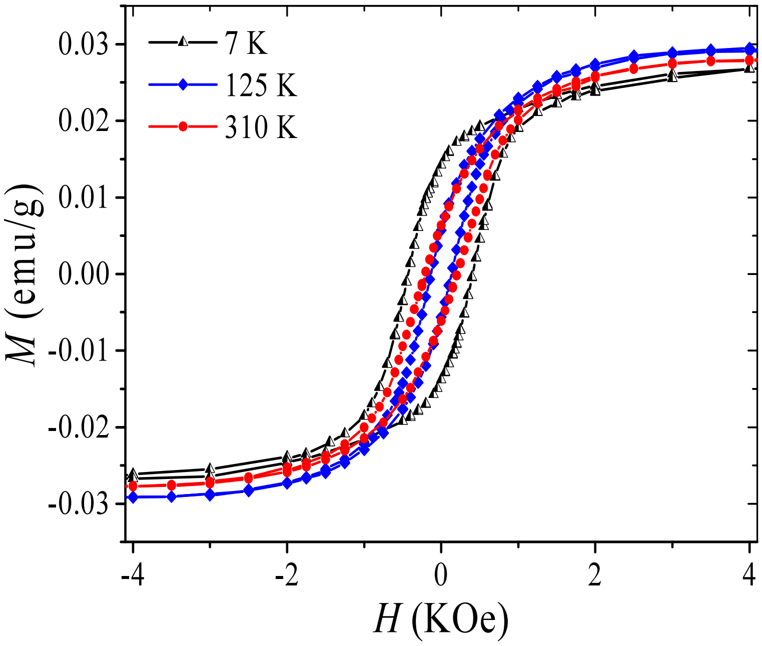

Figure 4.9 - Field-cooled (FC) hysteresis (H_{FC}=1000 Oe) curves for selected temperatures

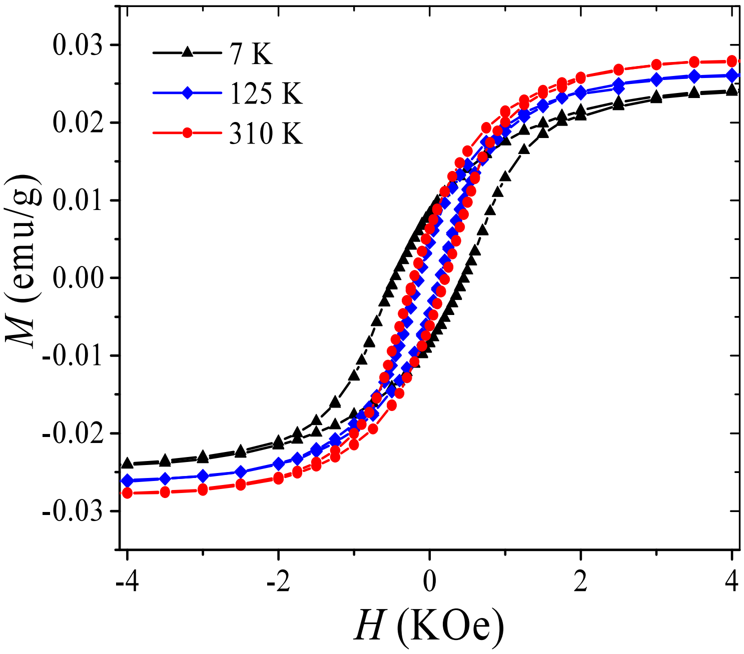

Figure 4.10 - Zero field-cooled (ZFC) hysteresis curves for selected temperatures.

This behavior is typical for FM systems and it can be ascribed to thermally induced spin fluctuations lowering the H_C with increasing the temperature. In addition, H_{EB} (from FC measurements) promptly decreases with the temperature and comes to zero at 125 K, affirming that the exchange-bias or possibly the AFM phase exists only at low temperatures. In the high temperature regime (125-310 K), H_C steadily increases and saturates at 310 K in both FC and ZFC measurements. This abnormal increase in H_C with the temperature proposes that the material may undergo a phase transition at 125 K, however temperature dependent optical absorption spectroscopy data for the same NC [35] does not reveal any deviations in this temperature regime. In addition, it also excludes the possibility of cluster aggregation at lower temperatures.

Also it is very important to mention that all hysteresis measurements are fully reversible. As an example, if we take respective FC hysteresis measurements at FC=1000, 2000, 3000 Oe and again at 1000 Oe, two curves measured at 1000 Oe are almost identical. A similar behavior can be observed for temperature dependent measurements as well. This observation can be correlated with recent reports on reversible phase transitions between crystalline and amorphous for metal organic compounds [41], a property not observed in conventional magnetic materials that undergo phase transitions. This emphasizes the importance of temperature dependent XRD and HRTEM measurements,which could give a greater insight to structural changes with the temperature (if any).

The variation of Mr for both FC and ZFC measurements follow a similar trend as H_C, with minimum values at 125 K. However, Mr values extracted from FC curves are higher for all temperatures compared to Mr values extracted from ZFC curves. This is a result of magnetic ordering by the cooling field. Saturation moment M_S increases with temperature for ZFC case however its variation is non-monotonic as shown in Figure 4.11-d. Nonetheless, FC M_S has a random variation with the temperature with a clear maximum at 125 K.

An increase in magnetic moment with the temperature has been reported previously for a number of AFM and FIM systems [42-44] due to thermal induced magnetization. On the other hand sub-lattices of an excited AFM NP can have slightly different precision angles that result a non-zero moment and it linearly increases with the temperature [45]. Further, canted surface and interface spins of the AFM (or FIM) phase of NPs arising from spin-glass sites and defects, can result unexpected temperature dependent magnetic properties [46]. This effect is dominant in ultrafine particles as canted spin density increases with decreasing particle size due to the creation of reduced symmetry environments on the particle surface. However such phenomena do not explain the variation of M_S beyond 125 K, at which the H_{EB} reduced to zero suggesting that the AFM phase does not exists, and more importantly it does not explain the unprecedented behavior of H_C with the temperature.

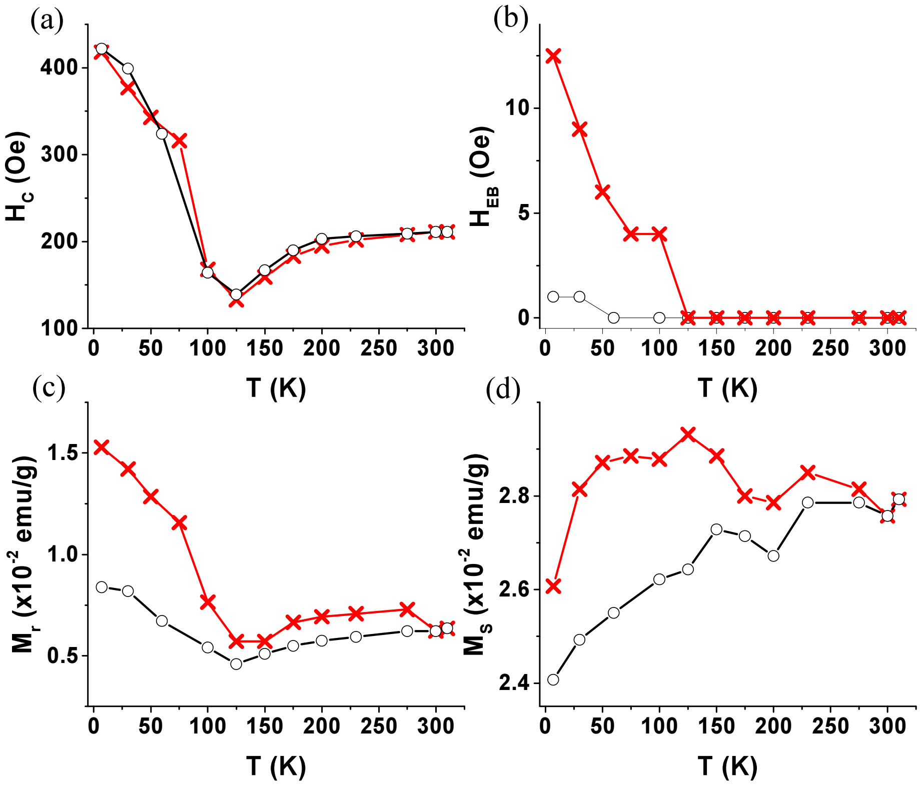

Figure 4.11a-d - Variation of H_C, H_{EB}, Mr, M_S with the temperature under Field-Cooled (at H_{FC}=1000 Oe Red) and Zero field-cooled (Black) conditions.

In addition, it is possible that cluster behaves as a spin glass system at low temperature, where magnetic moments are frozen into random orientations with no long-range interactions. Although, spin glasses are considered to be kinetically trapped non-equilibrium systems due to frustration and disorder, ordered crystal structures showing spin glass freezing have been reported [47, 48]. In one proposed mechanism, with increasing temperature frozen spins can become relaxed that promotes long-range ordering by inter-cluster interactions (exchange-interaction, RKKY, super-exchange or dipolar) resulting increased magnetic moment with temperature [49].

Figure 4.12 shows thermomagnetic measurements (FC-ZFC) performed for 5-310 K temperature range for three cooling fields and applied fields; 500 Oe, 1000 Oe and 2000 Oe. Also, it is important to mention that ZFC measurements were followed by FC measurements and the diamagnetic contribution has not been removed (unlike in hysteresis curves) as it has a temperature dependence. If we consider magnitude of the magnetic moment, it is higher at 1000 Oe than that at 500 Oe as expected due to the nature of more ferromagnetic ordering by extra cooling and applied field. However, moment at 2000 Oe is surprisingly lower than that at 1000 Oe. This observation suggests a transformation of the magnetic state from an ordered (more ordered) to a disordered (less ordered) state. At this point it is not clear the phenomena behind this unambiguous observation but it is possible that ferromagnetic signal is suppressed by high field diamagnetic susceptibility. Further, there are two transitions can clearly be seen in all plots; one in the low temperature regime and the other in the high temperature regime. The peak in the low temperature regime shifts left with increasing the cooling field from

112 K at 500 Oe to 107 at 2000 Oe. This transition does not represent any blocking temperature or superparamagnetic transition as the system is ferromagnetic even at 310 K.

Also, similarly, the jump in the high temperature regime also shifts towards left (285 K for 500 Oe and 270 K for 2000 Oe) but the jump is significant in the 1000 Oe FC-ZFC curve. Such transitions may represent spin reorientation of the AFM or FIM phase of the system guided by the field and the spin relaxation with the temperature. This can be supported by the fact that H_{EB}=0 beyond 125 K (no AFM or FIM phase exists), yet it doesn't explain (or even contradicts) the increase in H_C with the temperature. Similar jumps in M-T curves in lower regimes for Au NP and NC systems have been accounted to interaction between core and shell with opposite spin orientations [14, 24].

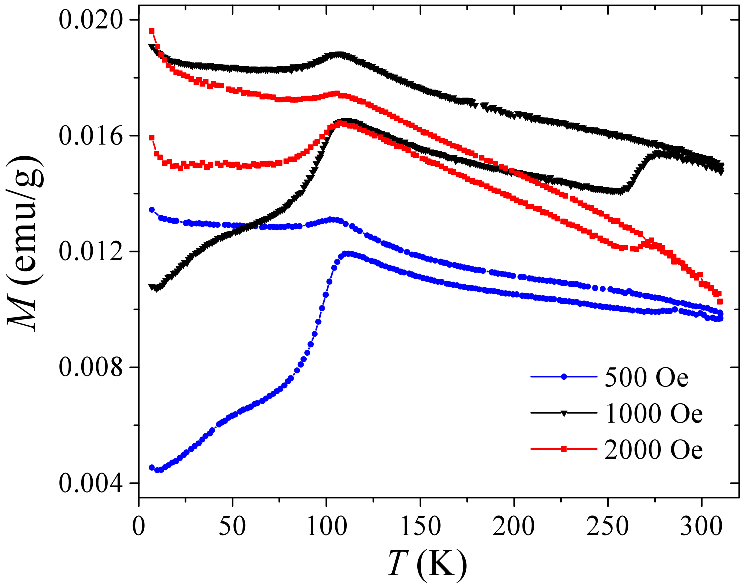

Figure 4.12 - FC-ZFC measurements in the 5-310 K range for 500 Oe, 1000 Oe and 2000 Oe cooling and applied fields.

4.4 Conclusions and Future Work

In this work, magnetic properties of $[Au_{25}(SC_6H_{13})_{18}]^-$ spherical nanocluster of 1.3±0.1 nm diameter were studied. Hysteresis and thermomagnetic measurements were taken under FC and ZFC conditions at various temperatures from 5-310 K. FC hysteresis measurements performed at low temperatures suggest that the cluster behaves as an exchange bias system which is typically due to the exchange interaction between FM and AFM phase. The unique dependency of magnetic properties with the cooling field suggests that the magnetic phase transforms from an exchange bias system to a FM dominated phase, that grows with the cooling field. The unusual and unique dependence of magnetic properties with the temperature suggests the possibility of phase transformation or thermally induced long range interactions beyond a critical temperature. Further, thermomagnetic curves show jumps in M-T plots in both lower and higher temperatures for all curves (for all cooling fields) which might be due spin re-orientation of AFM (or FIM) phase. Also, surprisingly, the M-T plots obtained at 1000 Oe cooling field has a higher magnetization than that was taken at 2000 Oe cooling field.

All these observations suggest that further analysis is needed to fully understand these observations. As an example, spin polarized neutron scattering is probably the most informative study as it can map the spin arrangement of the NC and determine its magnetic state at specific temperature and field. Also, AC susceptibility measurements can give an insight to magnetization dynamics by exploring phenomena such as relaxation and magnetic phase transitions. Further, temperature and field dependent impedance measurements (by PPMS) might also be useful as change in magnetic state is usually reflected in conductivity measurements. Also temperature dependent structural studies by XRD or HRTEM will reveal how the crystal structure changes (if any) with the temperature, which might answer questions erupted with temperature dependent magnetic measurements.

4.5 Reference

[1] Mannini, M., Pineider, F., Sainctavit, P., Danieli, C., Otero, E., Sciancalepore, C., Sessoli, R., *Nature Materials*, *8*(3), 194-197 (2009).

[2] Li, C., Fan, W., Lei, B., Zhang, D., Han, S., Tang, T.,Zhou, C., *Applied Physics Letters*, *84*(11), 1949-1951(2004).

[3] Bogani, L., Wernsdorfer, W., *Nature Materials*, *7*(3), 179-186 (2008).

[4] Leuenberger, M. N., Loss, D., *Nature*, *410* (6830), 789-793 (2001).

[5] Aubin, S. M., Sun, Z., Eppley, H. J., Rumberger, E. M., Guzei, I. A., Folting, K., Hendrickson, D. N., *Inorganic Chemistry*, *40*(9), 2127-2146 (2001).

[6] Christou, G., Gatteschi, D., Hendrickson, D. N., Sessoli, R., *Mrs Bulletin*, *25*(11), 66-71 (2000).

[7] Gomes, A. M., Novak, M. A., Sessoli, R., Caneschi, A., Gatteschi, D., *Physical Review B*, *57*(9), 5021 (1998).

[8] Lascialfari, A., Jang, Z. H., Borsa, F., Carretta, P., Gatteschi, D., *Physical Review Letters*, *81*(17), 3773 (1998).

[9] Pederson, M. R., Khanna, S. N., *Physical Review B*, *60*(13), 9566 (1999).

[10] Hernandez, J. M., Zhang, X. X., Luis, F., Bartolomé, J., Tejada, J., Ziolo, R., *Europhysics Letters*, *35*(4), 301 (1996).

[11] Bokacheva, L., Kent, A. D., Walters, M. A., *Physical Review Letters*, *85*(22), 4803 (2000).

[12] Negishi, Y., Tsunoyama, H., Suzuki, M., Kawamura, N., Matsushita, M. M., Maruyama, K., Tsukuda, T., *Journal of the American Chemical Society*, *128*(37), 12034-12035 (2006).

[13] Michael, F., Gonzalez, C., Mujica, V., Marquez, M., Ratner, M. A., *Physical Review B*, *76*(22), 224409 (2007).

[14] Maitra, U., Das, B., Kumar, N., Sundaresan, A., Rao, C. N. R., *ChemPhysChem* *12*(12), 2322-2327 (2011).

[15] Dutta, P., Pal, S., Seehra, M. S., Anand, M., & Roberts, C. B., *Applied Physics Letters*, *90*(21), 213102-213102 (2007).

[16] H. Hori, T. Teranishi, Y. Nakae, Y. Seino, M. Miyake, S. Yamada, *Physics Letters A*, 263, 406 (1999).

[17] Nealon, G. L., Donnio, B., Greget, R., Kappler, J. P., Terazzi, E., Gallani, J. L., *Nanoscale*, *4*(17), 5244-5258 (2012).

[18] Zhu, M., Aikens, C. M., Hollander, F. J., Schatz, G. C., Jin, R., *Journal of the American Chemical Society*, *130*(18), 5883-5885 (2008).

[19] Rosch, N., Ackermann, L., Pacchioni,G., *Journal of the American Chemical Society*, *114*, 3459 (1992).

[20] Luo, W., Pennycook, S. J., Pantelides, S. T., *Nano Letters*, 7, 3134 (2007).

[21] He, L., *Journal of Physical Chemistry C, 114*(29), 12487-12489 (2010).

[22] Pereiro, M.; Baldomir, D., *Physical Review A*, *72*, 045201 (2005).

[23] Pereiro, M.; Baldomir, D.; Arias, J. E., *Physical Review A*, *75*, 063204 (2007).

[24] Wu, C. M., Li, C. Y., Kuo, Y. T., Wang, C. W., Wu, S. Y., Li, W. H., *Journal of Nanoparticle Research*, *12*(1), 177-185 (2010).

[25] Harbola, M. K., Sahni, V., *Physical Review B*, *37*(2), 745 (1988).

[26] Hori, H., Yamamoto, Y., Iwamoto, T., Miura, T., Teranishi, T., Miyake, M., *Physical Review B*, *69*(17), 174411 (2004).

[27] Guerrero, E., Munoz-Marquez, M. A., Fernandez, A., Crespo, P., Hernando, A., Lucena, R., Conesa, J. C., *Journal of Applied Physics*, *107*(6), 064303 (2010).

[28] Mohapatra, S., Kumar, R. K., Maji, T. K., *Chemical Physics Letters*, *508*(1), 76-79 (2011).

[29] Crespo, P., Litrán, R., Rojas, T. C., Multigner, M., De la Fuente, J. M., Sánchez-López, J. C., Fernández, A., *Physical Review Letters*, *93*(8), 087204 (2004).

[30] Garitaonandia, J. S., Insausti, M., Goikolea, E., Suzuki, M., Cashion, J. D., Kawamura, N., Rojo, T., *Nano Letters*, *8*(2), 661-667 (2008).

[31] Akola, J., Walter, M., Whetten, R. L., Häkkinen, H., Grönbeck, H., *Journal of the American Chemical Society*, *130*(12), 3756-3757 (2008).

[32] Krishna, K. S., Tarakeshwar, P., Mujica, V., & Kumar, C. S., *Small*, *10*(5), 907-911 (2014).

[33] Zhu, M., Aikens, C. M., Hendrich, M. P., Gupta, R., Qian, H., Schatz, G. C., Jin, R., *Journal of the American Chemical Society*, *131*(7), 2490-2492 (2009).

[34] Kim, J., Lema, K., Ukaigwe, M., Lee, D., *Langmuir*, 23, 7853–7858 (2007).

[35] Devadas, M. S., Thanthirige, V. D., Bairu, S., Sinn, E., Ramakrishna, G., *The Journal of Physical Chemistry C*, *117*(44), 23155-23161 (2013).

[36] Lavenn, C., Albrieux, F., Bergeret, G., Chiriac, R., Delichère, P., Tuel, A., Demessence, A., *Nanoscale*, *4*(23), 7334-7337 (2012).

[37] Akola, J., Walter, M., Whetten, R. L., Häkkinen, H., Grönbeck, H., *Journal of the American Chemical Society*, *130*(12), 3756-3757 (2008).

[38] Iwasa, T., Nobusada, K., *The Journal of Physical Chemistry C*, *111*(1), 45-49 (2007).

[39] Teng, X., Han, W. Q., Ku, W., Hücker, M., *Angewandte Chemie*, *120*(11), 2085-2088 (2008).

[40] Tang, Y. K., Sun, Y., & Cheng, Z. H., *Journal of Applied Physics*, *100*(2), 023914-023914 (2006).

[41] Tian, C. B., Chen, R. P., He, C., Li, W. J., Wei, Q., Zhang, X. D., Du, S. W., *Chemical Communications, 50*(15), 1915-1917 (2014).

[42] Harris, J. G. E., Grimaldi, J. E., Awschalom, D. D., Chiolero, A., Loss, D., *Physical Review B*, *60*(5), 3453 (1999).

[43] Vollath, D., Szabó, D. V., Willis, J. O., *Materials Letters*, *29*(4), 271-279 (1996).

[44] Bañobre-López, M., Vázquez-Vázquez, C., Rivas, J., López-Quintela, M. A., *Nanotechnology*, *14*(2), 318 (2003).

[45] Mørup, S., Frandsen, C., *Physical Review Letters*, *92*(21), 217201 (2004).

[46] Jacobsen, H., Lefmann, K., Brok, E., Frandsen, C., Mørup, S., *Journal of Magnetism and Magnetic Materials*, *324*(19), 3218-3222 (2012).

[47] Goremychkin, E. A., Osborn, R., Rainford, B. D., Macaluso, R. T., Adroja, D. T., Koza, M., *Nature Physics*, *4*(10), 766-770 (2008).

[48] Krimmel, A., Hemberger, J., Nicklas, M., Knebel, G., Trinkl, W., Brando, M., Ressouche, E., *Physical Review B*, *59*(10), R6604 (1999).

[49] Knepper, J. W., Yang, F. Y., *Physical Review B*, *71*(22), 224403 (2005).

CHAPTER 5

SUMMARY AND OUTLOOK

Nanoscale ferromagnetic materials and structures are promising systems to efficient applications and understand new phenomena in magnetism. Three projects discussed in this dissertation focused in developing new fabrication techniques as well as investigating ill-understood phenomena in nanoscale magnetism. In the first project, we utilized a novel fabrication technique, roll-to-roll nanoimprinting, that can be utilized in commercial manufacturing of thin film devices, to develop nanostripe-based oriented flexible magnetic thin films with enhanced properties using patterned gratings. Observed moderate coercivities at room temperature are ascribed to shape anisotropy of nanostripes and large energy products are a result of improving coercivity without compromising areal density of the magnetic material. Based on temperature dependent hysteresis measurements, we understood that the reversal process is dominated by the curling reversal mechanism. As an extension to this project, I propose to develop hard and exchange-coupled magnetic nanostripe-based thin films to further enhance their properties by combining the shape and magnetocrystalline anisotropies. Also, it is interesting to study how the non-trivial reversal process of hard and exchange-coupled thin films change when their shape is tailored.

In the second project, we tried to understand the role of substrate in controlling properties of thin hard and exchange-coupled magnetic films. Two substrates, MgO(100) and glass, have been used and examined for how they control the crystallinity and grain growth of the underlayer (Cr) and magnetic layers, grown under identical conditions. From structural studies and surface analysis, we found that the underlayer has different growth conditions on MgO(100) and glass at 500^0 C due to epitaxial match/mismatch and possible de-wetting conditions. Although both samples resulted similar and reasonably high H_C values, we believe that their reversal mechanisms are different due to dissimilar microstructure formation. Reversal of samples grown on MgO(100) are mostly dominated by epitaxial guidance by MgO(100), while samples grown on glass believed to be dominated by pinning and isolated-like grain formation. Further, glass resulted lower maximum energy products despite having similar coercivities as of samples on MgO(100), due to random orientation of magnetic grains, evident by x-ray diffraction studies. Temperature dependent hysteresis measurements for exchange-coupled samples show a step formation only for the sample grown on glass below 150 K. This exchange-decoupling nature can be seen as microstructure driven and need further analysis to understand the cause. One noteworthy result in this study is that high H_C values do not always represent good hard magnetic properties as their $(BH)_{max}$ values can be affected by random distribution of grains. As an extension, I propose to study this exchange-decoupling behavior in details by taking measurements in the full temperature regime (5 K - 300 K) as a complete understanding is necessary before employing them in low temperature applications.

In the third project, we explored field-cooled (FC) and temperature dependent magnetic properties of $Au_{25}(SC_6H_{13})_{18}$ nanocluster. Although ferromagnetic properties in ultrafine diamagnetic systems have been reported before, in this study we observed unique dependence of magnetic properties with cooling field and temperature. FC measurements show a shift in M-H loop that suggests the existence of an exchange-bias (EB) like effect or in other words the possible existence of both ferromagnetic and antiferromagnetic phases in the cluster. Further, magnetization of the ensemble rises while the coercivity drops with increasing the cooling field. This can be understood as loss of EB effect and rise of FM nature in the cluster (FM phase grows or a part AFM phase is transformed to FM phase by cooling field) as it explains the increase in magnetization and decrease in coercivity. In temperature dependent measurements, we observed that the magnetization rises but coercivity first drops and then rises with the temperature. This observation can be a result of multiple phenomena such as thermal induced magnetization as observed in AFM materials and magnetic or structural phase transitions. Thermomagnetic measurements (FC/ZFC) show two clear transitions in mid temperature (~110 K) and high temperature (~260 K) regimes. All these observations suggest further investigations by neutron scattering, temperature dependent structural studies and EPR measurements that can reveal more details and possibly answer these unique but peculiar observations.

BIBLIOGRAPHY

Akola, J., Walter, M., Whetten, R. L., Häkkinen, H., Grönbeck, H., *Journal of the American Chemical Society*, 130(12), 3756-3757 (2008).

Alben, R., Becker, J. J., Chi, M. C., *Journal of Applied Physics*, 49(3), 1653-1658 (1978).

Ali, M., Marrows, C. H., Al-Jawad, M., Hickey, B. J., Misra, A., Nowak, U., Usadel, K. D., *Physical Review B*, 68(21), 214420 (2003).

Allwood, D., Xiong, G., C. Faulkner, C. , Atkinson, D., Petit, D., P. Cowburn, R., *Science* 309, 1688 (2005).

Arora, S. K., B. J. O'Dowd, B. Ballesteros, P. Gambardella, I. V. Shvets, *Nanotechnology* 23, 23 (2012).

Aubin, S. M., Sun, Z., Eppley, H. J., Rumberger, E. M., Guzei, I. A., Folting, K., Hendrickson, D. N., *Inorganic Chemistry*, 40(9), 2127-2146 (2001).

Bang, W., Kim, K., Rathnayaka, K. D. D., Teizer, W., Lyuksyutov, I. F., Naugle, D. G., *Physica C Superconductivity* 493, 89-92 (2013).

Bañobre-López, M., Vázquez-Vázquez, C., Rivas, J., López-Quintela, M. A., *Nanotechnology*, 14(2), 318 (2003).

Benaissa, M., Krishnan, K. M., Fullerton, E. E., Jiang, J. S., *IEEE Transactions on Magnetics*, 34(4), 1204-1206 (1998).

Bhowmik, R. N., Ranganathan, R., Nagarajan, R., Ghosh, B., Kumar, S., *Physical Review B*,72(9), 094405 (2005).

Bisio, F., Moroni, R., de Mongeot, F. B., Canepa, M., Mattera, L., *Physical Review Letters*, 96(5), 057204 (2006).

Bogani, L., Wernsdorfer, W., *Nature Materials*, 7(3), 179-186 (2008).

Bokacheva, L., Kent, A. D., Walters, M. A., *Physical Review Letters*, 85(22), 4803 (2000).

Borca, B., Fruchart, O., David, P., Rousseau, A., Meyer, C., *Applied Physics Letters*, 90(14), 142507 (2007).

Borca, B., Fruchart, O., Meyer, C., *Journal of Applied Physics*, 99, 08Q514 (2006).

Boulle, O., Kimling, J., Warnicke, P., Kläui, M., Rüdiger, U., Malinowski, G., Faini, G., *Physical Review Letters*, 101(21), 216601 (2008).

Brown, W. F., *Physical Review* 130, 1677 (1963).

Bruno, P., J-P. Renard., *Applied Physics A: Materials Science & Processing* 49(5), 499-506 (1989).

Burrowes, C., Mihai, A. P., Ravelosona, D., Kim, J. V., Chappert, C., Vila, L., Attané, J. P., *Nature Physics*, 6(1), 17-21 (2009).

Chappert, C., Bernas, H., Ferré, J., Kottler, V., Jamet, J. P., Chen, Y., Launois, H., *Science*, 280(5371), 1919-1922 (1998).

Cheng, R., Guslienko, K., Fradin, F., Pearson, J., Ding, H., Li, D., Bader, S., *Physical Review B* 72, 014409 (2005).

Christou, G., Gatteschi, D., Hendrickson, D. N., Sessoli, R., *Mrs Bulletin*, 25(11), 66-71

(2000).

Coehoorn, R., De Mooij, D. B., De Waard, C., *Journal of Magnetism and Magnetic Materials*, 80(1), 101 (1989).

Coey, J. M., Magnetism and magnetic materials. *Cambridge University Press* (2010).

Constantinides, S., The demand for rare earth materials in permanent magnets, *Arnold Magnetic Technologies*.

Crespo, P., Litrán, R., Rojas, T. C., Multigner, M., De la Fuente, J. M., Sánchez-López, J. C., Fernández, A., *Physical Review Letters*, 93(8), 087204 (2004).

Croat, J. J., Herbst, J. F., Lee, R. W., Pinkerton, F. E., *Journal of Applied Physics* 55 2078 (1984).

Devadas, M. S., Thanthirige, V. D., Bairu, S., Sinn, E., Ramakrishna, G., *The Journal of Physical Chemistry C*, 117(44), 23155-23161 (2013).

Donahue, M. J., Porter, D. G., OOMMF User's guide, *NIST* (1999).

Dubowik, J., *Physical Review B* 54(2), 1088 (1996).

Dutta, P., Pal, S., Seehra, M. S., Anand, M., Roberts, C. B., *Applied Physics Letters*, 90(21), 213102-213102 (2007).

Elmers, H. J., and U. Gradmann., *Surface Science* 193(1) 94-108 (1988).

Farrow, R. F. C., Weller, D., Marks, R. F., Toney, M. F., Cebollada, A., Harp, G. R., *Journal of Applied Physics*, 79(8), 5967-5969 (1996).

Fischbacher, T., Franchin, M., Bordignon, G., Fangohr, H., *IEEE Transactions on Magnetics*, 43(6), 2896-2898 (2007).

Fischer, R., Schrefl, T., Kronmüller, H., Fidler, J., *Journal of Magnetism and Magnetic materials*,153(1), 35-49 (1996).

Fritzsche, H., Kohlhepp, J., Gradmann, U., *Physical Review B*,51(22), 15933 (1995).

Fullerton, E. E., Jiang, J. S., Bader, S. D., *Journal of Magnetism and Magnetic Materials*, 200(1), 392-404 (1999).

Fullerton, E. E., Jiang, J. S., Grimsditch, M., Sowers, C. H., Bader, S. D., *Physical Review B*, 58(18), 12193 (1998).

Fullerton, E. E., Jiang, J. S., Rehm, C., Sowers, C. H., Bader, S. D., Patel, J. B., Wu, X. Z., *Applied Physics Letters*, 71(11), 1579-1581 (1997).

Garitaonandia, J. S., Insausti, M., Goikolea, E., Suzuki, M., Cashion, J. D., Kawamura, N., Rojo, T., *Nano Letters*, 8(2), 661-667 (2008).

Gaunt, P., *Philosophical Magazine B*, 48(3), 261-276 (1983).

Goll, D., Seeger, M., Kronmüller, H., *Journal of Magnetism and Magnetic Materials*, 185(1), 49-60 (1998).

Gomes, A. M., Novak, M. A., Sessoli, R., Caneschi, A., Gatteschi, D., *Physical Review B*, 57(9), 5021 (1998).

Goremychkin, E. A., Osborn, R., Rainford, B. D., Macaluso, R. T., Adroja, D. T., Koza, M., *Nature Physics*, 4(10), 766-770 (2008).

Gradmann, U., T. Dürkop, and H. J. Elmers., *Journal of Magnetism and Magnetic Materials* 168(3), 94-108 (1997).

Grollier, J., Boulenc, P., Cros, V., Hamzić, A., Vaurès, A., Fert, A., Faini, G., *Applied Physics Letters*, 83, 509 (2003).

Guerrero, E., Munoz-Marquez, M. A., Fernandez, A., Crespo, P., Hernando, A., Lucena, R., Conesa, J. C., *Journal of Applied Physics*, 107(6), 064303 (2010).

Harbola, M. K., Sahni, V., *Physical Review B*, 37(2), 745 (1988).

Harris, J. G. E., Grimaldi, J. E., Awschalom, D. D., Chiolero, A., Loss, D., *Physical Review B*, 60(5), 3453 (1999).

Hayashi, M., Thomas, L., Moriya, R., Rettner, C., Parkin, S. S., *Science* 320, 209-211 (2008).

Hayashi, M., Thomas, L., Rettner, C., Moriya, R., S. P. Parkin, S., *Nature Physics*, 3, 21-25 (2006).

He, L., Chen, C., *Physical Review B* 75, 184424 (2007).

He, L., *Journal of Physical Chemistry C*, 114(29), 12487-12489 (2010).

Herbst, J. F., Croat, J. J., Pinkerton, F. E., Yelon, W. B., *Physical Review B*, 29(7), 4176 (1984).

Hernandez, J. M., Zhang, X. X., Luis, F., Bartolomé, J., Tejada, J., Ziolo, R., *Europhysics Letters*, 35(4), 301 (1996).

Herzer, G., *IEEE Transactions on Magnetics*, 26(5), 1397-1402 (1990).

Herzer, G., Properties and Applications of Nanocrystalline Alloys from Amorphous Precursors, 15-34, *Springer Netherlands* (2005).

Hori, H., Yamamoto, Y., Iwamoto, T., Miura, T., Teranishi, T., Miyake, M., *Physical Review B*, 69(17), 174411 (2004).

Hori, H., Teranishi, T., Nakae, Y., Seino, Y., Miyake, M., Yamada, S., *Physics Letters A*, 263, 406 (1999).

Huang, H. T., Ger, T. R., Lin, Y. H., Wei, Z. H., *Lab Chip*, 3098-3104 (2013).

Hurd, C. M., Shiozaki, I., McAlister, S. P., *Physical Review B*, 26(2), 701 (1982).

Huse, D. A., Henley, C. L., *Physical Review Letters*, 54(25), 2708 (1985).

Introduction to Solid State Physics, Charles Kittal, 7th edition

Iwasa, T., Nobusada, K., *The Journal of Physical Chemistry C*, 111(1), 45-49 (2007).

Jacobsen, H., Lefmann, K., Brok, E., Frandsen, C., Mørup, S., *Journal of Magnetism and Magnetic Materials*, 324(19), 3218-3222 (2012).

James, P., Eriksson, O., Johansson, B., Abrikosov, I. A., *Physical Review B*, 59(1), 419 (1999).

Ji, N., Lauter, V., Sun, C. J., Allard, L. F., Ambaye, H., Heald, S. M., Wang, J. P., *arXiv preprint* arXiv:1211.0553 (2012).

Ji, N., Liu, X., Wang, J. P., New Journal of Physics, 12(6), 063032 (2010).

John, J., Tang, Y., Rothstein, J. P., Watkins, J. J., Carter, K. R., *Nanotechnology* 24.50, 505307 (2013).

K Arora, S., J O'Dowd, B., Thakur, P., B Brookes, N., Ballesteros, B., Gambardella, P., V Shvets, I., *Current Nanoscience*, 9(5), 609-614 (2013).

Kato, M., Nishino, Y., Mizutani, U., Asano, S., *Journal of Physics: Condensed Matter*, 12(8), 1769 (2000).

Kim, J., Lema, K., Ukaigwe, M., Lee, D., *Langmuir*, 23, 7853–7858 (2007).

Kimling, J., PhD Dissertation, Hamburg University (2013).

Kiwi, M., *Journal of Magnetism and Magnetic Materials*, 234(3), 584-595 (2001).

Kneller, E. F., Hawig, R., *IEEE Transactions on Magnetics*, 27(4), 3588-3560 (1991).

Knepper, J. W., Yang, F. Y., *Physical Review B*, 71(22), 224403 (2005).

Kotsugi, M., Mizuguchi, M., Sekiya, S., Mizumaki, M., Kojima, T., Nakamura, T., Watanabe, Y., *Journal of Magnetism and Magnetic Materials*, 326, 235-239 (2013).

Kotsugi, M., Mizuguchi, M., Sekiya, S., Ohkouchi, T., Kojima, T., Takanashi, K., Watanabe, Y., *Journal of Physics: Conference Series* 266 (1) 012095 (2011).

Krimmel, A., Hemberger, J., Nicklas, M., Knebel, G., Trinkl, W., Brando, M., Ressouche, E., *Physical Review B*, 59(10), R6604 (1999).

Krishna, K. S., Tarakeshwar, P., Mujica, V., & Kumar, C. S., *Small*, 10(5), 907-911 (2014).

Lascialfari, A., Jang, Z. H., Borsa, F., Carretta, P., Gatteschi, D., *Physical Review Letters*, 81(17), 3773 (1998).

Lavenn, C., Albrieux, F., Bergeret, G., Chiriac, R., Delichère, P., Tuel, A., Demessence, A., *Nanoscale*, 4(23), 7334-7337 (2012).

Lee, J. Y., Lee, K. S., Choi, S., Guslienko, K. Y., Kim, S. K., *Physics Review B* 76, 184408 (2007).

Lee, J. Y., Lee, K. S., Kim, S. K., *Applied Physics Letters*, 91, 122513 (2007).

Leuenberger, M. N., Loss, D., *Nature*, 410 (6830), 789-793 (2001).

Li, C., Fan, W., Lei, B., Zhang, D., Han, S., Tang, T.,Zhou, C., *Applied Physics Letters*, 84(11), 1949-1951(2004).

Li, S. P., Natali, M., Lebib, A., Pepin, A., Chen, Y., Xu, Y. B., *Journal of Magnetism and Magnetic Materials* 241, 447-452 (2002).

Liedke, M. O., Körner, M., Lenz, K., Fritzsche, M., Ranjan, M., Keller, A., Fassbender, J., *Physical Review B*, 87(2), 024424 (2013).

Luo, W., Pennycook, S. J., Pantelides, S. T., *Nano Letters*, 7, 3134 (2007).

Magnetism in Condensed Matter (*Oxford Master Series in Physics*) (06 December 2001) by Stephen Blundell

Maitra, U., Das, B., Kumar, N., Sundaresan, A., Rao, C. N. R., *ChemPhysChem* 12(12), 2322-2327 (2011).

Malhotra, S. S., Liu, Y., Shan, Z. S., Liou, S., Stafford, D. C., Sellmyer, D. J., *Journal of Applied Physics*,79(8), 5958-5960 (1996).

Mangin, S., Ravelosona, D., Katine, J. A., Carey, M. J., Terris, B. D., Fullerton, E. E., *Nature Materials*, 5(3), 210-215 (2006).

Mannini, M., Pineider, F., Sainctavit, P., Danieli, C., Otero, E., Sciancalepore, C., Sessoli, R., *Nature Materials*, 8(3), 194-197 (2009).

Meiklejohn, W. H., Bean, C. P., *Physical Review*, 105(3), 904 (1957).

Michael, F., Gonzalez, C., Mujica, V., Marquez, M., Ratner, M. A., *Physical Review B*, 76(22), 224409 (2007).

Miura, Y., Ozaki, S., Kuwahara, Y., Tsujikawa, M., Abe, K., Shirai, M., *Journal of Physics: Condensed Matter*, 25(10), 106005 (2013).

Mohapatra, S., Kumar, R. K., Maji, T. K., *Chemical Physics Letters*, 508(1), 76-79 (2011).

Morales, M. P., Veintemillas-Verdaguer, S., Montero, M. I., Serna, C. J., Roig, A., Casas, L., Sandiumenge, F., *Chemistry of Materials*, 11(11), 3058-3064 (1999).

Mørup, S., Frandsen, C., *Physical Review Letters*, 92(21), 217201 (2004).

N. D. The, Master Thesis, Vietnam National University (2006).

Nealon, G. L., Donnio, B., Greget, R., Kappler, J. P., Terazzi, E., Gallani, J. L., *Nanoscale*, 4(17), 5244-5258 (2012).

Negishi, Y., Tsunoyama, H., Suzuki, M., Kawamura, N., Matsushita, M. M., Maruyama, K., Tsukuda, T., *Journal of the American Chemical Society*, 128(37), 12034-12035 (2006).

Neu, V., Häfner, K., Schultz, L., *Journal of Magnetism and Magnetic Materials*, 322(9), 1613-1616 (2010).

Nogués, J., Schuller, I. K., *Journal of Magnetism and Magnetic Materials*, 192(2), 203-232 (1999).

Néel, L., *Annals of Geophysics* 5, 99 (1949).

Pardavi-Horvath, M., *IEEE Transactions on Magnetics*, 21(5), 1694-1699 (1985).

Parker, F. T., Foster, M. W., Margulies, D. T., Berkowitz, A. E., *Physical Review B*, 47(13), 7885 (1993).

Parkin, S. S., Hayashi, M., Thomas, L., *Science*, 320(5873), 190-194 (2008).

Pederson, M. R., Khanna, S. N., *Physical Review B*, 60(13), 9566 (1999).

Pereiro, M.; Baldomir, D., *Physical Review A*, 72, 045201 (2005).

Pereiro, M.; Baldomir, D.; Arias, J. E., *Physical Review A*, 75, 063204 (2007).

Prados, C., Hattink, B. J., Pina, E., Batlle Gelabert, X., Labarta, A., González-Miranda, J. M., Hernando, A., *IEEE Transactions on Magnetics*, 36, 6 (2000).

Radu, F., Zabel, H., Magnetic heterostructures. *Springer Berlin*, Heidelberg, 97-184 (2008).

Rosch, N., Ackermann, L., Pacchioni,G., *Journal of the American Chemical Society*, 114, 3459 (1992).

Rusponi, S., Cren, T., Weiss, N., Epple, M., Buluschek, P., Claude, L., Brune, H., *Nature Materials*,2(8), 546-551 (2003).

Saravanan, P., Hsu, J. H., Reddy, G. L. N., Kumar, S., Kamat, S. V., *Journal of Alloys and Compounds*, 574, 191-195 (2013).

Sawaga, M., Fujimura, S., Togawa, N., Yamamoto, H., *Journal of Applied Physics* 55 2083 (1984).

Sayama, J., Asahi, T., Mizutani, K., Osaka, T., *Journal of Physics D: Applied Physics*, 37(1), L1 (2004).

Sayama, J., Mizutani, K., Asahi, T., Osaka, T., *Applied Physics Letters*,85(23), 5640-5642 (2004).

Schrefl, T., Fischer, R., Fidler, J., Kronmüller, H., *Journal of Applied Physics*, 76(10), 7053-7058 (1994).

Seifert, M., Neu, V., Schultz, L., Applied Physics Letters, 94(2), 022501-022501 (2009).

Shao, Y. Z., Zhong, W. R., Lan, T., Lee, R. H., *International Journal of Modern Physics B*, 20(01), 61-72 (2006).

Singh, A., Neu, V., Fähler, S., Nenkov, K., Schultz, L., Holzapfel, B., *Physical Review B*,77(10), 104443 (2008).

Skomski, R. Simple models of magnetism. Oxford: *Oxford University Press* (2008).

Skomski, R., Coey, J. M. D., *Physical Review B* 48(21) 15812 (1993).

Skomski, R., *Journal of Applied Physics*, 76(10), 7059-7064 (1994).

Stöhr, J., Siegmann, H. C., Magnetism. Solid-State Sciences. *Springer, Berlin*, Heidelberg, 5 (2006).

Sun, S., Murray, C. B., Weller, D., Folks, L., Moser, A., *Science*, 287(5460), 1989-1992 (2000).

Tang, Y. K., Sun, Y., & Cheng, Z. H., *Journal of Applied Physics*, 100(2), 023914-023914 (2006).

Teng, X., Han, W. Q., Ku, W., Hücker, M., *Angewandte Chemie*, 120(11), 2085-2088 (2008).

Tian, C. B., Chen, R. P., He, C., Li, W. J., Wei, Q., Zhang, X. D., Du, S. W., *Chemical Communications*, 50(15), 1915-1917 (2014).

Tretiakov, O. A., Clarke, D., Chern, G. W., Bazaliy, Y. B., Tchernyshyov, O., *Physical Review Letters* 100, 127204 (2008).

Tripathi, J. K., Markovich, G., Goldfarb, I., *Applied Physics Letters*, 102(25), 251604 (2013).

Uhlig, W. C., Shi, *Applied Physics Letters*. 84, 5 (2004).

Vaz, C. A. F., Bland, J. A. C., *Physical Review B*, 61(4), 3098 (2000).

Velu, E. M. T., Lambeth, D. N., *IEEE Transactions on Magnetics*, 28(5), 3249-3254 (1992).

Vertesy, G., Tomas, I., *Journal of Applied Physics*, 77(12), 6426-6431 (1995).

Visokay, M. R., Bruce M. L., Sinclair, R., *U.S. Patent* No. 5,603,766 (1997).

Visokay, M. R., Sinclair, R., *Applied Physics Letters* 66(13) 1692-1694 (1995).

Vollath, D., Szabó, D. V., Willis, J. O., *Materials Letters*, 29(4), 271-279 (1996).

Vázquez, M., K. Pirota, M. Hernandez-Velez, V. M. Prida, D. Navas, R. Sanz, F. Batallan, and J. Velazquez, *Journal of Applied Physics* 95, 11 (2004).

Vértesy, G., Tomáš, I., Půst, L., Pačes, J., *Journal of Applied Physics*, 71(7), 3462-3466 (1992).

Wu, C. M., Li, C. Y., Kuo, Y. T., Wang, C. W., Wu, S. Y., Li, W. H., *Journal of Nanoparticle Research*, 12(1), 177-185 (2010).

Yan, M. L., Sabirianov, R. F., Xu, Y. F., Li, X. Z., Sellmyer, D. J., *IEEE Transactions on Magnetics*, 40(4), 2470-2472 (2004).

Zangari, G., Lu, B., Laughlin, D. E., Lambeth, D. N., *Journal of Applied Physics*, 85(8), 5759-5761 (1999).

Zavaliche, F., Zheng, H., Mohaddes-Ardabili, L., Yang, S. Y., Zhan, Q., Shafer, P., Ramesh, R., *Nano Letters*, 5(9), 1793-1796 (2005).

Zhang, J., Song, J. Z., Zhang, Y., Wang, F., Chen, B. C., Shen, B. G., Sun, J. R., *IEEE Transactions on Magnetics*, 47(10), 2792-2795 (2011).

Zhang, L. N., Hu, J. F., Chen, J. S., Ding, J., *Journal of Magnetism and Magnetic Materials*, 321(17), 2643-2647 (2009).

Zheng, H., Skomski, R., Menon, L., Liu, Y., Bandyopadhyay, S., Sellmyer, D., *Physical*

Review B 65 (2002).

Zhu, M., Aikens, C. M., Hendrich, M. P., Gupta, R., Qian, H., Schatz, G. C., Jin, R., *Journal of the American Chemical Society*, 131(7), 2490-2492 (2009).

Zhu, M., Aikens, C. M., Hollander, F. J., Schatz, G. C., Jin, R., *Journal of the American Chemical Society*, 130(18), 5883-5885 (2008).

Zighem, F., Maurer, T., Ott, F., Chaboussant, G., *Journal of Applied Physics*, 109(1), 013910 (2011).